Thèse présentée à l'École Polytechnique
pour obtenir le grade de

DOCTEUR DE L'ÉCOLE POLYTECHNIQUE
ET DE L'UNIVERSITÀ degli STUDI di MILANO

Spécialité: Lasers et Matière

par
Alessandro FLACCO

Experimental study of proton acceleration with ultra-high intensity, high contrast laser beam

soutenue publiquement le 3 Juillet 2008
à l'Université de Milan devant le Jury composé de:

M. Philippe BALCOU	CELIA, Bordeaux	Rapporteur
M. Dimitri BATANI	Univ. Milano-Bicocca	
M. Ilario BOSCOLO	Univ. Milano	Directeur de thèse
M. Erik LEFEBVRE	CEA-DIF, Saclay	
M. Victor MALKA	LOA/ENSTA	Directeur de thèse
M. Giorgio TURCHETTI	INFN, Bologna	Rapporteur et Président du Jury

Thèse préparée au Laboratoire d'Optique Appliquée UMR7605
ENSTA - École Polytechnique - CNRS

Verso la mezzanotte calpestai,
irta di forme idolatriche sulla sabbia gialla,
la nera ombra delle sue mura.
Borges

Pour elle,
la mia tazzina blu

Remerciements

Je tiens d'abord à remercier Mme Danielle Hulin, ancienne directrice du Laboratoire d'Optique Appliquée, pour m'avoir accueilli dans son laboratoire, puis comme étudiant en co-tutelle, me permettant ainsi d'élargir les horizons de mon doctorat. Mes activités au sein du laboratoire ont été, chaque jour, d'une grande nouveauté et ont toujours représenté une occasion d'évolution, tant personnelle que professionnelle.

Je tiens à remercier chaleureusement les membres de mon jury de thèse, qui ont accepté le voyage dans la chaleur infernale ce jour de juillet 2008 à Milan. Je tiens surtout à remercier mes rapporteurs, M. Philippe Balcou et M. Giorgio Turchetti, pour avoir lu attentivement tous les chapitres, et de m'avoir prodigué de précieux conseils. Je tiens spécialement à remercier M. Erik Lefebvre: Erik a été d'une aide précieuse durant toute la durée de ma thèse ainsi que dans la correction des chapitres théoriques. Un grand merci à Rachel Nuter pour la réalisation des simulations avec Chivas et pour avoir répondue toujours avec patience et intérêt à mes questions.

Un ringraziamento speciale al prof. Ilario Boscolo, che ha accettato di appoggiarmi in una cotutela azzardata e che ha continuato a seguire il mio lavoro, pur in condizioni avverse. A questo proposito, ringrazio in modo particolare il prof. G.P. Bellini, direttore della scuola di dottorato, e il sig. A. Zanzani, preziosissimo e invidiatissimo alleato di ogni dottorando del Dipartimento di Fisica di Milano.

Dans le plan de ma thèse, un chapitre en soi devrait être dédié aux remerciements pour M. Malka. Merci Victor, pour avoir su me diriger et me guider; pour m'avoir laissé suffisamment d'espace pour apprendre de mes erreurs, en me ramenant sur la bonne voie quand je m'en éloignais trop. Merci pour la confiance que tu donnes aux étudiants, pour l'intérêt, la rigueur et la motivation que tu as su stimuler pendant mes trois intenses années de thèse. Je tiens, de la même manière, à remercier tous mes collaborateurs du groupe SPL, des collaborateurs ≪ directs ≫, Alain, Mina, Hélise et François, aux ≪ indirects ≫, Jérôme et Clément. A grateful "thank you" goes to Narayanan for his

precious collaboration, from experiments in *Salle Jaune* to the real-time dubbing in a cinema in Mumbay.

Un ringraziamento molto sentito a Dimitri Batani, il relatore ombra, forse il vero unico responsabile di tutto questo. Per avermi portato, in piene vacanze di Natale, a visitare il LOA: studentello sperduto che ero, con Los Angeles alle spalle e non ricordo più cosa davanti...
Per tutti i viaggi, per tutte le riunioni, per tutti i ristoranti (da chez Gladine fino a Creta) e tutti gli esperimenti. Per essere stato, in questi anni, un fondamentale punto di riferimento, umano e scientifico.

Une thèse, qui plus est expérimentale, contient le travail d'une quantité de personnes. Des gros mercis à tout le personnel du LOA, notamment à Denis Douillet et Thierry Lefrou, pour leur disponibilité et résistance aux questions idiotes, à Charlie, pour sa promptitude et sa précision dans les réalisations (y compris le "tension - graissage de chaîne") et à Michael, pour tout les travaux du type "vendredi, 15h" que je lui ai filé. Merci à toute l'équipe laser, Amar, Frédéric, Gilles, etc... de nous avoir délivré ces trop précieux photons. Je remercie chaleureusement toutes les personnes qui, soit par leurs activités, soit par leurs présences (197 fois merci Fatima!), ont participé à ces années des travails, même si je ne peux pas les remercier nominalement ici.

Infine a Lorenzo, a Giorgio, a Fetz, a Luca Colombo, a Valentina, a Benoîte, a Chiara; a `proton`, che giace morto in preda a Windows, a `mosquito`, che giace morto e basta, e a `wintermu{x,te}`, che chissà quanto ancora resisterà. A tutto `LCM`, e alla memoria di Michele Dondi, venuto a mancare quando ancora io festeggiavo.
Questa tesi è indissolubilmente legata a tutto ciò che è stata Parigi per me in questi tre anni, da Belleville a Nation, da Camus a Stendhal (passando per Zola) e dalla ReR al TDR. All'alba sulla Senna, vista dal ponte della 6, nel sonno di interminabili mattine, et à la langue française, que je torture depuis mon arrivé. E a Luppi, Pellicciotti, Lucio, Elena, Jhenzo, Feffe e Matthew. Alla Manu, per troppe cose.

Un profondissimo grazie a Tommaso, senza il quale tutto ciò sarebbe stato, probabilmente, molto diverso.

A Francesca, per tutto quello che non siamo.

Contents

I Introduction **1**

1 Introduction **3**

II Physics **9**

2 Lasers **11**

2.1 Laser pulse 11

2.1.1 Relativistic laser pulse 13

3 Laser Particle Acceleration **15**

3.1 Plasmas 15

3.2 Plasma created by lasers 17

3.2.1 Matter ionization and plasma creation 17

3.2.2 Correlation with the pulse duration 19

3.3 Electron Heating from UHI lasers and particle acceleration 21

3.4 Laser ion acceleration 25

3.4.1 Acceleration from the illuminated surface 26

3.4.2 Rear surface acceleration 27

III Experiments **35**

4 Interferometric Study of Plasma Expansion **37**

4.1 Experimental Setup 38

4.1.1 Laser 38

4.1.2 Experiment 40

4.2 Experimental Procedure 44

4.2.1 Spatial alignments 45
4.2.2 Synchrony 45
4.2.3 Error Estimation 46
4.3 Experimental Data 47
4.4 Results and Comparison with Simulations 51
4.5 Discussion and Conclusion 56

5 Reflectometry Study of Thin Metal Foil Perturbation 59
5.1 Introduction 59
5.2 Reflectometry Measurements of a Metallic Surface 60
5.3 Experimental Setup 63
5.4 Experimental Data 67
5.5 Analysis of the Experimental Data 71
5.6 Discussion 74

6 Proton acceleration: experimental setup 77
6.1 The laser source 77
6.1.1 Enhancement of the Contrast 79
6.1.2 Adaptive correction of the phase front 84
6.2 The experimental installation 85
6.2.1 Laser Diagnostics 87
6.2.2 Proton Diagnostics 89

7 Proton acceleration in the high contrast regime 103
7.1 Previous Works 104
7.2 Experimental procedure 108
7.3 Validation of experimental parameters 111
7.3.1 Target focusing 111
7.3.2 MCP Calibration and Alignment 114
7.4 Proton Acceleration with Enhanced Contrast Laser 115
7.4.1 Correlation with Target Thickness 116
7.4.2 Correlation with Laser Energy and Pulse Duration 118
7.5 Discussion and Conclusions 123

IV Résumé en Français **125**

8 Contexte du Travail de Recherche **127**
8.1 Les sources laser ultra-intenses 127
8.2 L'accélération d'ions par laser 128
8.2.1 Dépendance du couplage avec les paramètres laser 128
8.3 Structure du manuscrit de thèse et de son résumé 129

9 Expériences préparatoires **131**
9.0.1 Source laser utilisée 131
9.1 Étude interférométrique d'expansion d'un plasma 132
9.1.1 Reconstruction de la carte 3D des densités 132
9.1.2 Procédure expérimentale 133
9.1.3 Comparaison avec les simulations 133
9.2 Étude du débouché de l'onde de choc par variation de réflectivité 134
9.2.1 Mesure optique de température électronique 134
9.2.2 Réalisation expérimentale 135
9.2.3 Résultats Expérimentaux 135
9.3 Conclusion 136

10 Expériences d'accélération de particules par laser **137**
10.1 Réalisation des expériences 137
10.1.1 Détection des faisceaux ioniques 138
10.2 Résultats expérimentaux 139
10.2.1 Validation des paramètres et des diagnostiques 139
10.2.2 Accélération des protons dans un régime de haut contraste . . . 139
10.3 Conclusions 140

11 Conclusions **143**

V Conclusions and Perspectives **147**

VI Appendices **157**

A Two beams proton acceleration **159**
A.1 Two beams setup 159

A.2 Experimental Results 162
A.3 Discussion and Conclusion 163

B Fundamentals of Plasma Interferometry **165**
B.1 Fundamentals of plasma interferometry 165
B.1.1 Maxwell equations 165
B.1.2 Electrical permittivity for a cold plasma 167
B.1.3 Refraction index for a cold plasma 167
B.1.4 Plasma Interferometry 168
B.2 Numerical Analysis of Interferograms 172
B.2.1 Application to the experimental case 173

Part I

Introduction

Chapter 1

Introduction

It was in the far 1917 that A. Einstein [21] developed the theory of stimulated emission in conjunction with the inversion of population. He showed that in a medium where a population inversion exists, where charged states are more populated than the ground state, the probability for an atom to undergo stimulated emission is higher than the probability for spontaneous. It was only in 1960 that T. H. Maiman [63] practically realized a source of stimulated electromagnetic radiation in the optical band, pumping a ruby crystal, Al_2O_3:Cr, with a flash lamp. The inversion of population was obtained by the presence, in the pumped material, of meta-stable, longer lived, energy levels. The laser era began.

Lasers

In a laser source a medium is pumped to produce the population inversion. The production of a laser beam is obtained in an optical cavity, which *(i)* provides a resonant feedback to the lasing medium and *(ii)* forms and collimates a beam. In a stable optical cavity[1], resonant modes are selected and amplified; the technology used to pump the medium and the insertion of intra-cavity devices defines the characteristics of the produced beam. During the past decades, several technological solutions have been explored to increase the final intensity. Continuous wave (CW) lasers are obtained by continuously pumping the lasing medium, which is easily accomplished in gas lasers by electrical discharge; only in recent times diode pumping made possible the construction

[1]The stability of an optical cavity long L composed by mirrors of curvature radius R_i is defined by the condition $\prod_i g_i < 1$, where the factor $g_i = 1 - L/R_i$ is calculated for each mirror.

of solid-state CW lasers. Pulsed pumping, mainly represented by flash lamps, produces laser pulses on the timescale of the self-relaxation of the medium. This results in pulses with a duration in the order of *microseconds* (μs) and powers in the range of several KiloWatts. Instead of a continuous/relaxed emission, a train of shorter pulses can be obtained by triggering the emission process. The Q-Switching (quality switching) consists in dropping the quality factor of the cavity to an almost "no feedback state" while the medium is being pumped. Once the quality factor is restored, the avalanche process is let begin, releasing all the accumulated energy in a shorter time, resulting in higher intensities. The Q-Switch effect can be obtained by using active (Pockels cells) or passive (saturable absorbers) devices. Q-switched, solid state lasers can produce pulses with a duration in the range of a *nanosecond* (*ns*) and intensities up to hundreds of MegaWatts. Even shorter pulses are created in Mode-locked (ML) lasers. In a cavity long L, resonant modes are separated in frequency by $\Delta\nu = c/2L$[2]; modes that fall into the bandwidth of the amplification medium are allowed to survive (Fig.1.1-*left*), but no correlation between their absolute phase exists. The overall effect is the formation of random intensity fluctuations due to beating between the uncorrelated different wavelengths. The modes are said to be locked when they are forced to be in phase

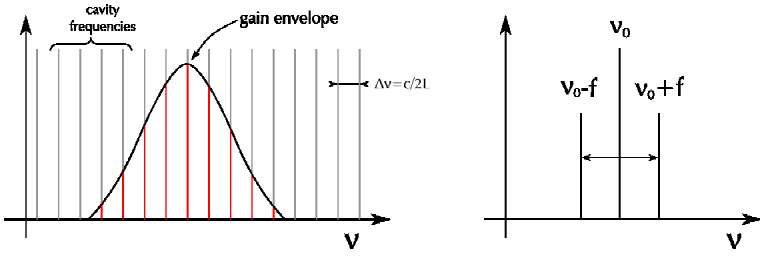


Figure 1.1: *(left)* The bandwidth of the amplification medium selects the resonant cavity modes; *(right)* Mode-locking at frequency f produces satellites in the spectrum at $\nu_0 \pm f$

one with each other; when this happens, phase-locked interference produces a comb of higher intensity pulses. The mode-locking can be produced by active or passive devices. Active mode locking is obtained by an acousto-optical modulator. If a small amplitude modulation is induced at a frequency $f = c/2L$, sidebands for each existing mode will appear and overlap with neighbouring modes (Fig.1.1-*(right)*). In-phase modes will be more amplified than others, making them to survive. Passive mode-locking is obtained

[2]This is true only for the TEM_{00} mode.

by saturable absorbers or Kerr effect (Kerr lens mode-locking, KLM). In both cases, strong losses are introduced for certain under-threshold intensities, which will let only the modes that produce the higher peak to propagate. In the first it is used the property of certain materials to increase their transmission depending on the incoming intensity. In the second, the Kerr effect of $\chi^{(3)}$ crystals is used to focus different components on different planes, depending on their intensity. With mode-locking, the pulse duration is lowered to *picoseconds* (*ps*) and *femtoseconds* (*fs*), producing peak intensities in the order of several GigaWatts. The CPA (Chirped Pulse Amplification) is a technique to amplify a laser pulse (Fig.1.2), introduced at the University of Rochester in 1985 by G.Mourou[95] in 1985. The short pulse from an oscillator is stretched, introducing a

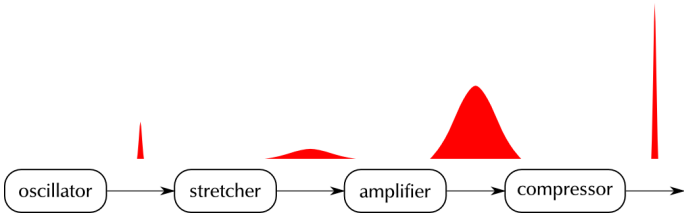


Figure 1.2: Block scheme of a CPA chain.

linear chirp φ_2 on its spectral components:

$$E(\omega) = \delta(\omega-\omega_0) * \mathrm{e}^{-\omega^2/\Delta\omega^2} \xrightarrow{\text{stretching}} \delta(\omega-\omega_0) * \mathrm{e}^{-\omega^2/\Delta\omega^2}\mathrm{e}^{\mathrm{i}\varphi_2\omega}. \tag{1.1}$$

The stretch is obtained by letting the pulse propagate through strongly dispersive materials or with appropriate optical setups[3]. The resulting pulse will have the same spectral content but a longer duration. A longer pulse can be amplified more, in energy, than a shorter one, for its lower peak intensity pushes further the limits imposed by damage and non-linear response in crystals and refractive optics. The stretched pulse is sent to a chain of power amplifiers. For power amplification, multi-pass (open cavity) amplifiers are used, where the incoming pulse is the seed that stimulates emission from a (previously) charged crystal. The amplified pulse is finally re-compressed[4]; the φ_2

[3] One (or more) diffraction gratings are used to separate and re-collimate the beam. Between the two, an optical path introduced to add different delay times depending on the wavelength.

[4] A two gratings compressor contains no refractive parts.

term is eliminated and the pulse is shortened to about its original duration[5]. At the time of writing, commercial CPA systems, based on Ti-doped Sapphire crystals, deliver pulses in the $30-60fs$ range with peak intensities of hundreds of TeraWatts. Prototype systems are reported to have reached the PetaWatt ($10^{15}W$).

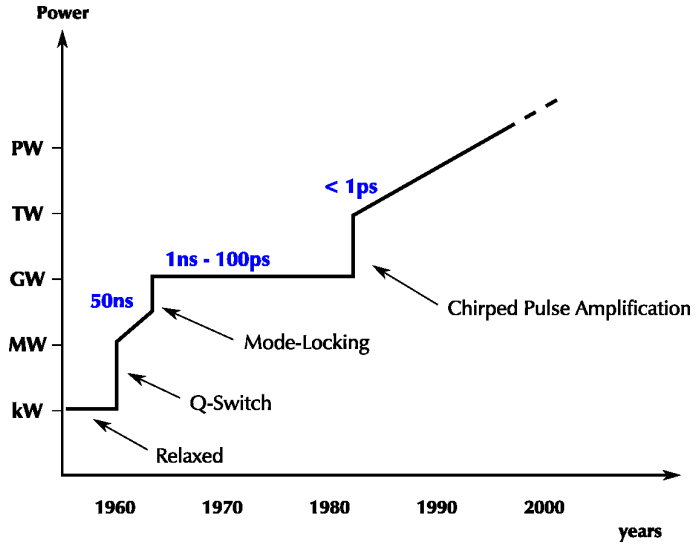


Figure 1.3: Evolution of laser power in time.

Particle Acceleration

Since their discovery, elementary particles represented an extremely important subject for applied and theoretical research. In particular, energetic particle sources gained importance in fundamental research (the huge electrostatic accelerating machines) and in medical application (cancer treatment, non invasive diagnostics).
In a classical accelerator, a bunch from particle source (heated filament, photocathodes, gases ionization, nuclear reactions) is injected in an accelerating structure, which is in charge of transporting, accelerating and shaping it.
In time, bigger accelerating machines have been designed and built. At the time of writing, the Tevatron in Fermilab reaches the energy of $980GeV$ ($1.96TeV$ in the center of mass) and the LHC in Geneva is about to be lit: at full specifications it will reach

[5]The non-uniform gain curve of the amplifying media produces a shrinking of the spectrum, and consequently a longer pulse. Typical value for Ti:Sapphire is $150nm$ at the oscillator output cut to $40nm$ after $\times 1000$ amplification.

$2.76\,TeV$ for a total of $5.52TeV$ in the center of mass. While there is no theoretical limit on the number of accelerating sections[6] on the beam path, physical and structural limits are imposed on single structures. The technological improvements have pushed the values of accelerating gradients from KV/m to MV/m, from electrodes to RF-cavities[7] but limitations arise due to the structural stress of the materials.

In parallel to the development, control, and realization of high frequency superconducting cavities by the mainstream accelerator community, some plasma physicists started in the 1980's to work on compact plasma accelerators. Ultra high-gradient acceleration techniques, using field amplitudes of $100GV/m$ to TV/m, rely on space charge separation between electrons and ions in plasmas. Because of this key property, plasmas have been recognized as promising accelerating media since the pioneering work of Tajima and Dawson in 1979[97] . Static electric fields are produced to accelerate ions, whereas "travelling" electric fields supported by electron plasma waves are used to accelerate lighter particles such as electrons or positrons.

In laser-plasma electron accelerators, a longitudinal accelerating electric field is excited by the ponderomotive force of an ultra-short and ultra-intense laser. This force, proportional to the gradient of the laser intensity, pushes the plasma electrons out of the laser beam path, separating them from the ions. This creates a travelling longitudinal electric field, in the wake of the laser beam, with a phase velocity close to the speed of light, most suitable for accelerating particles to relativistic energies. This electric field, which can reach amplitudes of several hundred GV/m can efficiently accelerated injected electrons. Experimentally, two injection mechanisms (the bubble[65, 33, 23] and the colliding schemes[24]) have recently demonstrated the generation of high quality quasi-monoenergetic electron beams.

In contrast to electrons, ions are best accelerated by a low-frequency (compared to the electron plasma wave frequency), or even a quasi-static electric field. Indeed, due to their higher mass, the rapid field oscillations associated with an electron plasma wave average out to a zero net acceleration for an ion. In present day experiments the mechanisms of ion acceleration can be classified into ponderomotive acceleration or thermal

[6] Although at present merely practical limits arise for civil engineering: the length of a linear accelerator is limited by the terrestrial curvature and in the LHC the beam alignment has to be corrected for the progressive motion of foundations

[7] Ref. LHC design report v1 06/2004, http://doc.cern.ch/yellowrep/2004/2004-003-v1/.

explosion acceleration, based on how the electric charge separation that produces the quasi-static field is generated.

In the 'ponderomotive acceleration' scenario, charge separation is generated by the ponderomotive force of the laser, which sets up a charge imbalance that in turn accelerates ions. In the 'thermal explosion' type scenarios, charge imbalance is maintained by heating a fraction of the plasma electrons to very large temperature. The resulting electron thermal pressure drives an expansion of these hot electrons around the target, setting up a large-amplitude electrostatic field at the target-vacuum interfaces. Field amplitudes greater than a TV/m are produced, leading to efficient ion acceleration from the target surfaces over very short distances.

Structure of the thesis

This thesis is related to the general framework of the interaction between laser pulses at relativistic intensities ($I > 10^{18} W/cm^2$) and solid matter, in particular the use of an Ultra High Intensity laser pulse to extract and accelerate an ion beam.

The manuscript is organized as follows. The chapters Ch.2 and Ch.3 are dedicated to the fundamentals of the laser parametrization and of plasma physics, where my research work situates.
Two preparatory experiments I realized on the *Salle Verte* laser facility are self-consistently described in two separated chapters, Ch.4 and Ch.5. The first is a plasma interferometry experiment, where a *probe* laser pulse is used to map the expansion in time of a plasma, created by a moderate intensity pulse; comparison to simulations is used to infer the propagation timescale of the generated shock in the unperturbed matter. The second one uses reflectometry measures, in an experimental case that is comparable to the first, to monitor the evolution of the non-illuminated surface of a thin shocked target.
To the proton acceleration experiment, two separate chapters are dedicated. In the first (Ch.6) I describe in detail the facility where the experimental measurements are performed, discussing the key features of the laser system and of the adopted diagnostic strategy. The second chapter (Ch.7) is dedicated to the experimental procedures and the presentation and discussion of the obtained results.

Part II

Physics

Chapter 2

Lasers

2.1 Laser pulse

Depending on the characteristics of the source, spectral content and transverse profile, a laser pulse can hold different temporal and spatial features. Here I briefly introduce the relationships defining the behaviour of the laser beam I used.

Gaussian Laser pulse

During the research activities here described, pulses with temporal and spatial gaussian profile are used. The temporal and spatial dependencies of a gaussian pulse of FWHM (Full Width Half Maximum) duration τ_0 (on the intensity envelope) and radius w (at $1/e^2$ of intensity), which propagates on the z axis ($\underline{x} = (x, y, z)$, $\underline{k} \cdot \underline{x} = k_0 z$) is written as:

$$E(r,z,t) = E_0 \exp\left[-\frac{r^2}{w^2}\right] \exp\left[-2\ln(2)\left(\frac{z-ct}{c\tau_0}\right)^2\right] e^{i(kz-\omega t)} \tag{2.1}$$

The intensity envelope will then be

$$I(r,t) = I_0 \exp\left[-2\left(\frac{r}{w}\right)^2\right] \exp\left[-4\ln(2)\left(\frac{z-ct}{c\tau_0}\right)^2\right] \tag{2.2}$$

where $I_0 = (1/2)\, c\, \varepsilon_0 E_0^2$ and c the speed of light in vacuum. The peak intensity I_0 normalized to the total energy contained in the pulse, E_L, is calculated from the integral

of $I(r,t)$ in $r\,\mathrm{d}r\,\mathrm{d}\theta$, giving

$$I_0 = \frac{4\sqrt{\ln(2)}}{\pi^{3/2}}\frac{E_L}{\tau_0 w^2} \tag{2.3}$$

$$\approx 0.6\,\frac{E_L}{\tau_0 w^2} \quad (^1) \tag{2.4}$$

When we treat the light propagation by approximating the distances at the second order

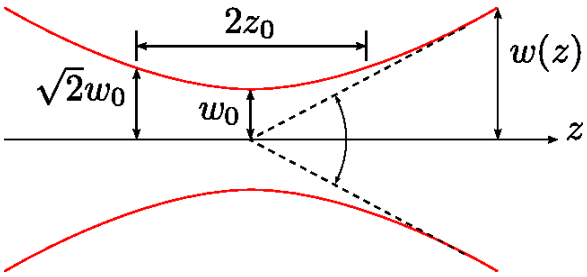


Figure 2.1: Gaussian beam

(Fresnel integrals), a gaussian envelope of field amplitudes is found to be an *eigenstate* in a way that a gaussian envelope evolves keeping its formal structure[2]. The TEM_{00} mode from a confocal cavity has a pure transverse gaussian profile. The optics of gaussian beams is of fundamental importance in laser optics because it defines the way energy is transported and concentrated, defines boundaries and asymptotic behaviour. In the ideal case, the phase front curvature and the width of the amplitude envelope are bound to the distance of propagation by simple relations; for a pulse like the one defined in (2.1) it holds

$$w(z) = w_0\sqrt{1+\left(\frac{z}{z_0}\right)^2} \tag{2.5}$$

where w_0 is commonly called *beam waist* and

$$z_0 = \frac{\pi w_0^2}{\lambda} \tag{2.6}$$

[1] In some experimental cases, a correct gaussian spot cannot be obtained, due to unsufficient quality of the beam; in these cases, a better estimation of I_0 is done by setting $E_{L,eff} = 2\,E_{FWHM}$ where $E_{L,eff}$ is the effective energy in the FWHM spot, calculated by multiplying the total energy times the measured energy ratio in FWHM.

[2] This, of course, is bound to the II order approximation.

is the Rayleigh range. The waist that is produced when a lens of focal length f focuses the beam of diameter $2w$ is calculated by equating (2.5) to $z = f$ which gives[3]:

$$w_0 \approx \frac{\lambda f}{\pi w} \tag{2.7}$$

From here to the rest of the manuscript, the symbol w will indicate the beam radius at a field amplitude $E/E_0 = 1/\mathrm{e}$ (or intensity $I/I_0 = 1/e^2$); the symbol will be w_0 only for focal spots, where a plane phase front is expected.

Inserting the r-dependent waist (2.5) in (2.4) one obtains

$$I(z) = I_0 \cdot \left[1 + \left(\frac{z}{z_0}\right)^2\right]^{-1/2} \tag{2.8}$$

the dependence of peak intensity versus the distance from the focal plane.

2.1.1 Relativistic laser pulse

An *em* wave is said to be relativistic if the energy W of electrons in the quivering motion due to electric field oscillation make them relativistic. Writing the momentum of the electron in the wave vector potential $\underline{\mathrm{A}}$[4] and normalizing with respect to mc one gets the dimensionless parameter

$$a_0 = \frac{eA}{mc} \tag{2.9}$$

The wave is called relativistic when $a_0 > 1$. The average energy in the oscillation is calculated by the average momentum[5]

$$< p >= \frac{1}{\sqrt{2}} eA \tag{2.10}$$

and the total relativistic energy

$$< E_R >= \sqrt{p^2c^2 + m_0^2c^4} =< W > +m_0c^2 \tag{2.11}$$

[3]The approximation holds for $w\, w_0 \gg w_0^2$.

[4]$\underline{\mathrm{E}} = \partial_t \underline{\mathrm{A}} \rightarrow \underline{\mathrm{A}} = \underline{\mathrm{E}}/\mathrm{i}\,\omega$.

[5]The $1/\sqrt{2}$ factor comes from the averaging of a linearly polarized wave. In case of circular polarization, the factor becomes 1. This also drops the 1/2 factor in (2.13).

giving

$$< W > \;=\; (\gamma - 1)\, mc^2 \tag{2.12}$$

$$\;=\; mc^2 \left\{ \left[1 + \frac{1}{2} \left(\frac{e\underline{\mathrm{A}}}{mc} \right)^2 \right]^{1/2} - 1 \right\} \tag{2.13}$$

The dimensionless field amplitude will be used in the alternative forms

$$a_0 \;=\; \frac{eE}{m_e c\, \omega_0} \;=\; \left[\frac{e^2}{2\pi^2 \varepsilon_0 m_e^2 c^5} \lambda^2 I_0 \right]^{1/2} \tag{2.14}$$

when studying the interaction between the relativistic field and electrons.

Chapter 3

Laser Particle Acceleration

3.1 Plasmas

The plasma state is a state of matter where components are no more neutral; this is usually reached when a bulk is heated to a point where its internal energy is higher than one or more ionization levels, which makes the single atoms to lose electrons in collisions. A plasma can be locally created by ionizing a certain amount of material, like in discharge tubes, heating a rarefied gas with microwaves or by interaction with a laser. The vast set of parameters, in temperature, pressure, density, neutrality makes the plasma state one of the most various chapter of the physics.

Collective parameters In a plasma, for each of the species α, it is defined the α-plasma frequency

$$\omega_{p\alpha} = \sqrt{\frac{n_\alpha q_\alpha^2}{\varepsilon_0 m_\alpha}}, \tag{3.1}$$

which is the oscillating frequency of the α component. This is a key parameter for evaluating the response timescale of the α-plasma to external fields. When a separation of charges is produced, the motion of the α component to restore the neutrality results in an oscillation at the frequency (3.1).

For each charge in a plasma, the surrounding charge distribution balances its electrostatic potential, which effectively screens it, lowering the distance over which its influence should be considered effective. The distance over which the newly created electric field

drops by a factor of $1/e$ is the Debye length[13]:

$$\lambda_D = \sqrt{\frac{\varepsilon_0 k_B T_\alpha}{n_\alpha q_\alpha^2}} \tag{3.2}$$

Fluid equations The interaction between components in a plasma happens through electro-magnetic forces, each particle interacting at the same time with any other in the volume. A precise description of the plasma medium is obtained from the kinetic theory. The probability density function $f_\alpha(\underline{\mathrm{x}}, \underline{\mathrm{v}}, t)$ represents the position of the plasma components of specie α in the $6-$dimensional phase space. From the definition of f_α it follows:

$$\begin{cases} n_\alpha(\underline{\mathrm{x}}, t) &= \int f_\alpha(\underline{\mathrm{x}}, \underline{\mathrm{v}}, t)\, \mathrm{d}^3 v \\ \\ \langle\psi\rangle_\alpha(\underline{\mathrm{x}}, t) &= \dfrac{1}{n_\alpha} \int \psi\, f_\alpha(\underline{\mathrm{x}}, \underline{\mathrm{v}}, t)\, \mathrm{d}^3 v \end{cases} \tag{3.3}$$

Each of the functions must verify the Boltzmann equation which states that[13]

$$\frac{\mathrm{d}f}{\mathrm{d}t} = \left(\frac{\partial f}{\partial t}\right)_{(coll)} \tag{3.4}$$

or

$$\frac{\partial f}{\partial t} + \underline{\mathrm{v}} \cdot \frac{\partial f}{\partial \underline{\mathrm{x}}} + \frac{\underline{\mathrm{F}}}{m} \cdot \frac{\partial f}{\partial \underline{\mathrm{v}}} = \left(\frac{\partial f}{\partial t}\right)_{(coll)}. \tag{3.5}$$

Equation (3.4) states that the convective derivative in the phase space doesn't change unless collisions happen. When describing a plasma, the equation (3.5) is changed to the Vlasov equation:

$$\frac{\partial f_\alpha}{\partial t} + \underline{\mathrm{v}} \cdot \frac{\partial f_\alpha}{\partial \underline{\mathrm{x}}} + \frac{q_\alpha}{m_\alpha} (\underline{\mathrm{E}} + \underline{\mathrm{v}} \times \underline{\mathrm{B}}) \cdot \frac{\partial f}{\partial \underline{\mathrm{v}}} = 0 \tag{3.6}$$

In the Vlasov equation the collision term is dropped and the Lorenz terms are expressed in function of the self consistent fields, $\underline{\mathrm{E}}$ and $\underline{\mathrm{B}}$; these fields are generated by the plasma itself and satisfy the Maxwell equation with the source terms

$$\rho = \Sigma_\alpha\, q_\alpha \int f_\alpha \mathrm{d}^3 v \qquad \underline{\mathrm{j}} = \Sigma_\alpha\, q_\alpha \int \underline{\mathrm{v}} f_\alpha \mathrm{d}^3 v \tag{3.7}$$

The set of equations that enable the fluid treatment of the plasma (fluid equations) is obtained by calculating momenta $\psi(\underline{\mathrm{v}})$ of the Vlasov equation at different orders. When calculating the equation for a given order, a term of higher order in $\underline{\mathrm{v}}$ appears, due to the second term in equation (3.6). A hierarchy of equations is hence created, where each equation contains a term that is defined in the one of higher order. This hierarchy can be stopped whenever physical consideration enable the dropping of the highest order term. At the first two orders, respectively for $\psi = 1$ and $\psi = m\underline{\mathrm{v}}$, one obtains[1]:

$$\frac{\partial n_\alpha}{\partial t} + \underline{\nabla} \cdot (n_\alpha \underline{\mathrm{u}}_\alpha) = 0 \tag{3.8}$$

$$m_\alpha n_\alpha \frac{\mathrm{D}}{\mathrm{D}t}\underline{\mathrm{u}}_\alpha = -\underline{\nabla} \cdot \underline{\underline{\mathrm{P}}}_\alpha + q_\alpha n_\alpha \left(\underline{\mathrm{E}} + \underline{\mathrm{u}}_\alpha \times \underline{\mathrm{B}}\right). \tag{3.9}$$

where have been introduced the fluid velocity $\underline{\mathrm{u}}_\alpha = \langle \underline{\mathrm{v}} \rangle_\alpha$ and the pressure tensor $\underline{\underline{\mathrm{P}}}_\alpha = \langle \underline{\mathrm{vv}} \rangle_\alpha$. In the non viscous approximation the pressure tensor $\underline{\underline{\mathrm{P}}}_\alpha$ is diagonal and can be written in the form

$$\underline{\underline{\mathrm{P}}}_\alpha = p_j \underline{\underline{\mathbf{1}}} = n_\alpha T_\alpha \underline{\underline{\mathbf{1}}} \tag{3.10}$$

where T_α is the kinetic temperature for the α component. In the cold plasma approximation, which is used in forthcoming chapters, it is set $T_\alpha = 0$ in (3.10).

3.2 Plasma created by lasers

The interaction between laser pulses, at a flux over a certain threshold, and supercritical matter (i.e. $\omega_{pe} > \omega_{laser}$) produces a plasma. As a general scenario, electrons are heated at first, by the evanescent wave that penetrates the skin depth $l_s = c/\omega_{pe}$, atoms are ionized and a high temperature corona of plasma starts to expand from the area of interaction. The involved mechanisms range depending on the intensity and the duration of the laser pulse.

3.2.1 Matter ionization and plasma creation

When high intensity electromagnetic (em) radiation interacts with matter, electrons start to oscillate accordingly to the forcing electric field. As intensity increases, the field amplitude becomes comparable to the bounding field of the outer electronic shells (or

[1] Defined the convective derivative $\frac{\mathrm{D}}{\mathrm{D}t} = \frac{\partial}{\partial t} + \underline{\mathrm{u}} \cdot \underline{\nabla}$.

electrostatic potential comparable to the work potential) and nonlinear effects gain in importance. [51, 81, 82]. If no resonant level exists, the direct, single photon, ionization is impossible; when the density of photons is sufficiently high, different ionization mechanisms (nonlinear ionizations) can happen; their small cross section makes them not observable at lower intensities. The relative importance of these cross sections has been extensively studied. The adiabaticity parameter (the Keldysh factor)

$$\gamma_K = \frac{\omega}{\omega_t} = \omega \frac{\sqrt{2mW}}{eA} \tag{3.11}$$

is defined as the ratio between the laser frequency ω and the frequency ω_t of electron tunnelling through a potential barrier. This last comes from the ratio between the electron potential in the oscillating field eA and its ionization momentum $\sqrt{2mW}$, set W the work potential of the level. The value of (3.11) defines the main ionization mechanism, as briefly described hereafter in order of increasing field amplitude.

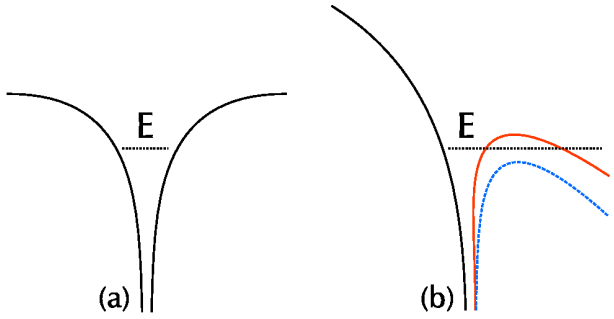


Figure 3.1: Non linear ionization: the electron in the potential well can tunnel through the residual potential (red) of is freed by suppression of the barrier (blue)

Multiphoton ionization For values of $\gamma_K > 1$ the only possible mechanism is the multiphoton ionization. When a sufficient density of photon exists, a bound electron can be freed by the absorption of several photons with an energy lower than the work potential[100, 1, 64]. The typical threshold value ranges between $10^{10} W/cm^2$ and $10^{14} W/cm^2$. In above-threshold ionization (ATI, [2, 34]) more photons are absorbed than necessary for the ionization. In this cases electrons are freed with non-zero energy, and their spectrum shows peaks around multiples on the photon energy, $h\nu$.

Tunnel ionization When $\gamma_K < 1$ the walls of the potential well are deformed in a way that only a finite range of forbidden energies exists for the bound electron. A non-zero probability exists for the electron to tunnel through the potential barrier (Fig.3.1-red).

Suppression of the potential barrier When the well boundary is deformed to have its maximum lower than the energy of the bound electron (Fig.3.1-blue), no more barrier exists and the electron drifts in the electric field ($\gamma_K \ll 1$).

3.2.2 Correlation with the pulse duration

ns pulses

When a *nanosecond* laser pulse interacts with matter, atoms are ionized by multiphoton ionization and electrons accelerated in the laser electric field. In metals the temperature of electrons in conduction band is strongly increased and new electrons from inner shells are promoted to it. In transparent dielectrics electrons have to be freed before any absorption could take place, and this motivates the higher threshold of damage.

In both cases the plasma is produced by collisions between the quivering electrons and the matter at rest. The threshold fluxes for $\tau_L = 1ns$ are of the order of $I\tau_L \gtrsim 1.5J/cm^2$ for gold and $I\tau_L \gtrsim 40J/cm^2$ for fused silica (Fig.3.2). In the ns regime, the laser dura-

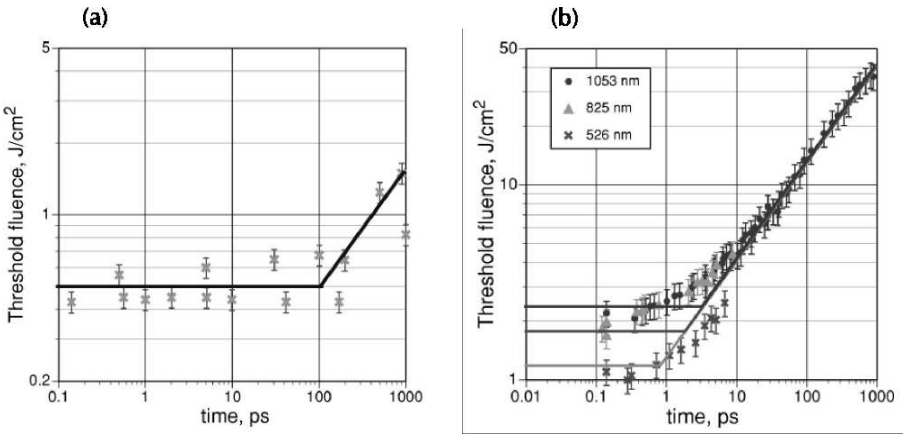


Figure 3.2: Damage thresholds at different pulse length for gold (a) and fused silica (b). (Ref.[30])

tion is longer than the characteristic timescale of thermal processes, which brings to the

quasi-stationary formation of three areas, namely a **corona**, a **conduction region** and a **shocked region**. In the corona ($n_e < n_c$) the laser energy is absorbed by electrons in the plasma at undercritical density[2]; in the conduction region ($n_c < n_e < n_s$) the thermal conduction transports energy from the laser-heated region to the bulk; in the shocked region ($\rho > \rho_s$) the matter is compressed to densities higher than the solid (ρ_s) by conservation of momentum from the expanding motion in the corona (rocket effect). This last effect is responsible for the creation of a shock wave, which propagates towards the unperturbed part of the bulk. During the laser pulse duration, the expansion of the corona in the vacuum can be regarded as isothermal.

sub-*ps* pulses

When the laser duration is $\tau_L < 1ps$, the interaction process with cold matter changes due to (i) the short duration and (ii) the higher intensities reached.
The laser pulse duration is shorter than the characteristic times of electron-to-ion energy transfer, the electron heat conduction and the time of hydrodynamic expansion of the interaction zone. This makes the laser pulse to interact with a solid target where the density remains almost constant.

The higher intensities ($I \sim 10^{13} - 10^{14}\, W/cm^2$ at the threshold) are responsible for almost sudden ionization at the beginning of the laser pulse, not depending on the nature of the material, metal or dielectric. Ablation of the material can happen for charge separation in the interaction zone. Electrons can gain sufficient energy to escape the target and drag ions out of it (when $\varepsilon_e > \varepsilon_{work} + \varepsilon_b$)[3] or can be pushed deeper by ponderomotive force. The expansion starts once the laser pulse has passed over and it can be regarded as adiabatic, where a plasma front propagates towards the vacuum at a speed of

$$v_p = \frac{2\gamma_A^{1/2}}{\gamma_A - 1} c_{s\,0} \tag{3.12}$$

and the transition between the unperturbed bulk and the shocked region at

$$v_s = -\gamma_A^{1/2} c_{s\,0} \tag{3.13}$$

[2]Defined n_c the electron density for which $\omega_{laser} = \omega_{pe}$.
[3]Where are defined ε_e the electron energy, ε_{work} the electron work potential and ε_b the ion work potential.

having defined

$$c_{s0} = \sqrt{\frac{(Z+1)\,k_B T_i}{A m_i}} \tag{3.14}$$

the isothermal speed of sound in the unperturbed material and $\gamma = 5/3$ the adiabatic constant[22].

3.3 Electron Heating from UHI lasers and particle acceleration

This thesis falls in the context of the interaction between Ultra High Intensity (UHI) femtosecond lasers and supercritical matter. At relativistic intensities ($I_0 > 10^{18}\,W/cm^2$) from CPA laser chains (Ch.2) the interaction with a ns pedestal at intensities over the ionization threshold, is to be accounted for before the sub-ps peak. The considered situation is then an UHI, sub-ps pulse interacting with a preformed expanding plasma. In this section I focus on the mechanisms of energy transfer between the laser pulse and the existing plasma gradient, which are responsible for the generation of a suprathermal electron population.

When the *em* wave penetrates the plasma gradient, it propagates freely until the critical surface at density

$$n_c = \frac{\varepsilon_0 m_e}{e^2}\omega \tag{3.15}$$

which is obtained by equating $\omega = \omega_{pe}$ from (3.1). If the field amplitude is relativistic, the electron plasma frequency is corrected by the increase of the accelerated electrons' mass (induced transparency), giving

$$\omega'_{pe} = \sqrt{\frac{1}{\gamma}}\,\omega_{pe} \tag{3.16}$$

The free electrons are made slowly drifting by the $v \times B$ term in the Lorenz force while oscillating in the electric field. The only way to make them gain a net energy from the interaction is to break the adiabaticity of the process, i.e. make them escape the interaction region once they have gained momentum. In a plasma this can happen due to collisionality, wave breaking or steep discontinuities in the density distribution.

Collisional absorption (inverse Bremsstrahlung)

When an electron in its quivering motion in the laser field ω undergoes a collision with an ion, its trajectory in the electric field is lost and a local conversion to thermal energy happens. Given ν_{ei} the electron-ion collision frequency, the overall effect is accounted for an absorption rate of[35, 101, 86]:

$$A_{coll} = \frac{\omega}{\omega_{pe}} \left(\frac{8\nu_{ei}}{\omega} \right)^{1/2} \tag{3.17}$$

where ω_{pe} is the usual electron plasma frequency. From the Spitzer collision frequency for hot plasma[14, 94]

$$\nu_{Spitzer} \;=\; \frac{4}{3}\sqrt{2\pi}\, \frac{Z^* e^4}{16\pi^2 \varepsilon_0^2}\, \frac{m_e n_e}{(m_e k_B T_e)^{3/2}} \ln\left(\Lambda'\right) \tag{3.18}$$

the collisionality decreases as temperature increases (for the definition of Λ' see (5.4)). This mechanism is most effective at lower laser intensities: in the high intensity limit, the thermal motion of electrons becomes much smaller than their velocity in the laser field. The collisional absorption is considered to be negligible for laser intensities higher than $10^{16} W/cm^2$.

ponderomotive forces and $j \times B$ heating

In presence of an electro-magnetic field, a charged particle is subject to the usual Lorentz force.

$$\underline{\mathrm{F}}_L = \frac{q}{m} \left(\underline{\mathrm{E}} + \underline{\mathrm{v}} \times \underline{\mathrm{B}} \right) \tag{3.19}$$

In an electromagnetic wave, the coupling between the E-field and the B-field make the particle to drift in the direction of propagation while quivering in the oscillating electric field. When the field amplitude is not constant in space, a force term, directed along the intensity gradient appears[76, 75]. In the classical limit[54], the oscillation center of a free charge q in the *em* field $\underline{\mathrm{E}}$ at frequency ω_0 is governed by the force

$$\underline{\mathrm{F}}_p \;=\; -\underline{\nabla}\Phi_p; \quad \Phi_p \;=\; -\frac{q^2 \left|E_0\right|^2}{2 m_0 \omega_0^2} \cos\left(2\omega_0 t\right). \tag{3.20}$$

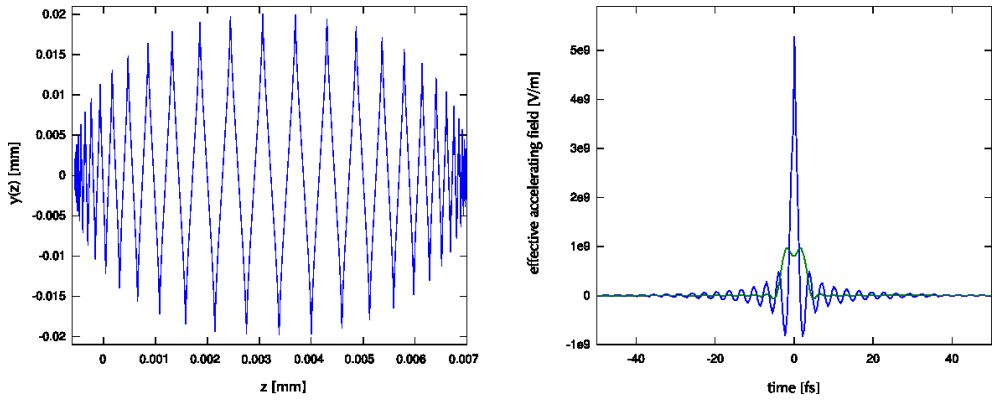


Figure 3.3: Trajectories *(left)* and effective accelerating field due to ponderomotive potential *(right)* for an electron in a short electromagnetic pulse (numerical simulation). The pulse ($\tau_L = 30fs$, $I_0 = 10^{15} W/cm^2$) propagates along $-\hat{z}$ and is polarized on $\hat{y}$. The green plot represents the averaged force term.

The time averaged value of (3.20)

$$\langle \underline{\mathrm{F}}_p \rangle = -\frac{q^2}{4m_0\omega_0^2} \underline{\nabla}|\underline{\mathrm{E}}|^2 \tag{3.21}$$

represents a net force which pushes the charges, independently of their sign, out of the influence of the higher intensity *em* field; being dependent on the $mass^{-1}$, its effect is predominant on the electron component. The ponderomotive push is responsible of the *hole boring* in the target surface[84] and the steepening of the plasma density gradient[25, 6].

The oscillating term at $2\omega_0$ in (3.20) is responsible for the so-called $j \times B$ heating[53]. The non-adiabaticity of electrons in the skin depth, while oscillating in the non-resonant $2\omega_0$ term, can be broken. This happens while following a trajectory which pushes them into the overdense plasma, making them to escape the region of influence of the oscillating force[101].

Resonant absorption and Wavebreaking

It is considered the propagation of a p-polarized wave with vector $\underline{\mathrm{k}} \equiv (k_x, k_y)$ through a plasma density gradient $\underline{\nabla} n_e \parallel \hat{x}$. The local permittivity in the plasma is written as

$$\frac{\varepsilon(x)}{\varepsilon_0} \approx 1 - \frac{\omega_{pe}^2(x)}{\omega_0^2}\left(1 + \frac{\mathrm{i}\nu}{\omega_0}\right) \tag{3.22}$$

where ν is the collision frequency. In the collisionless limit the ratio $\nu/\omega_0 \to 0$, which produces a singularity at the critical surface, where ω equals ω_{pe}. In [27] the numerical solutions of the light propagation equations are presented. At the critical boundary the only non-zero magnetic component (B_z) is purely real, with $B_z > 0$ for $n_e < n_c$ and $B_z = 0$ otherwise. The electric field E_x stays real and is proportional to $1/\nu$, which makes it to diverge in the collisionless limit. From the Ampere's equation on x, $\partial_y B_z = \mu_0 J_x + \partial_t E_x$ a strong electron current arises. The physical situation is the one on an electron plasma wave that is resonantly driven by the forcing field. The electron current in x absorbs energy from the laser wave and the amplitude of oscillations grows in time. The resonant absorption is present only for p-polarized waves, as the electric field component that is normal to the critical surface is needed to drive the plasma oscillations across it. Moreover, the effect is set up only when the plasma gradient length is bigger than the laser wavelength, $L_{grad} \gg \lambda$. An estimate of the ratio of energy absorption is [101]

$$A_{resonant} \approx \frac{1}{2}\left[2.3\,(k_0 L_{grad})^{1/3}\sin(\theta)\cdot\exp\left(-\frac{2}{3}k_0 L_{grad}\sin^3(\theta)\right)\right] \tag{3.23}$$

which shows a maximum for $\theta \approx \arcsin(1/k_0 L_{grad})^{1/3}$. The resonant absorption is the main electron heating process for fluxes $10^{12} W\cdot\mu m^2/cm^2 < I\lambda_{\mu m}^2 < 10^{17} W\cdot\mu m^2/cm^2$.

Wavebreaking As the previously described effect evolves in time, the plasma waves that set up in outer regions, $n_e < n_c$, start to de-phase from the driver, as their self oscillating frequency is different from the forcing one, while the resonant wave grows in amplitude. This produces a shrinking of the resonance area. The waves break when the fluid elements from two regions with a different relative phase come to cross each other's trajectories. In particular if a phase difference of $\pi/2$ exists between the outer and the inner oscillation, some electrons are injected in an inner wave, finding a strong accelerating field, leaving the influence of the driver and propagating in direction of higher densities[27, 3].

vacuum heating (Brunel effect)

When a strong oscillating electric field acts orthogonally on the separation between a conductor and vacuum, electrons can be pulled out of the conductor and sent back at a velocity comparable to their oscillating velocity in the quivering motion,

$$\beta_{osc} = \sqrt{\frac{a_\perp^2}{a_\perp^2 + 1}}. \tag{3.24}$$

The vacuum heating is found to be more important than the resonant absorption when the gradient length L at the critical surface becomes smaller or comparable to the electron displacement in the $\hat{z} = \underline{\nabla} n_e$ direction. An estimation of laser energy absorption is [11]:

$$A_{brunel} = \frac{\eta}{\pi} \frac{a_\perp}{a_0^2 \cos(\theta)} \left[\sqrt{(1 + a_\perp^2)} - 1 \right] \tag{3.25}$$

where the terms a_0 and $a_\perp$ are respectively the dimensionless amplitude for the total electric field and its component on $\hat{z}$. The factor η is calculated numerically [11] and found to be, in the relativistic case, $\eta = 1.66$ for $a_\perp = 2$. This effect is active only for p-polarized light.

3.4 Laser ion acceleration

Two separate mechanisms of laser ion acceleration are at present recognised and confirmed by experiments and PIC simulations: front surface and rear surface acceleration. This last is normally termed TNSA (Target Normal Sheath Acceleration). In this theoretical introduction as well as in proton acceleration experiments, I only focused on protons which acquire a final velocity in the forward direction. A proton beam emerging from the illuminated surface and propagating backwards is found in PIC simulations and experimentally observed by some experimental teams, as a consequence of the plasma expansion from that surface. When using a high contrast laser on very thin targets [12], the backward acceleration conditions are the same as the forward ones, which makes the two spectra and cutoffs comparable.

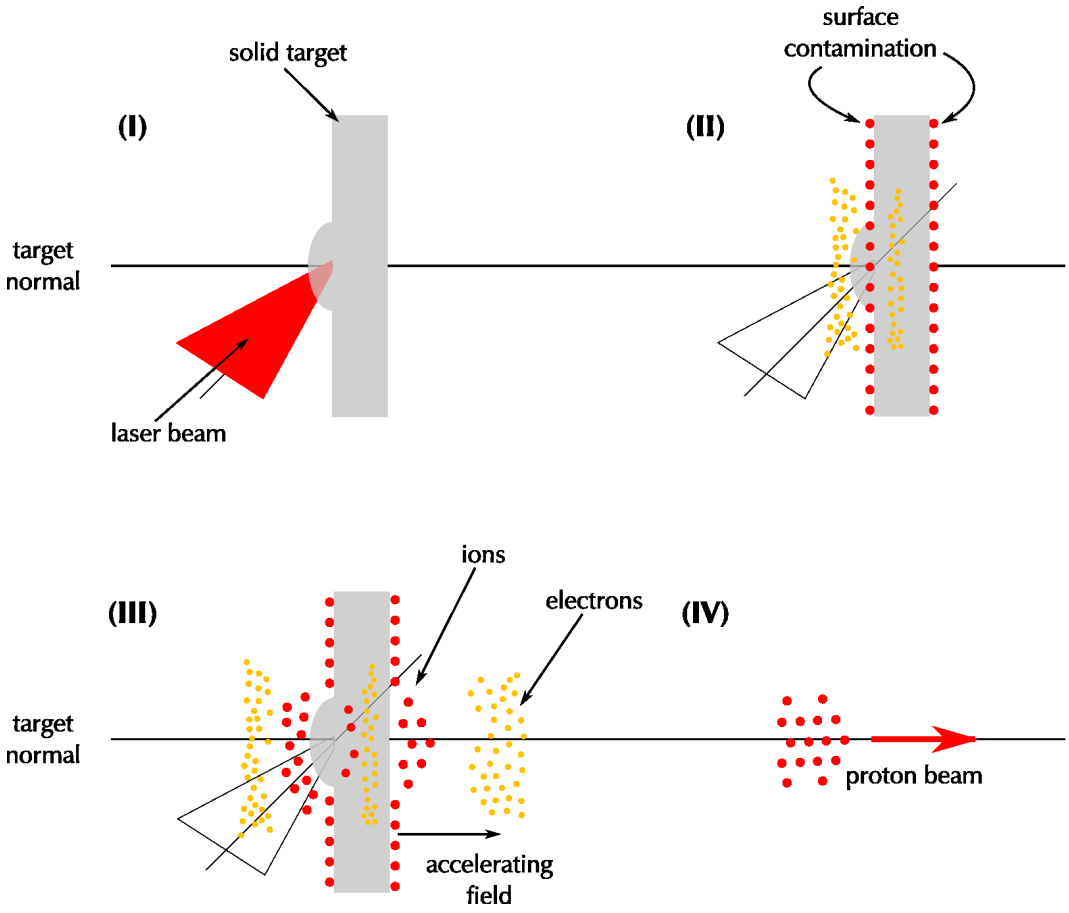


Figure 3.4: Proton acceleration scheme. The UHI laser pulse impinges on a slab of solid matter (I); the matter is ionized and the plasma heated, which produces suprathermal electron population (II). Following the propagation of electrons through the target (III) an electrostatic accelerating field is set up on the rear surface (TNSA), which extracts and accelerates ions from the back surface impurities.

3.4.1 Acceleration from the illuminated surface

Ions are accelerated at the front (illuminated) surface by the charge separation that is induced in the expanding plasma. Depending on the mechanism that dominates in the electron heating, the correlation with laser parameters changes. In cases of normal incidence or s-polarized obliquely incident light, the main charge separation mechanism at relativistic intensities is due to the ponderomotive potential, thus the acceleration gradient lies on the axis of laser propagation [83]; as a consequence of the radial components of the ponderomotive force, a non negligible charge separation on the target

normal direction can be however set up. From [83] the scaling of the cutoff energy for protons from the front surface and normal incidence of the laser is

$$E_{MAX}^{(front)} \approx 2\sqrt{2}aZ \times 0.511MeV, \tag{3.26}$$

where a is the renormalized field amplitude (2.14).

For p-polarized light, independently from the scale gradient length [40], the heating mechanisms, resonant and vacuum heating, are directed along the normal, and so the accelerated ion beam. From [39] the front ion acceleration can be seen as a balance between the thermal pressure and the laser pressure:

$$\frac{\mathrm{d}E_i}{\mathrm{d}t} = (1+R)\frac{I_0}{cl_s} - \frac{n_e k_B T_e}{L_{grad}} \tag{3.27}$$

3.4.2 Rear surface acceleration

When a hot plasma is not confined, its internal pressure leads to its expansion. We observe the formation of a density gradient, density being lower at peripheral regions, and the propagation of a rarefaction wave towards the higher densities. The local charge neutrality holds up to its local Debye length (3.2). The difference in mass between electrons and ions produces a separation of charges at the plasma/vacuum interface; the suprathermal part of the electron spectrum enhances this separation, which results in an accelerating field that drags and accelerate the initially cold ions[38, 98].
The suprathermal electron population that is produced in the laser-plasma interaction drifts through the target. Upon its arrival onto the rear surface, the matter is ionized by resistive heating and collisions; the resistive heating happens as a consequence of the ultra strong currents that re-equilibrate the charge unbalance. The divergence of the electron flux travelling through the bulk is in some part considered responsible of the decrease of ion energy that is observed on thicker targets. In [89] the divergence is measured by looking at the *Optical Transition Radiation* (OTR) emission on the rear surface of targets of different thicknesses. The measured half width at half maximum (HWHM) corresponds to an angle of 17°[4]. More recent experiments [90] repeated the

[4]The experiment was held in the *Laboratoire pour l'Utilisation des Lasers Intenses* (LULI) of the École Polytechnique and the focusing parabola had $f/3$ aperture.

measure by observing the *Coherent Transition Radiation* (CTR) emission. They underlined a double structured transport, with a hotter and narrower bunch ($\approx 10MeV$ at $\sim 7°$ HWHM), followed by a colder and more divergent ($\approx 600keV$ at $\sim 35°$ HWHM). The second one contains the larger part (some tens of percent) of the total laser energy.

In the following sections, two analytical models for TNSA ion acceleration are presented.

Isothermal Model In [74] and in later improvement [71] is presented the solution for the expansion of an isothermal plasma where $T_e \neq T_i$. At $t = 0$, a semi-infinite plasma occupies the $(-\infty, 0]$ space; ions are cold whereas an electronic temperature T_e exists. No cold electrons are taken in account and the neutrality is written as $n_{e\,0} = Zn_{i\,0}$. The electron population respects the Boltzmann distribution

$$n_e \;=\; n_{e\,0}\, \mathrm{e}^{e\Phi/k_B T_e} \tag{3.28}$$

under the action of the electrostatic potential Φ

$$\varepsilon_0 \frac{\partial^2 \Phi}{\partial x^2} \;=\; e\,(n_e - Zn_i) \tag{3.29}$$

The electric field at $x = 0$ is obtained by integration of (3.29), which produces [16]

$$E_{front,0} \;=\; \sqrt{\frac{2}{e}} \cdot \frac{k_B T_e}{e\lambda_{D\,0}} \tag{3.30}$$

During the evolution in time the electron component is supposed in equilibrium with the potential, while the ion component is governed by the two fluid equations (3.8) and (3.9) where the force on the electron component derives from the potential Φ:

$$\frac{\partial u_i}{\partial t} + u_i \frac{\partial u_i}{\partial x} \;=\; \frac{Ze}{m_i} \frac{\partial \Phi}{\partial x} \tag{3.31}$$

The set of differential equation (3.8) and (3.31) with the conditions (3.28) and (3.29) has been resolved numerically with a lagrangian code in [74]. The formation of three non-neutral areas is observed (Fig.3.5). Firstly a rarefaction front with positive charge propagates at a speed $-c_s$ in the unperturbed plasma. Secondly a separation of charges forms at the expanding front: an electron cloud followed by an ion front. By fitting the

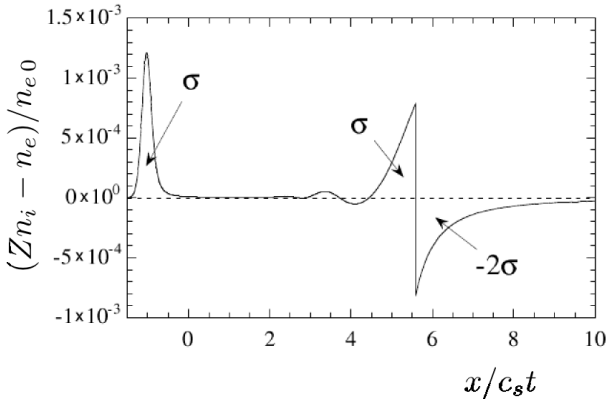


Figure 3.5: The creation of three non-neutral areas during the expansion of the hot electrons, cold ions plasma (excerpt from [71]).

numerical result for the accelerating field at the charge separation front, it is obtained:

$$E_{front} = \frac{2E_0}{\sqrt{2e + (\omega_{pi}t)^2}} \tag{3.32}$$

from which the speed of the ion front is

$$\begin{cases} v_{f,I} &= 2c_s \log\left[\tau + \sqrt{\tau^2 + 1}\right] \\ \\ \tau &= \dfrac{1}{\sqrt{2e}}\,\omega_{pi}t \end{cases} \tag{3.33}$$

where $\omega_{pi} = \left(Zn_{e\,0}e^2/m_i\varepsilon_0\right)^{1/2}$. It has to be underlined that in this calculation the charge neutrality $n_i = n_{e\,0}/Z$ is fixed at the beginning of the simulation, which makes the quantity ω_{pi} dependent on the initial $n_{e\,0}$. The ion energy is finally calculated from (3.33) to be

$$E_{max} = \frac{1}{2}Zk_BT_e\left[2\log\left(\omega_{pi}t\right) - \log\left(2\right) - 1\right]^2 \tag{3.34}$$

In the isothermal model, no energy depletion of the electron component is taken in account. The ions will indefinitely gain energy in time. Rough estimation of a meaningful "acceleration time" correlates with the duration of the laser pulse.

Adiabatic Model The experimental situation of a laser-plasma acceleration on a thin target, differs from the assumption of isothermal model by the fact that *(i)* the finite size of the target doesn't provide an infinite *reservoir* of hot electrons and *(ii)* no external source of energy exists for an indefinite acceleration time.

In [72], an improvement to the isothermal model is presented. At the initial time $t = 0$, the plasma at density ($n_{i\,0}$, $n_{e\,0} = Zn_{i\,0}$) occupies the space $x \in [-L/2, L/2]$ (Fig.3.6). The depletion in energy of the electron component is inserted in the calculation by

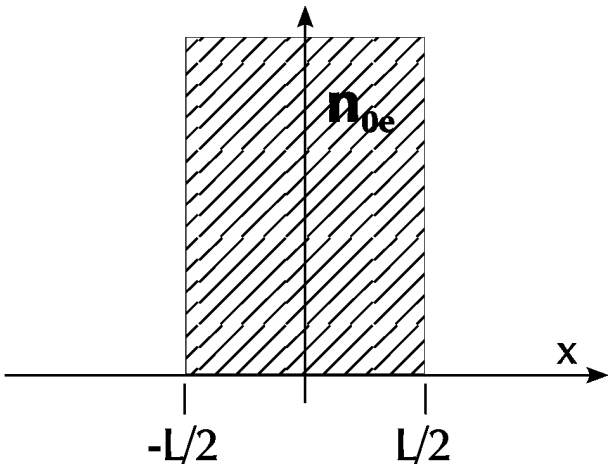


Figure 3.6: Initial condition for the adiabatic model.

$$\frac{\mathrm{d}U_{elec}}{\mathrm{d}t} = -\frac{\mathrm{d}U_{ions}}{\mathrm{d}t} - \frac{\mathrm{d}U_{field}}{\mathrm{d}t}. \tag{3.35}$$

The expansion is symmetric in the two directions, which adds the condition $E\,(x = 0) = 0$ and $v_e\,(x = 0) = 0$ for every time. The system of equations from the isothermal model (3.8), (3.31), (3.28), (3.29) is resolved by the same lagrangian code with the added condition (3.35). In these condition, the solution doesn't change from the isothermal model when $t < t_L$, defined

$$t_L = L/2c_{s\,0} \tag{3.36}$$

the time needed to the rarefaction wave to reach the $x = 0$ boundary.
The simulations show that for $t \ll t_L$ the electron temperature is constant, but that as t approaches t_L the temperature starts falling (Fig.3.7).

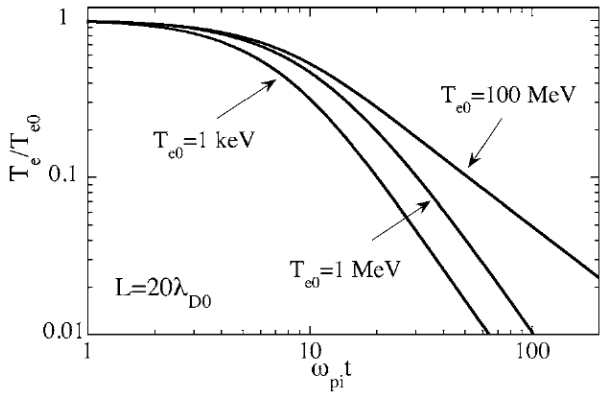


Figure 3.7: Electron temperature decreasing in the adiabatic expansion from a finite size plasma (excerpt from [72]). For an Aluminum target heated at $I = 4 \times 10^{19} W/cm^2$, $T_e \approx 1MeV$ which corresponds to $20\lambda_D \approx 0.4\mu m$. On the time scale, $\omega_{pi} \approx 40ps^{-1}$

The final ion velocity is found to be

$$v_{f,A} \;=\; 2c_{s\,0}\,\log\left[\alpha\frac{L}{\lambda_{D\,0}}+\beta\right] \tag{3.37}$$

where α and β are found to depend on the electron temperature. For $T_e = 1MeV$ it is found $\alpha = 0.49$, $\beta = 5.3$. If we compare (3.37) to (3.33), the two asymptotic behaviours are found to be similar when $L \gg \lambda_{D\,0}$ with an acceleration time of t_L (3.36).

The applicability of each of the two models to the real experimental case of a thin metal foil heated by a laser is bound to the relationship between the two parameters t_l, the laser duration, and $t_e = 2L/c$, the time needed to relativistic electrons to fill the entire thickness[5]. When $t_L \ll t_e$ the interaction between the electron burst and the non-irradiated surface happens only once, which can be considered as the case of an isothermal expansion limited to the duration of the laser pulse, $t_{acc} = t_l$. For $t_e \simeq t_l$, the hot electrons fill the target, making the adiabatic model applicable.

Corrections to the model for finite plasma scale length on the rear surface
In the experimental realization of the plasma slab by means of laser-target interaction, a density gradient on the rear (not illuminated) surface can be produced by the breakout

[5]It holds $t_e[fs] = 6.7\,L[\mu m]$

of the shock wave (see Ch.7). In [73] a correction to the model is presented, which analyses the expansion of a plasma slab when the ion-vacuum front is not steep anymore. A density gradient is introduced at $t = 0$ on the ion front, with a scale length of l_{ss}

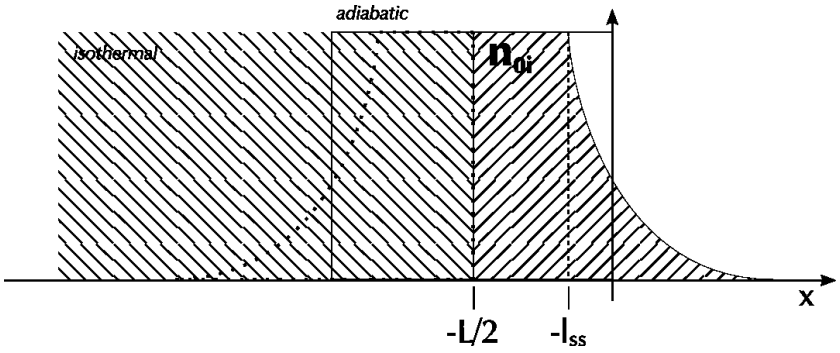


Figure 3.8: Picture of the initial condition for the two cases. In the isothermal case, the density is constant $n_i(x, t = 0)$ for $x \in (-\infty, -l_{ss}]$ and exponentially decreases on the right hand side of $x = -l_{ss}$. In the adiabatic case, the plasma initially occupies the $x \in [-L, 0]$; the symmetry axis is set at $x = -L/2$ and the two density gradients begin at $x = -l_{ss}$ and $x = l_{ss} - L$.

(Fig.3.8). The evolution of the system is analyzed for both the models (isothermal and adiabatic). According to the different representations of the initial system, the corrections are introduced as follow.

Isothermal The cold ion density distribution is

$$\begin{cases} n_i\,(x, t = 0) &= n_{i\,0} & x \le -l_{ss} \\ \\ n_i\,(x, t = 0) &= n_{i\,0} \cdot \mathrm{e}^{-\frac{x+l_{ss}}{l_{ss}}} & x > -l_{ss}. \end{cases} \tag{3.38}$$

The density gradient starts at $x = -l_{ss}$ and the constant density plasma sits in the half-space for $x < -l_{ss}$.

Adiabatic The situation depicted in Fig.3.6 is modified in a way that the new symmetry axis is $x = -L/2$ which make the plasma slab to be initially between $-L$ and 0 for $l_{ss} \to 0$. The gradient envelope is the same as defined in (3.38) for $x > -L/2$ and is symmetrized accordingly for the left hand side.

Aside of this, the physical scenario is the same as previously described, i.e. the ions are initially cold and the electron temperature is set to $T_{e\,0}$. As the system is let

evolve, by solving the set of fluid equations, the ions in the more peripheral region are accelerated by a charge separation field that is weaker than what experienced by those in the denser plasma. The differential gain in energy brings to the crossing between the two populations: the more internal and faster ions overrun the external and slower and the plasma fluid comes to a wave breaking.

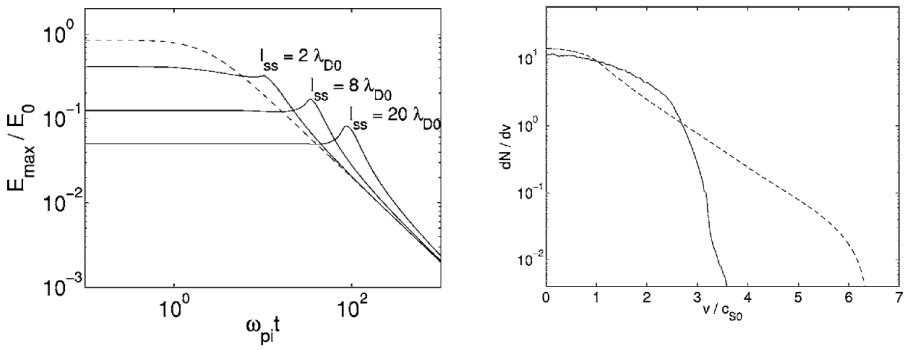


Figure 3.9: *(left)* The evolution in time of the accelerating field due to charge separation at the plasma boundary for different initial density gradient lengths. The dashed line represents the ideal ($l_{ss} = 0$) case for comparison; the peaks in the plot mark the moment when the breaking of the wave happens. *(right)* Final ion velocity spectrum for a sharp boundary (dashed) and $l_{ss} = 20\lambda_{D\,0}$ (solid) from an adiabatic simulation of $L = 40\lambda_{D\,0}$. (Excerpts from [73]).

The evolution in time of the accelerating field for fast ions is shown in Fig.3.9-*left* for different initial conditions. After an initial, constant, accelerating field, a peak appears at the moment the wave breaks; the asymptotic behaviour is found to be the same in all the cases. The accelerating field before the wave breaks is lower for longer plasma scale lengths. A simulation on the adiabatic case, see Fig.3.9-*right*, clearly shows that the final energy that is acquired from a steep boundary plasma is lower than what is achieved in presence of a gradient. Moreover, the longer the gradient, the lower the final ion velocity.

Part III

Experiments

Chapter 4

Interferometric Study of Plasma Expansion at Early Stages

The energy deposited by a femtosecond (*fs*) laser pulse on a solid target increases the temperature in a well defined region[1], creating, with a threshold of about $10^{11} - 10^{13}$ W/cm^2 [30] a solid density plasma (see Ch.3). As the superficial areas of the plasma start expanding towards the vacuum, the region of transition between the two states propagates deeper in the bulk, at a speed which depends on the initial electron temperature (Fig.4.1).

In this chapter I describe the experiment performed to directly measure the parameters of expansion of this plasma, created by a moderate intensity femtosecond pulse, in a time scale for which the shock area doesn't penetrate more than few microns in the bulk. An Aluminum plasma is produced by a $\tau = 150fs$ laser pulse, whose total energy is comparable to the total energy contained in the prepulse of a standard CPA multi-terawatt laser chain[2]. The density evolution is probed at different delays by a second laser pulse at normal incidence to the main laser pulse. The phase plane of the probe pulse, analysed by interferometry, is used to reconstruct the electron density map.

The searched timescale ($t < 100ps$) corresponds, according to hydrodynamic simulations, to the time taken by the shock to propagate over $2\mu m$.

The final comparison between experimental results and simulations allows us to follow the evolution of the plasma expansion and to infer the properties of the shock wave in the dense part of the target.

[1] In *fs* regime we use $\delta_l = c/\omega_{pe}$ as expression for the skin depth, since at room temperature, all other collisional phenomena have timescales longer than the pulse duration.

[2] Considering $contrast \cdot intensity \cdot \pi w_0^2 \cdot \tau_{ASE} = 10^{-6} \cdot 10^{19} \pi \left(3 \cdot 10^{-4}\right)^2 \cdot 3 \cdot 10^{-9} = 15mJ$.

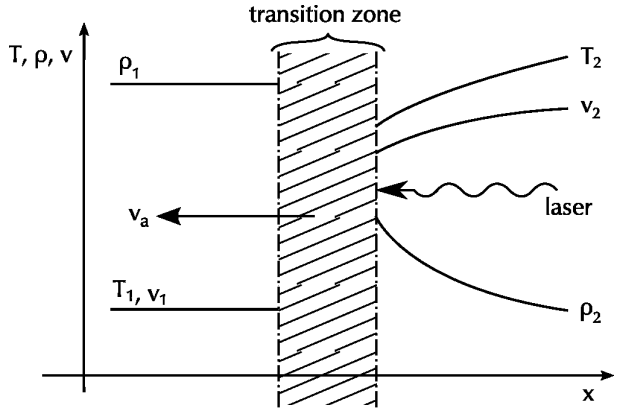


Figure 4.1: General scheme of the expansion of a solid target following laser irradiation. A transition area propagates through the unperturbed (ρ_1, T_1) bulk; a density gradient ($\{\rho_2, T_2, v_2\}(x,t)$) is formed and expands from its right surface. (Adapted from [22])

4.1 Experimental Setup

The experiment is a *pump/probe* experiment, where two separate beams from the same laser source are used, one to produce the physical situation and the second to measure the obtained parameters. This kind of experiment enables the user, given a sufficient repeatability, to measure the fast evolution of phenomena with a temporal resolution that is limited only by the duration of the probe pulse. This kind of approach is one of the key features of short pulse lasers and is possible when the duration of the probe beam is shorter then the timescale of the probed phenomenon.

4.1.1 Laser

For this experiment I used the *Salle Verte* laser facility. This is a CPA based laser system, whose basic scheme is depicted in Fig.4.3. The initial pulse is produced by a Ti:Sa crystal pumped by a CW Argon source. The repetition rate is lowered to $10Hz$ and the pulse stretched to $400ps$. Two, Nd:YAG pumped, multipass amplification stages, a 8-pass and a 4-pass, boost the single pulse energy up to $100mJ$. At this point, a birefringent window is used to rotate the beam polarization and a polarizer to split the two components in two different beams, before compression. Two independent grating compressors are then used to compress the pulses, giving two beams of $150fs$ pulses at a repetition rate of $10Hz$. The total energy after compression contained in the two

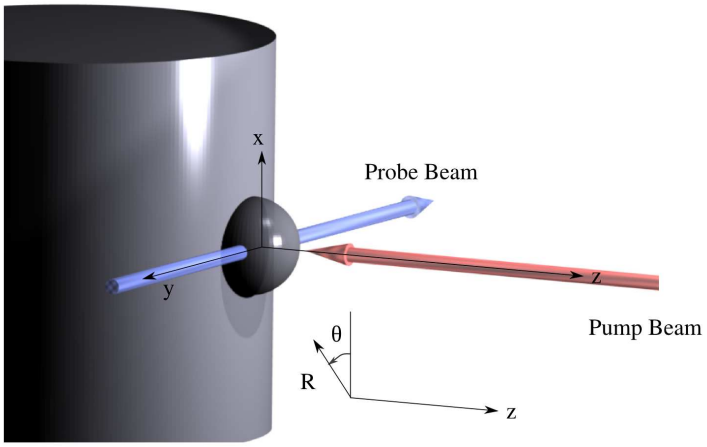


Figure 4.2: Experiment Layout

synchronized[3] pulses is about $50mJ$; the user has the freedom of changing the angle of polarization before the compression stages, deciding the ratio of energy to be sent to each beamline. The difference in optical path between the two lines is roughly $3m$ at the moment they arrive in the experimental room, having the *probe* pulse in late of about $10ns$. The laser beam is a gaussian beam with diameter of $2w = 25mm$. One of the two

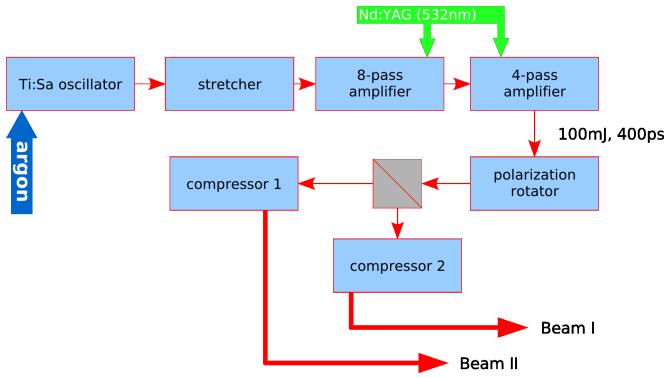


Figure 4.3: Scheme of the CPA laser chain in Salle Vert, LOA

compressors is found to have a lower efficiency so that a energy loss is introduced on one of the beamlines. In order to maximize the available energy on the *pump* beamline, the lower efficiency compressor is used on the *probe* beamline.

[3]The two compressed pulses are produced by a single pulse before compression.

4.1.2 Experiment

A brief scheme of the optical system for the plasma interferometry experiment is shown in Fig.4.4.

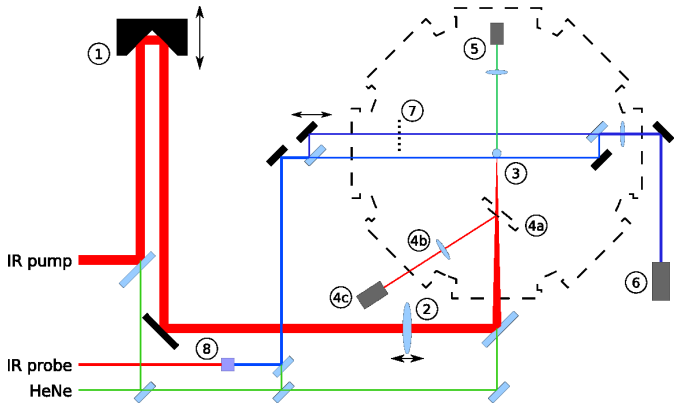


Figure 4.4: Scheme of the experiment: 1. delay line; 2. main focusing lens; 3. target; 4a-c analysis of the focal spot, including flipping mirror, microscope objective and camera; 5. imaging of lateral displacement of the target; 6. 12*bit* camera to record the interferograms; 7. shutter; 8. BBO crystal.

Pump beamline

The delay line (Fig.4.4-1) is made of two mirrors glued on a metal support to form 90^o one to the other and mounted on a step-by-step micro-controlled motor with $1\mu m$ wide steps. The motor itself is mounted and carefully aligned on a $1m$ long rail to give freedom of setting the relative delay between the two pulses.

The *pump* beam is sent to a singlet lens $f = 100cm$ (Fig.4.4-2) which focuses the beam on the target; in the ideal case (beam waist on the lens) it would produce a spot of $2w_0' = 40\mu m$ (eq. (2.7)). The focal spot is imaged by the microscope objective on the 12*bit* CCD camera (Fig.4.4-4bc) with a resolution of $0.43\mu m/pix$ [4] and the tilting of the lens is corrected to minimize astigmatism. The analysis of the focal spot (Fig.4.5) shows that the energy within the FWHM contour (marked in blue) is the 26% of total. The ratio is calculated numerically by subtracting the measured background and integrating the contoured area. There is a non-negligible amount of energy in the satellite, clearly visible in the upper-right corner. It was not possible to eliminate it by acting on lens

[4] The effective magnification is $\approx 23\times$.

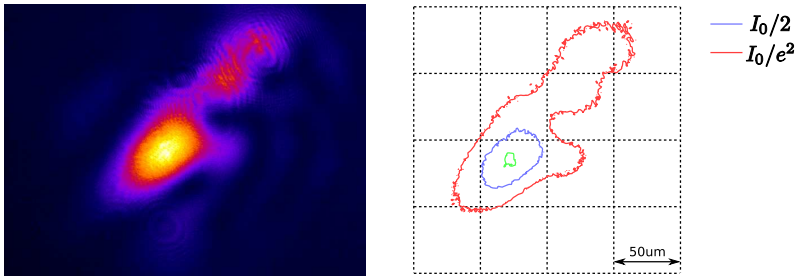


Figure 4.5: CCD image and intensity contours of the focal spot

or microscope alignments, so that we believe it to be caused by inhomogeneities on the phase front. For this experiment no adaptive optics were available to correct the phase front of the laser beam.

In the final configuration the total per-pulse energy after compression is $35mJ$; given a 59% of energy in the $2w_0$ contour (Fig.4.5-red with the satellite cut out) the resulting flux on target is $I_0 \approx 4 \times 10^{15} W/cm^2$.

Probe beamline

In order to probe higher densities in the plasma the *probe* laser beam is doubled in frequency, by a type-I BBO crystal of $2mm$ in thickness (Fig.4.4-8). Having the frequency of the *probe* different from the one that creates the plasma is also necessary to be able to filter out all the light at the *pump* wavelength being diffused during the interaction, and to produce cleaner interferograms.

It has to be underlined that the doubling process reduces the spectral content of the input pulse and acts on the spectral phase, due to different matching conditions for the various spectral components. Our input pulse has a duration $\tau = 150fs$ which corresponds, for an ideal gaussian pulse, to a spectral bandwidth of $\Delta\lambda = 12.6nm$; simulations showed that the doubled pulse will have a duration between $400fs$ and $500fs$.

Interferometry

The interference is realized in a Mach-Zender (MZ) setup. The first two components, one beam splitter and one mirror, can be seen on the same figure outside the chamber,

on the left side, and the other two on the rightmost part of the chamber itself. Hereby for the rest of this chapter, when talking about the beams inside the interferometer optics, I will distinguish the two as *probe* and *reference*, where the *reference* beam is the part of *probe* reflected by the first beam splitter and not interacting with the plasma. The

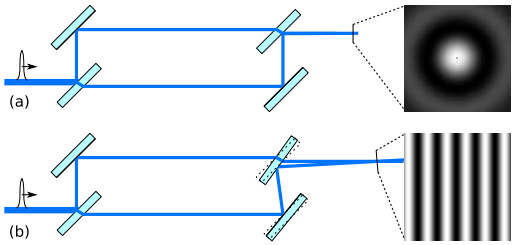


Figure 4.6: Mach-Zender interferometer setup (a); if the superposition of the two beam on the second beam splitter is done off-axis, a transverse carrier frequency appears (b).

output part of the setup is tilted, to produce a carrier frequency on the recombination of the two beams: the tilt is regulated to produce the smallest inter-fringe on the horizontal direction and to void it on the vertical. Also, the sign of the angle between the two beams is chosen so that a phase anticipation on the *probe* ($v_{phase,plasma} > c$) produces fringes *moving away* from the target shadow, and not entering it. A deeper discussion about the importance of a spatial carrier frequency is presented in section Ch.B.
A micrometric control is placed on the first mirror to be able to correct one of the MZ legs and the temporal superposition of the two pulses coming from the two parts (the probe and the reference); being $\tau_{probe} = 500fs$ the superposition will hold over a $\Delta z = 150\mu m$ wide interval[5]. The *reference* beam can occasionally be intercepted to produce a shadowgram of the target.

Imaging

The experimental information, as a phase perturbation on the *probe* beam in the MZ setup, is produced when the beam propagates through the plasma plume. In order to *transport* at its best the phase plane as it were when perturbed, a lens is inserted between the plasma and the imaging device. The first aim is to conjugate the plane orthogonal to the *probe* propagation direction and passing through the target normal (object plane) to a plane outside the interaction chamber; the second aim is to introduce

[5]The position of this mirror has to be changed when pumping down the chamber.

a magnification.
Some important choices were done about the configuration of the imaging system. First of all a focal as short as possible is to be preferred, in order to keep the lens as small as possible and to achieve the biggest numerical aperture. On the other hand a certain distance is to be kept between the Mach-Zender components and the interaction point; otherwise the metal ablation process would result in deposit of the ablated material on the optics, with a consequent degradation of the optical surfaces' quality. One should also avoid to have the object plane imaged through a beam splitter, as the thick, tilted, slab of glass between the lens and the object introduces uncorrectable geometrical aberrations.

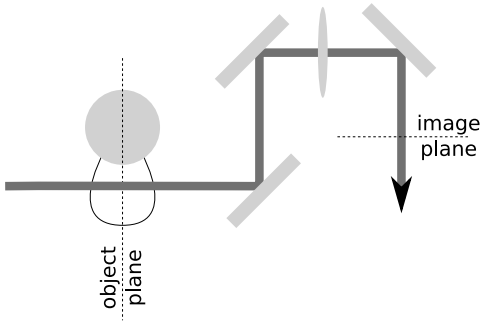


Figure 4.7: Scheme the imaging part on the plasma probe

Balancing all these factors, an achromatic doublet of $\phi = 50mm$ diameter and $f = 19cm$ (Fig.4.7) is chosen. The minimum distance from the interaction point we could place it is lower than $x = 21cm$. From the geometrical optics formula it conjugates to a plane at $380cm$ and produces a magnification $> 10\times$. The diffraction limit, calculated as

$$d = \frac{\lambda}{2n \sin(\theta)} \tag{4.1}$$

(where $\theta = \arctan[\phi/2x]$, being ϕ the lens diameter and x the object distance) turns out to be $\delta_x = 1.5\mu m$. Unfortunately this configuration (Fig.4.7) limits the freedom in the spatial carrier frequency. In fact, after having correctly aligned the lens for the *probe* side, the angle between the beams can be regulated only on acting on the far side (Fig.4.6) of the Mach-Zender, the beam-splitter and the mirror. The two beams finally

superpose on the chip of a $12bit$ linearized camera[6]. The final measured magnification on the imaging of interferograms is $m = 12.85\times$, giving a resolution of $0.77\mu m/pix$.

Target

The target is composed by an array of $200\mu m$ thin metal (Aluminum) wires. The choice fell on cylindrical target because of *(i)* their ease of alignment and *(ii)* to probe the density profile near the critical density without being masked by the rest of the target. The *probe* beam will always be tangent on the target surface and its perpendicularity to the main plasma expansion direction, i.e. the *pump* laser direction, is set by geometrical constraints of the optical setup and the target wire lateral placement. For the alignment procedure, see section 4.2.1. The holder itself is mounted on a three axis micro-controlled

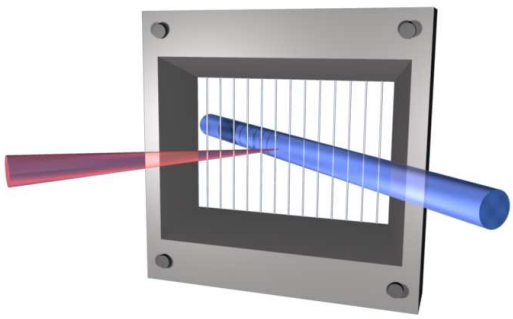


Figure 4.8: Target holder and wires; more than one pump shot was possible on a single wire, as the laser damage was not deep enough to break it.

set of motors for focusing, lateral and vertical displacement.

4.2 Experimental Procedure

The self-consistency of the entire set of data in this experiment strongly relies on the best reproduction of the system configuration for every delay. It has to be stressed that having the delay line on the *pump* beam makes the system more critical, requiring additional work and lateral realignment of the target for every important change on the delay line.

Another important parameter is the synchrony between the *pump* and the *probe* pulses. In fact, the zero point on the plasma's timescale is set by the arrival of the *pump* beam.

[6]PCO PixelFly, 12bit, 640×480 pixels of $9.9\mu m \times 9.9\mu m$.

Since I want to characterize the plasma's evolution on the absolute scale of times with its zero on the moment the expansion starts, it is necessary to carefully calibrate the optical path of the two beamlines.

4.2.1 Spatial alignments

At first the Mach-Zender components and the focusing lens are placed, in a way that the focal point of the lens is almost centered in the *probe* beam profile. The relatively long focal length eases the alignment, being the Rayleigh range $z_0 = 6mm$. At this point of the procedure a precise positioning of the *pump* spot in the *probe* beam is not fundamental, given the diameter of this last.
The imaging system on the *probe* beam path (lens and camera) is then aligned. A white, incoherent, light source is used as an object, put at the intersection between the *pump* and the *probe* axis. The target is finally put in its place, in the supposed best focus position and at the center of the *probe* beam.
The fine alignment of the target in the *pump* focus is accomplished by looking in real-time at shadowgrams[7]. A small plasma structure is formed on the target surface by the strongly attenuated *pump* beam and observed on the imaging device; if the *pump* focusing lens is moved along its axis with the micrometric translation, a range is defined where the intensity is above the threshold for target ionization, which makes a bubble visible in the target shadowgram. As neutral densities are added in the front of the focusing lens, this range becomes smaller and smaller. The procedure is stopped when this range is smaller than $200\mu m$. This position of the target is taken as a reference on the shadowgram and used to align forthcoming targets on the *pump* focal plane.
The target is also moved on its horizontal axis to keep the imaged bubble as big as possible, thus ensuring the correct lateral positioning. The reference for the lateral position is taken by the camera Fig.4.4-5 on the shadow of the target, illuminated by a HeNe laser collinear to the *pump* beam.

4.2.2 Synchrony

The delay line must be regulated to temporally superpose the two pulses, *pump* and *probe*, on the target. This condition is searched by substituting the target holder with a thin glass blade ($150\mu m$ thick) acting as a beam splitter and sending the two beams together on the lateral alignment camera. The delay line is then moved until the in-

[7]Shadowgrams are obtained by obstructing the *reference* beam in the MZ.

terference condition is produced. The interference pattern is observable within a range of $\approx 600\mu m$ on the delay line. To carry out this measurement the BBO crystal was removed.

4.2.3 Error Estimation

Two kinds of errors are introduced in the experimental procedure: the alignment of the targets and the numerical analysis of the interferograms. The second type is explored in Annex.B and it proved to be negligible when compared to alignment errors.

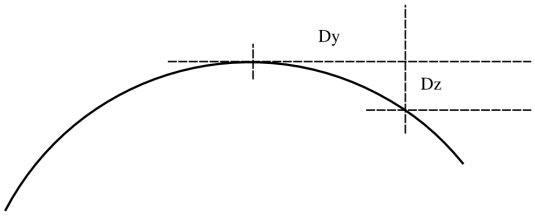


Figure 4.9: Geometrical relationship between a lateral misalignment of the target and the position of its surface on the *pump* axis.

Spatial errors

The uncertainties on the target position (Fig.4.9) are concentrated on lateral and focus alignments. A lateral misalignment would result in a surface, as seen by the *pump* pulse, with a tilt, which means a different direction of plasma expansion. Not considering the difference in physical situation (for example the loss of cylindrical symmetry seen by the *probe*), the result would be in higher density regions seen nearer to the target surface. Considering that on the lateral alignment camera the target boundary is seen with a resolution better than $1\mu m/pix$, a misalignment $10pix$ would have a negligible consequence on the final result.

The positioning in focus, where the reference is seen on the shadowgraphy on the interferogram camera, is more important, as a misalignment here, while not affecting the physics of the interaction, would directly result in a wrong measure of the distance between a given density and the original surface. In the alignment of a new target, uncertainties are introduced by diffraction effect on its boundary (see Fig.4.10a): its

position in z can be defined in a range of $\pm 4pix = \pm 3\mu m$. I use this quantity as the uncertainty on the z value of experimental measurements.

Temporal errors

As introduced in 4.2.2, the temporal superposition of the beams is defined down to $600\mu m$ on the delay line. This range introduces a systematic uncertainty of $\pm 2ps$ on the temporal axis. Aside of this, every movement of the delay line has a precision of $\approx 1\mu m$, which introduces a negligible error of $\pm 4fs$.

4.3 Experimental Data

For each delay time, four images need to be taken, namely a shadowgraphy before (Fig.4.10a) and after (Fig.4.10d) the *pump* shot, a reference interferogram (Fig.4.10b) and the interferogram with the plasma (Fig.4.10c). The procedure is repeated at least twice for delays between $0ps$ and $100ps$, by steps of $3ps$.

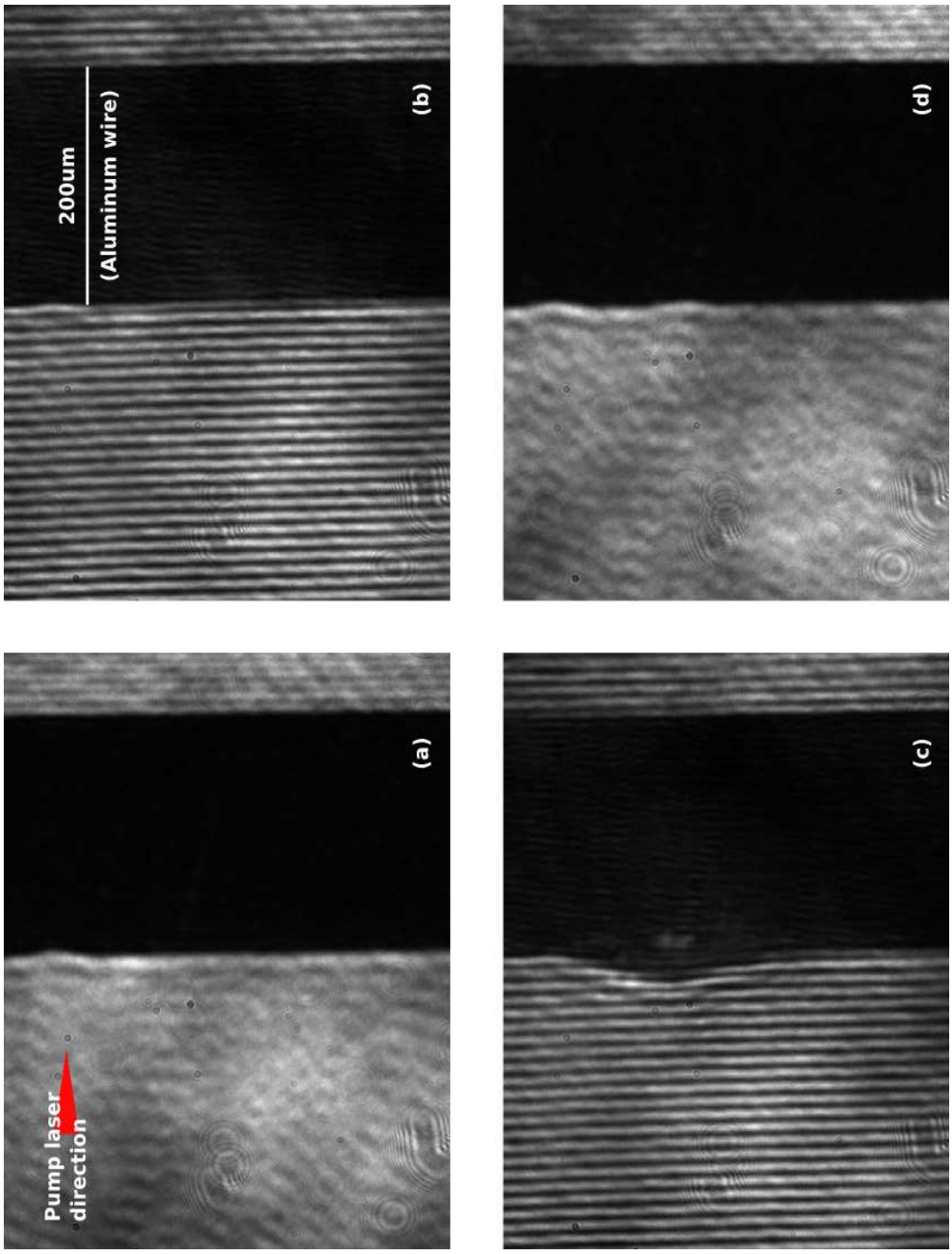


Figure 4.10: A set of images recorded for a single delay ($t = 90ps$). (a) Shadowgraphy before the *pump* shot; (b) reference interferogram; (c) plasma interferogram; (d) shadowgraphy after the shot, the hole is clearly visible on the left side of the target. (Images have a resolution of $1.2\mu m$; inter-fringe is $\lambda_{het} \approx 10\mu m$)

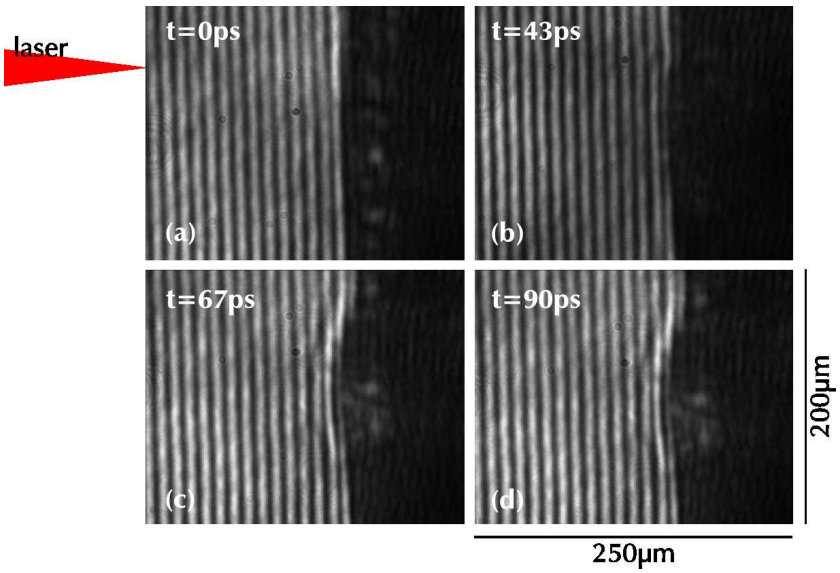


Figure 4.11: Plasma expansion at four different delays : (a) $0ps$, (b) $43ps$, (c) $67ps$ and (d) $90ps$.

As the delay line is moved, a black bubble is seen to form, starting $6-7ps$ later than the *pump* pulse and to expanding as time passes. The black area, where complete absorption or deviation of *probe* happens, is surrounded by deformed fringes. In Fig.4.11 interferograms recorded at different times are shown.

The interferograms are filtered and the phase map is calculated and inverted to obtain the 2D density map (see Ch.B). The filtering process is accomplished in the Fourier space by limiting the information that is contained in the image to certain physical constraints, like the size of the focal spot and the parameters of the optical system that created it (see B.2.1 for details).

The phase map is reconstructed from the filtered image and the heterodyne carrier removed by 2D linear fit on the phase plane[8].

On behalf of cylindrical symmetry of the created plasma, the symmetry axis (Fig.4.12-*upper*) is searched on the phase planes and the phase cuts on $\phi_{exp}(x, z = constant)$ are symmetrized by averaging the two halves. The obtained phase matrix is inverted from (x, z) to (r, z) by the Abel formula (4.2)-I and electron density calculated by (4.2)-II.

[8] If the phase on the interferogram is represented by $\Phi(\underline{x}) = \underline{k}_{het} \cdot \underline{x} + \varphi(\underline{x})$, the heterodyne component $|\underline{k}_{het}| = 2\pi/\lambda_{het}$ can be removed by directly subtracting the $\underline{k}_{het} \cdot \underline{x}$ plane.

$$\begin{cases} \left(\dfrac{\partial\phi}{\partial r}\right)(r,z) &= -\dfrac{1}{\pi}\displaystyle\int_r^{r_0} \dfrac{\partial\phi_{exp}/\partial x}{\sqrt{x^2-r^2}}\mathrm{d}x \\ n_e\,(r,z) &= \dfrac{m_e\epsilon_0 c^2}{e^2}\left[2k_0\left(\dfrac{\partial\phi}{\partial r}\right)+\left(\dfrac{\partial\phi}{\partial r}\right)^2\right] \end{cases} \tag{4.2}$$

The latter – see (B.19) – makes use of the dependence of the refraction index on the electron density for transverse *em* waves in a cold plasma. The analysis of the entire

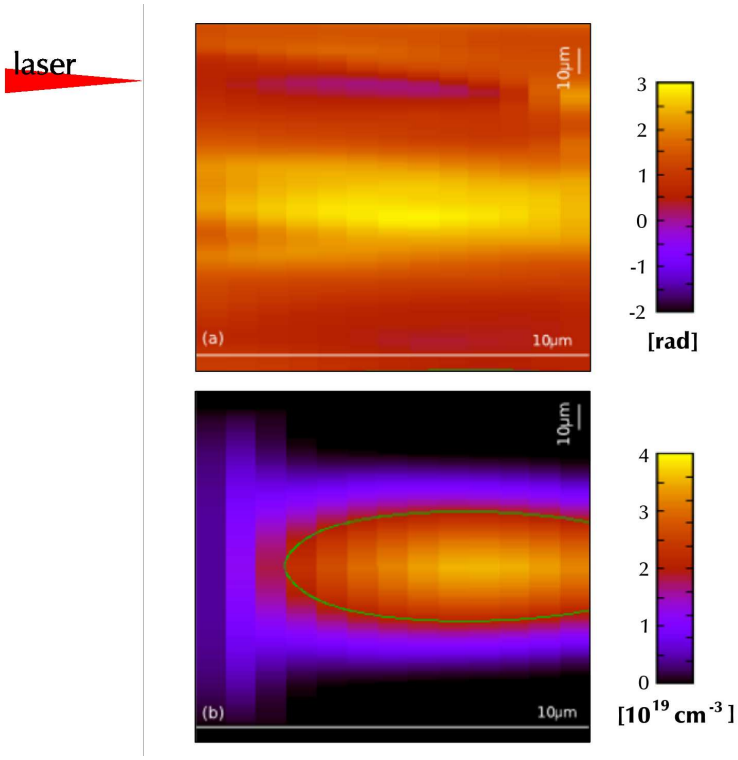


Figure 4.12: 2D map of plasma expansion at a delay of for $\Delta t = 67ps$ (Fig.4.11c); (a) phase map from the interferogram; (b) density map after Abel inversion (green line represents the isodensity contour at $n_e = 2 \cdot 10^{19}\, cm^{-3}$).

collection of images provides the set of 2D maps of electron densities from $6ps$ to $100ps$. The set of measured densities ranges between $2 \times 10^{18} cm^{-3}$ and $4 \times 10^{19} cm^{-3}$. The error introduced by the phase retrieval process, propagated through the Abel inversion – (B.29) – results in uncertainties on the density values in the range of $10^{12} - 10^{13} cm^{-3}$, which are smaller than other sources of uncertainty.

4.4 Results and Comparison with Simulations

Simulations

Within the timescale we measured the plasma expansion, its longitudinal dimension (z) remains small compared to the focal spot size. We can then neglect transversal (r) expansion and simulate the plasma expansion with the 1D1/2 Lagrangian hydrodynamic code Chivas. It is a mono-dimensional cylindrical code where the meshes have a time dependent transverse size, expanding radially with a velocity that depends on the pressure and density existing in the cell[44]. This code is adapted to short pulse laser-matter interaction by solving the Helmholtz equation[9], and it includes the Nohel code, which is an atomic physics model used to describe the ionization, the equation of state and the opacity of matter. For numerical convenience, we have considered a thinner Aluminium target ($8\mu m$). Since the shock wave propagates only over $2\mu m$ inside the target after $100ps$, we are confident that our numerical results can satisfactory be compared with the experimental case ($200\mu m$). This bulk material is irradiated by a laser pulse which has a temporal FWHM of $150fs$ and a focal spot of $40\mu m$ containing $16mJ$ of energy. The code simulates as well the propagation of a transitional zone – shock wave, showing a density higher then the solid density of the target – between the unperturbed material (towards the inner part of the target) and the "ablation front" where the high temperature results in the production of a plasma bubble, which expands towards the vacuum (Fig.4.1). The code is able to simulate correctly the rarefaction until a density of $10^{19}cm^{-3}$.

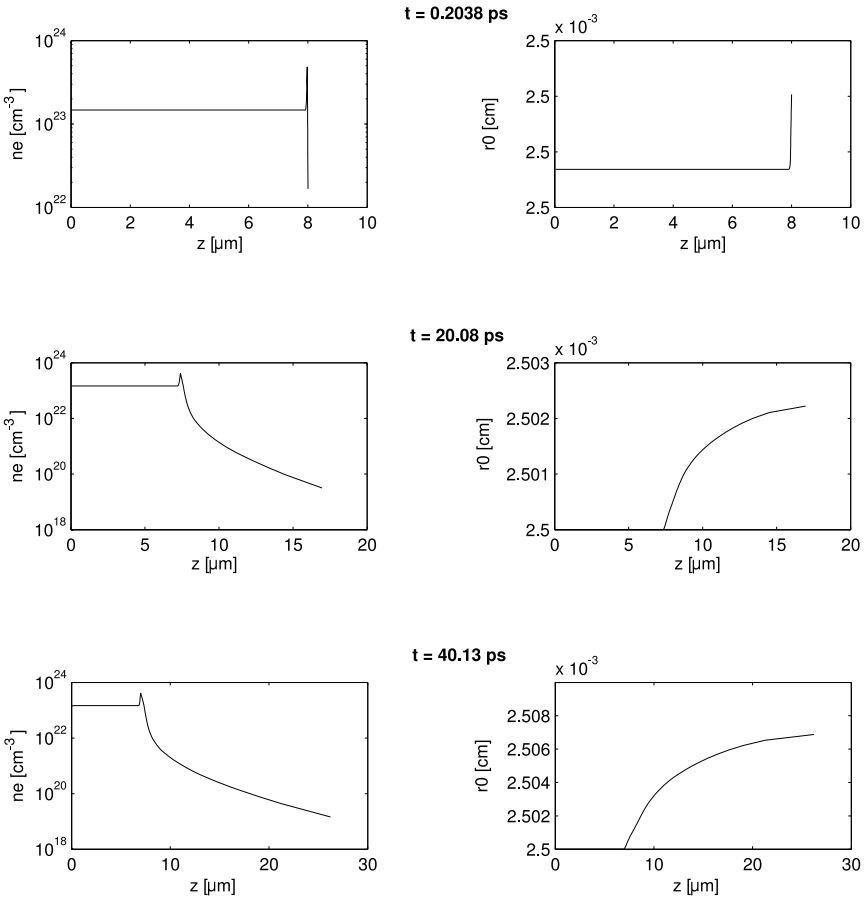


Figure 4.13-a: Chivas simulations for the plasma plume produced on an Aluminum target by a $\tau = 150fs$ long laser pulse (coming from the right to the left) with $16mJ$ of energy in a gaussian spot of $50\mu m$ FWHM diameter. The initial, unperturbed target boundary is at $z = 8\mu m$. At $0.2ps$ the laser pulse is over and the shock is created. On the left it is shown the density decreasing from the bulk density (left side of the plot) towards the vacuum (right side). On the right, the transverse size (radius) of the plasma plume.

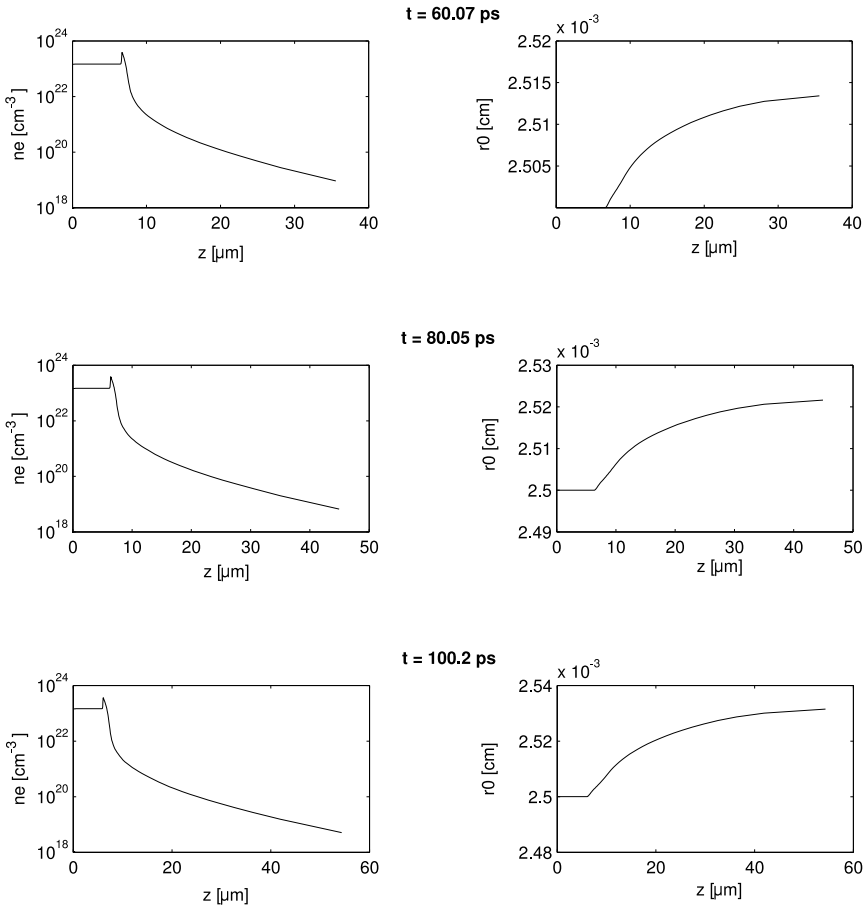


Figure 4.13-b: (*cont. from Fig.4.13-a* for times from 60*ps* to 100*ps*). For the entire time range the transversal growth is negligible if compared to the propagation over $z-$axis. This confirms the use of $1D\,^1/_2$ simulation code.

At $t = 0ps$ the laser pulse starts to heat the electrons in the target; its interaction with the bulk stops at $t = 0.2ps$. The maximum reached temperature is $\approx 250eV$. At this point a corona starts to expand and the shock wave to penetrate deeper in the bulk. After the first $20ps$ a significant plume is already visible. The simulation is stopped at $t = 100ps$: by this time the shock has penetrated $\approx 2\mu m$ of material, while the plasma front (at the lowest density considered by the code) has reached $\approx 60\mu m$ from the target.

Comparison with experimental data

The simulated data spawns over a density range that is bigger than what experimentally measured. Neglecting what is situated (in the simulations) beyond the $8\mu m$ boundary, not visible by the *probe* beam because masked by the "walls" of the crater, the densities in the plasma gradient range between $n_e = 10^{23}\, cm^{-3}$ to $n_e = 10^{19}\, cm^{-3}$. The critical density for the *probe* beam is $n_{c,400nm} = 6.88 \times 10^{21}\, cm^{-3}$ which is in contrast with the maximum density measured on the interferograms of $\approx 4 \times 10^{19}\, cm^{-3}$. There are many possible reasons for this value being $\ll n_c$. First of all, the entire region with densities between the critical density at $400nm$ and the highest measured density has a maximal length (from simulations) of $\approx 7\mu m$, which corresponds to $3/4\, \lambda_{het}$([9]) on the interferogram; this means that the information on two orders of magnitude in electron density is contained in a deformation of just half a fringe. On the other hand, the attenuation of the beam, while travelling through high density regions, significantly worsen the contrast and the signal to noise ratio, making that part of the interferogram more difficult to analyze. See for example the weak contrast of the rightmost perturbed fringe in Fig.4.11c and Fig.4.11d.

By plotting the simulated density with experimental data (like in Fig.4.14) we find the superposition to be fair, confirming the correlation between the measured densities and their distance from the target. The correlation is even more clear looking at the plot of the propagation, in time, of a test density in comparison with the simulated expansion (Fig.4.15).

[9] The heterodyne spatial wavelength.

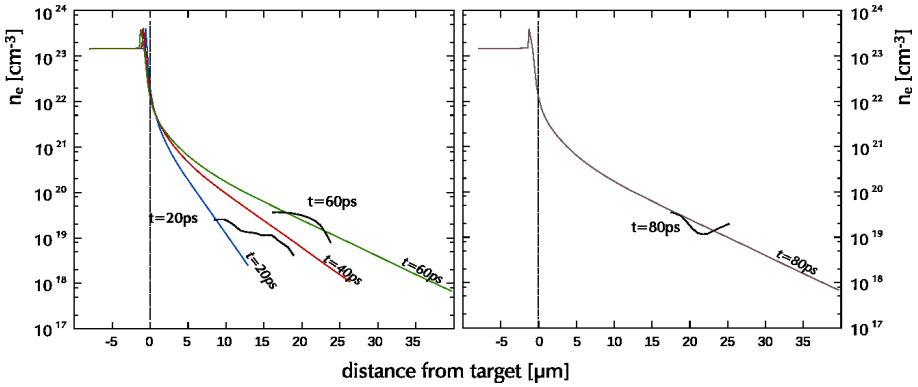


Figure 4.14: Electron density on the symmetry axis vs. distance from target at three different times: (a) 20*ps* (40*ps* dotted), (b) 60*ps* and (c) 80*ps*. Dotted vertical line is the unperturbed target boundary, laser is coming from the right.

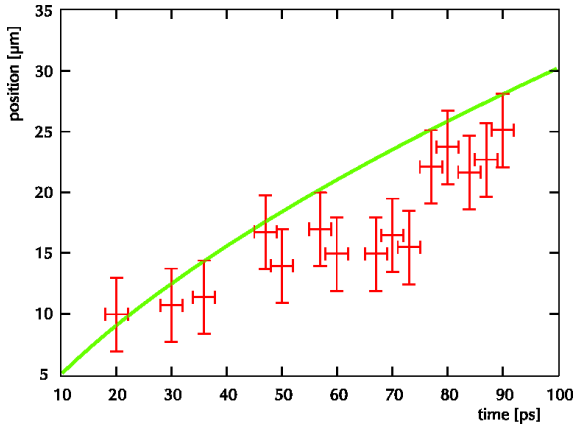


Figure 4.15: Propagation of a constant density front ($n_e = 2 \times 10^{19} cm^{-3}$); the solid line represents the extrapolation from simulated data, crosses are experimental data. Error bars are from alignment uncertainty (see 4.2.1, 4.2.2).

From the simulated density profiles we gain informations concerning the position of the front at the critical density and the gradient length in front of the target (Fig.4.16-*left*). Moreover we can follow the propagation in time of the shock inside the bulk material (Fig.4.16-*right*).

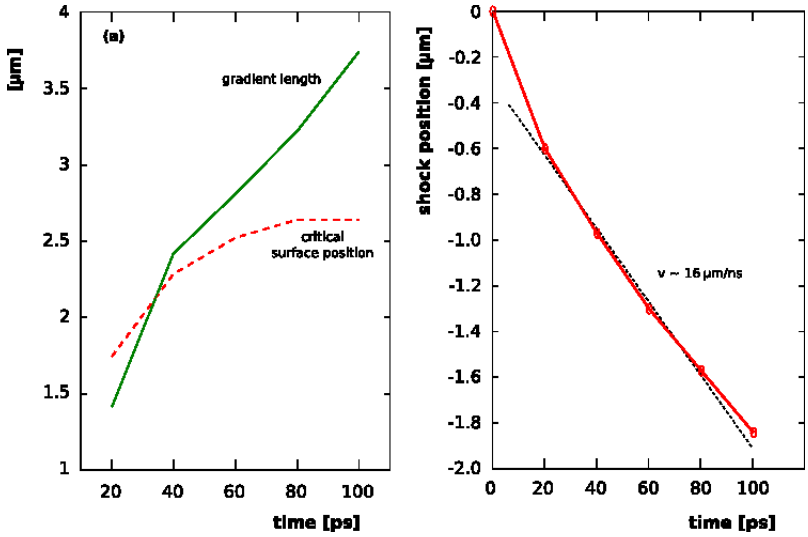


Figure 4.16: Temporal evolution of the plasma profile: *(left)* the dotted line represents the propagation of the critical density front ($n_c = 1.72 \times 10^{21} cm^{-3}$, for $\lambda = 800nm$); the continuous line represents the gradient length (evaluated between n_c and n_c/e); *(right)* propagation of the shock wave in the bulk material (0 marks the position of the target surface before interaction).

4.5 Discussion and Conclusion

The superposition between the simulated density profiles and on-axis experimental points is rather good, see for example Fig.4.15, confirming the correct 1D modelling of plasma expansion at short times. Further data analysis (not reported) also shows the lateral expansion to be negligible within the first $150ps$. The set of density that could be experimentally probed is limited, on the upper side, to $\approx 4 \times 10^{19} cm^{-3}$.

The simulations also show the propagation of the shock wave in the bulk (see the over-density peaks in Fig.4.14, left of the unperturbed boundary). If we plot shock the position versus time (Fig.4.16b) we distinguish two propagation regimes. At the beginning, during the first $20ps$ the shock wave rapidly propagates inside the target and then

reaches a stationary regime. When the measurement timescale becomes much greater than the laser duration, an almost constant velocity is observed; a linear fit gives a velocity of $v = 16\mu m/ns$. If we consider the shock wave behaviour to be independent on the target thickness, the plot in Fig.4.16b enables us to estimate the time at which the shock would reach the rear side of a thin foil. For example, we observe that a target $1\mu m$ thick target would be completely traversed in about $41ps$.

Looking at the gradient length (defined as the distance needed for the electron density to drop of a factor $1/e$ from the critical density for $\lambda = 800nm$) in Fig.4.16a, we find a similar behaviour; after the first $40ps$, when the density profile expands to about $2.5\mu m$, the scale expansion continues at a velocity of $v_{exp} = 20\mu m/ns$. This expansion velocity corresponds to the sound velocity of a plasma heated to $20eV$, which is in agreement with the temperature evaluated numerically.

Chapter 5

Reflectometry Study of Thin Metal Foil Perturbation by a Moderate Intensity Laser Pulse

5.1 Introduction

In chapters Ch.3 and Ch.4 I introduced a few basic concepts on the interaction between a laser pulse and a solid target. Here I focus on the propagation of the shock wave through the bulk and in particular on the evolution of the shock effects on the non irradiated surface (the back surface).

The detrimental effects produced by a laser pedestal on the back surface can reduce or destroy the target normal sheath acceleration (TNSA) according to the timescale of propagation of the shock wave through the thin foil. From the moment the interaction begins between the pulse pedestal and the overdense matter, the shock wave starts propagating. Once it arrives at the back side of the foil, a new plasma starts expanding in that direction: when a sufficient plasma gradient exists on the surface, the TNSA acceleration is reduced due to the lengthening of the Debye length.

In this experiment I use a short laser pulse to monitor the evolution of the electron temperature on the back side of a thin metal foil. The electron temperature is measured through the change in reflectivity of the metal surface. The shock wave is created by a femtosecond laser ($\tau = 150fs$, $I \approx 10^{15}W/cm^2$) with the same characteristics than the one used for the experiment in Ch.4. This, in turns, will enable us to close the loop between the gradient scale length that is created on the front surface (Fig.4.16) and the

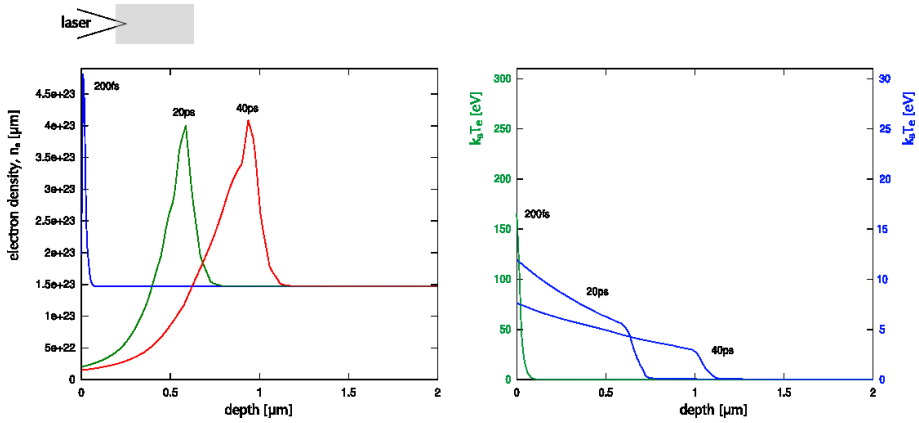


Figure 5.1: Excerpt from the simulations in Fig.4.13 for the evolution beyond the target boundary. *(left)* The shock propagates deeper into the bulk; *(right)* the evolution of the electron temperature. (The 20*ps* and the 40*ps* plots in the right graph are referred to the rightmost scale of temperature).

propagation of the shock through the bulk material.

5.2 Reflectometry Measurements of a Metallic Surface

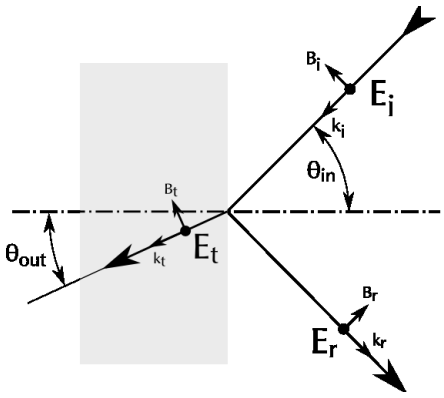


Figure 5.2: Reflection of an S-polarized wave.

The reflectivity of a cold metallic surface, when no density gradient is present, is calculated from the Fresnel coefficients. Let's consider the problem in the geometry depicted in Fig.5.2. When the S-polarized wave arrives at the interface between the metal (ω_{pe},

ε) and the vacuum (ε_0), the reflected and refracted waves are produced. The calculation is carried out by setting the three fields $\underline{\mathrm{E}}_i(\underline{\mathrm{x}}, t)$, $\underline{\mathrm{E}}_r(\underline{\mathrm{x}}, t)$ and $\underline{\mathrm{E}}_t(\underline{\mathrm{x}}, t)$[1] to satisfy the continuity relationship on the interface. Having defined $r_S = E_r/E_i$, it results:

$$r_S = \frac{\cos\theta - \sqrt{\varepsilon - \sin^2\theta}}{\cos\theta + \sqrt{\varepsilon - \sin^2\theta}} \tag{5.1}$$

which defines the reflectivity coefficient as

$$R_S = |r_S|^2, \tag{5.2}$$

where θ is the impinging angle and ε the (complex) dielectric constant for the metal. From the Drude model it holds

$$\varepsilon = 1 - \frac{\omega_{pe}^2}{\omega\,(\omega - \mathrm{i}\nu_{ei})} \tag{5.3}$$

which inserts the contribution of the electron-ion collision frequency ν_{ei}. For an over-dense material $\left(\frac{n_e}{n_c} \gg 1\right)$ the behaviour is defined by the ν_{ei}/ω ratio. If $\nu_{ei}/\omega < 1$, the medium has a good reflectivity when its collisionality is low, i.e. for temperatures lower than some eV or higher than several tens of eV. To estimate the term ν_{ei} I use the Eidmann-Hüller interpolation between the Spitzer collision frequency for the hot plasma and the electron-phonon collision frequency for the cold limit[14, 94, 20].

The Spitzer formula for the collision frequency is

$$\nu_{Spitzer} = \frac{4}{3}\sqrt{2\pi}\,\frac{Z^* e^4}{16\pi^2\varepsilon_0^2}\,\frac{m_e n_e}{(m_e k_B T_e)^{3/2}}\ln\left(\Lambda'\right) \tag{5.4}$$

where $\Lambda' = \left(1 + (b_{max}/b_0)^2\right)^{1/2}$ is the Coulomb parameter. The terms b_0 and b_{max} are respectively *(i)* the impact factor for a $\pi/2$ deflection in a Rutherford scattering and *(ii)* the maximum impact factor for a deflection to happen, before the electrostatic field of the scattering center is shielded by the plasma. Here they are used in the form

[1] Usual representation: $\underline{\mathrm{E}} = \underline{\mathrm{E}}_0 \exp[\underline{\mathrm{kx}} - \omega t]$.

$$\begin{cases} b_{max} &= \sqrt{\dfrac{k_B T_e}{m_e}} \dfrac{1}{\max(\omega,\, \omega_{pe})} \\ b_0 &= \max\left(\dfrac{h}{\sqrt{k_B T_e m_e}},\, \dfrac{Z^* e^2}{4\pi\varepsilon_0} \dfrac{1}{k_B T_e} \right), \end{cases} \tag{5.5}$$

where to the common corrections (λ_{Debye} for b_{max} and classical calculation for b_0) are added[2].

In the cold limit the considered collision frequency is the $\nu_{el-phonon}$ between electrons in the material and phonons:

$$\nu_{el-phonon} = k_s \frac{e^2}{4\pi\varepsilon_0 \hbar v_F} \left(2 - \frac{v_F^2}{c^2}\right) \left[1 + \left(0.13 \frac{\hbar\omega_{pi}}{k_B T_i}\right)^2\right]^{1/2} \frac{k_B T_i}{\hbar} \tag{5.6}$$

$$\approx 2k_s \frac{e^2 k_B T_i}{4\pi\varepsilon_0 \hbar^2 v_F} \tag{5.7}$$

where ω_{pi} is the ion plasma frequency, T_i the ion temperature and it is used the expression for the Fermi's velocity $v_F = (\hbar/m_e)\left(3\pi^2 n_e\right)^{1/3}$. The k_s parameter in (5.7) is calculated to fit the tabulated data[3].
The set of frequencies between the two extreme cases is extrapolated by

$$\nu_{ei}^{-1} = \nu_{Spitzer}^{-1} + \nu_{el-phonon}^{-1}. \tag{5.8}$$

The evolution of the reflectivity is numerically obtained from (5.2) with the values obtained from (5.8) for different electron temperatures in the case of an impinging angle of $\theta = \pi/4$ and $\omega_{laser} = 2\pi c/\left(\lambda_{probe} = 400nm\right)$.

Notes on Ion temperature The collision frequency in the cold limit depends on the ion temperature. For a given electron temperature, a decrease in the ion temperature will reduce the collisionality in the cold limit, which increases the contribution of ν_{cold} (5.7) to ν_{ei} (5.8); this, in turns, increases the depth of the reflectivity drop (see Fig.5.3).

[2]The max() term in (5.5)-i corrects the λ_D when an evanescent wave is present; the first term in (5.5)-ii sets that no impact parameter smaller than the deBroglie's wavelength of the impinging particle should be considered.

[3]The approximation to the cold metal solid is done via $v_F \ll c$ and $\hbar\omega_{pi} \ll k_B T_i$. It is set $k_s = 58.9$, calculated from the condition $\nu_{el-phon}\left(T = 300K\right) = n_e e^2 \rho / m_e$, being the tabulated resistivity of aluminum $\rho\left(T = 300K\right) = 26.50n\Omega \cdot m$.

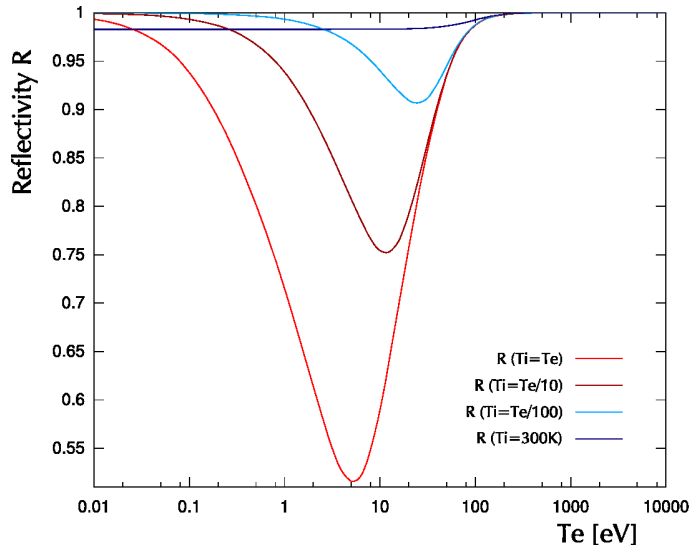


Figure 5.3: Reflectivity vs. electronic temperature from the Eidmann-Huller interpolation of electron-ion collision frequency, for an Aluminum bulk at solid density with $\lambda = 400nm$ s-polarized light impinging at 45°. Different ion temperatures are shown.

5.3 Experimental Setup

As in the previous experiment two beams are obtained from the laser chain of the *Salle Verte* (Ch.4). The most intense one is focused to produce a plasma on thin Aluminum foils ($3\mu m$, $2\mu m$ and $800nm$); the less intense is delayed through a variable delay line, doubled in frequency and reflected and diffused by the rear surface of the metallic target. Here's a brief description of the realized setup.

Pump Beam The beam is focused by a single lens of $f = 1000mm$. The focal spot is sent by a removable mirror to a microscope objective and imaged on a 12bit camera (Fig.5.4-5); the image is used to correct the lens tilt, controlling the aberrations, and to measure the size and the energy content of the focal spot. The obtained spot exhibits (Fig.5.5) an average diameter on the $1/e^2$ (fwhm) of approximately $58\mu m$ ($34\mu m$). The corresponding Rayleigh range is $z_0 = 3.5mm$. The total energy on the *pump* beam line is about $E_L = 20mJ$, which results in a peak intensity of $I_0 = 8 \times 10^{15} W/cm^2$.

Probe Beam The *probe* beam, with energy lower than $2mJ$ is first reduced in diameter by a telescope, $f_1 = 500mm$, $f_2 = 100mm$. This operation has the dual purpose

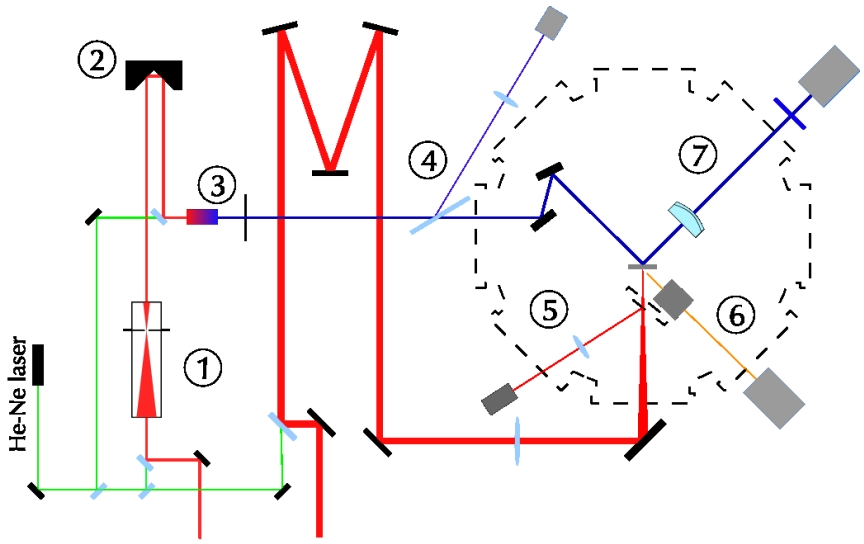


Figure 5.4: Scheme of the experimental setup: 1. telescope and spatial filter, 2. delay line, 3. BBO crystal, 4. glass blade and energy reference camera, 5. focal spot imaging, 6. target focus reference, 7. collection of the diffused light (doublet, filter and camera).

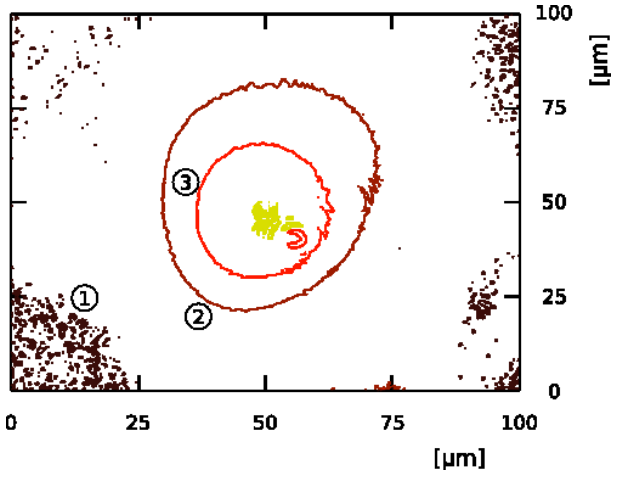


Figure 5.5: Level contours of the focal spot, as measured by the 12bit camera; 1. background, 2. $1/e^2$, 3. FWHM.

of *(i)* increasing the beam intensity without focusing it and *(ii)* enhancing its quality (the transverse profile is cleaned on the focal plane of the first lens by a pinhole of $\phi = 200\mu m$). I decided to avoid the usual procedure in reflectometry measurements of focusing the probe beam on the target surface. In fact, the poor optical quality of

common thin targets, in conjunction with the increased beam divergence, would result in a larger spread of the reflected/diffused light cone.
To be able to analyse the reflectivity map, a precise knowledge of the fluctuations in laser intensity, between the recording of the reference and the shot image, is needed. For this purpose, a glass blade ($150\mu m$, Fig.5.4-4) sends a small part of the *probe* energy to a 12bit camera. For every shot, the integrated image on this camera is used as an intensity reference.
The area on the target surface that corresponds to the pump axis is imaged by an achromatic doublet on a $16bit$ camera (Andor DV434). The doublet is a $f = 150mm$, $\phi = 75mm$; its very large numeric aperture lets us collect the biggest part of the reflected/diffused light and obtain a good magnification. The images in blue light (*probe*) on the camera (Fig.5.4-7) have a final resolution of $2.38\mu m/pix$, producing a total imaged square of $\approx 2.5mm$ by side (1024×1024 pixels).
The alignment of the doublet proved to be very time consuming, and it is done in incoherent white light. A bandpass optical filter (Schott-BG39) is inserted in front of the Andor camera, to minimize the signal that is produced by the plasma self emission and by the infrared light that is diffused in the experimental chamber.
Due to the very high level of inhomogeneities on a typical target surface, getting worse as thickness gets smaller, minor corrections on the Andor camera are necessary. For this purpose the camera is mounted on a micrometric motorized translation and its position corrected when needed. An additional camera (Fig.5.4-6) images the target front surface illuminated in white light with weak magnification ($\approx 2x$) at an angle of 45°. The spot that is produced on this camera by the green alignment beam, collinear with the IR pump beam, is used as an absolute reference on the target position on the focal axis. In fact, given the angle between the focal axis and this imaging axis, a displacement of the target in focus translates into a lateral movement of the imaged spot. This configuration gives a $10\mu m$ sensibility on the target position (i.e. $10\mu m$ of target translation will move the spot on the monitor by a quantity of half of the spot itself). This kind of approach proved to be simple and very effective, in a way that it is used in forthcoming experiments in this manuscript.

Target Alignment The positioning of the target foil along the focus axis is searched for by looking at the surface ionization, that is produced whenever the pump beam interacts, over-threshold, on the thick target holder ($4mm$ aluminum). Moving this

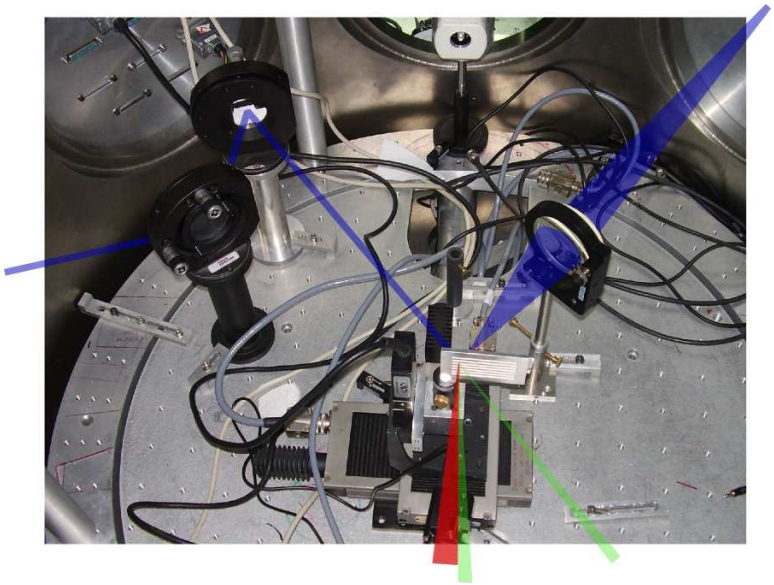


Figure 5.6: Experimental setup with beam paths.

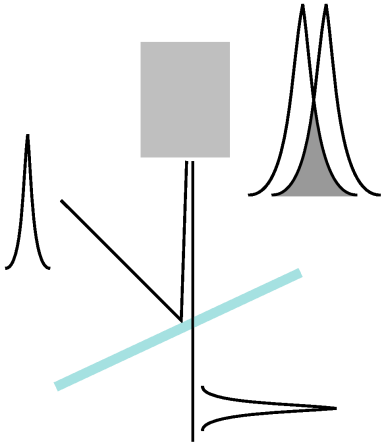


Figure 5.7: Principle of synchronization of the beams.

surface along the pump axis lets us to define a range around the best focus position: its boundaries are defined by the positions where the ionization effect disappears. Neutral densities are added in front of the focusing lens to shrink this range, until smaller than the calculated Rayleigh depth. Its halfway position is taken as a best focus.

Synchronization of the Beams The synchronization condition is searched through the interference condition in the superposition of the two beams. The BBO crystal is removed and a $150\mu m$ thick glass blade in the target holder is used to superpose the two beams on the chip of an 8bit CCD camera. The energy balance between the two is set to enhance the contrast in the interferometry image. The interference condition is found in a range of $1mm$ on the delay line. This means that we're left with an uncertainty on the temporal scale of at least $7ps$. Our supposed $t = 0$ position is set in the middle of this range.

5.4 Experimental Data

The delay time is varied in a range between $0ns$ and $2ns$ and the reflectometry images are recorded without and with pump beam for three different target thicknesses ($3\mu m$, $2\mu m$ and $0.8\mu m$). A third image is taken after the pump shot; an example of a set of experimental images is presented in Fig.5.8.

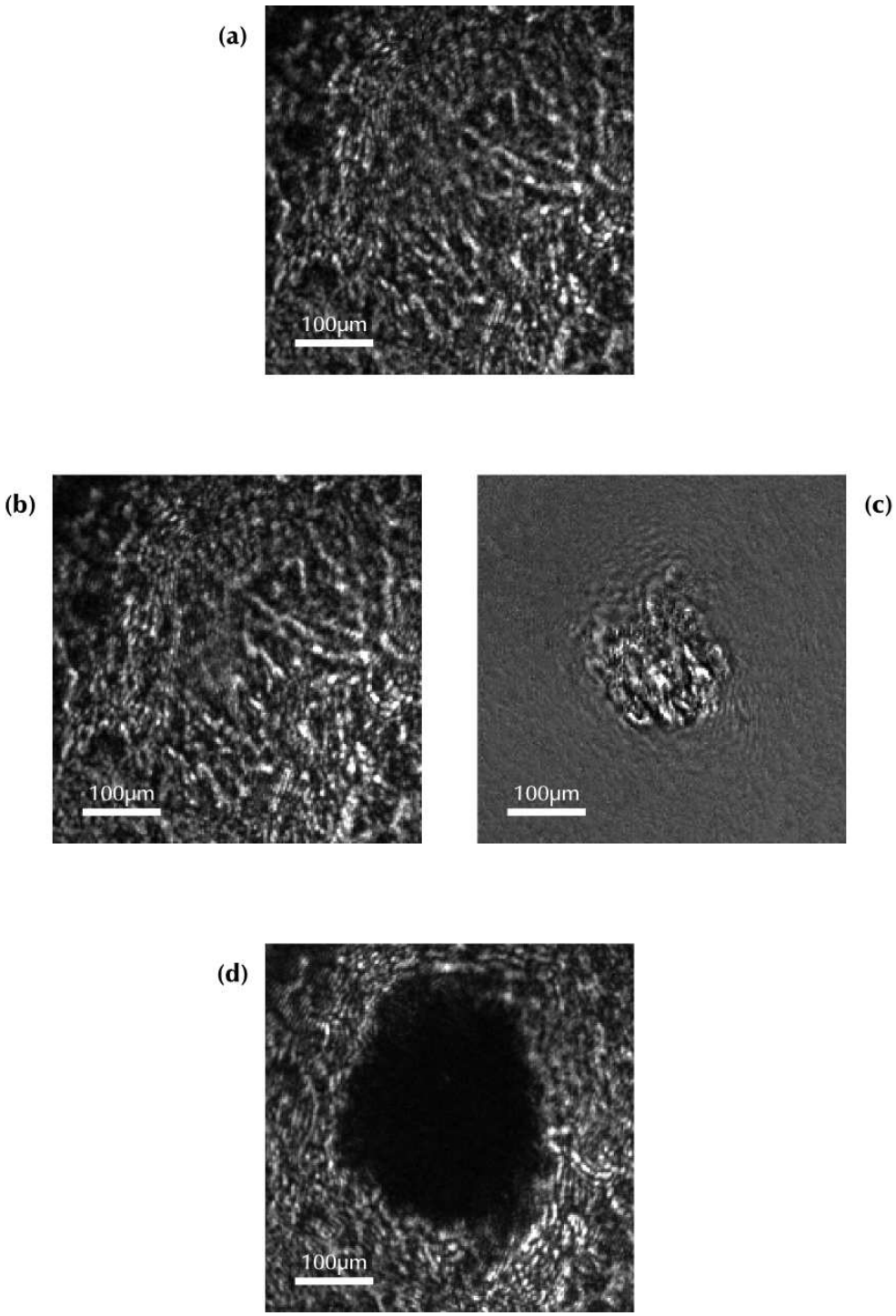


Figure 5.8: Cuts from a set of reflectometry images of a $3\mu m$ target after a delay of $90mm$ ($600ps$) from the *pump* pulse. (a) Reference image. (b) Reflectometry during the *pump* shot; no apparent deformation is visible. (c) Pixel to pixel ratio between (b) and (a): except from the shot area, an almost flat surface at $R \approx 1$. (d) Image of the back surface long time after the shot. 68

The surface of the target has no optical quality, which results in the formation of a homodyne speckle field (Fig.5.8-a,b,d) that is produced by the interference of the – coherent – light source on the structures of the surface that have a size comparable to the wavelength. When the *pump* laser is shot, no clearly visible perturbation is present on a ns timescale, other than a deformation (Fig.5.8-b) in the speckle field, which depends on the delay time. If the pixel-wise ratio

$$\tilde{R} = \frac{I_{shot}(x,y)}{I_{ref}(x,y)} \tag{5.9}$$

between the shot and the reference image is calculated, some deformation structures start to appear, surrounded by the almost[4] constant plane $\tilde{R} = 1$; on purely qualitative basis, we can divide the obtained $\tilde{R}$ maps in three types (Fig.5.9) as delay time increases:

1. **no perturbation:** there is no observable perturbation in the $\tilde{R} = 1$ surface;
2. **speckles deviation:** the shot area shows peaks of relative reflectivity both lower and higher than 1 but integrals show no net energy absorption. The peaks might be originated by the rigid translation of speckles around the shock breakout area;
3. **absorption:** inside the speckles perturbation area appears a clean, almost circular, darker structure.

The boundary between different types of images is found to be dependent on the target thickness: their scaling is depicted in (Fig.5.10).

[4]This neglects intensity fluctuations on the image that are produced by laser instability and that show a low spatial frequency.

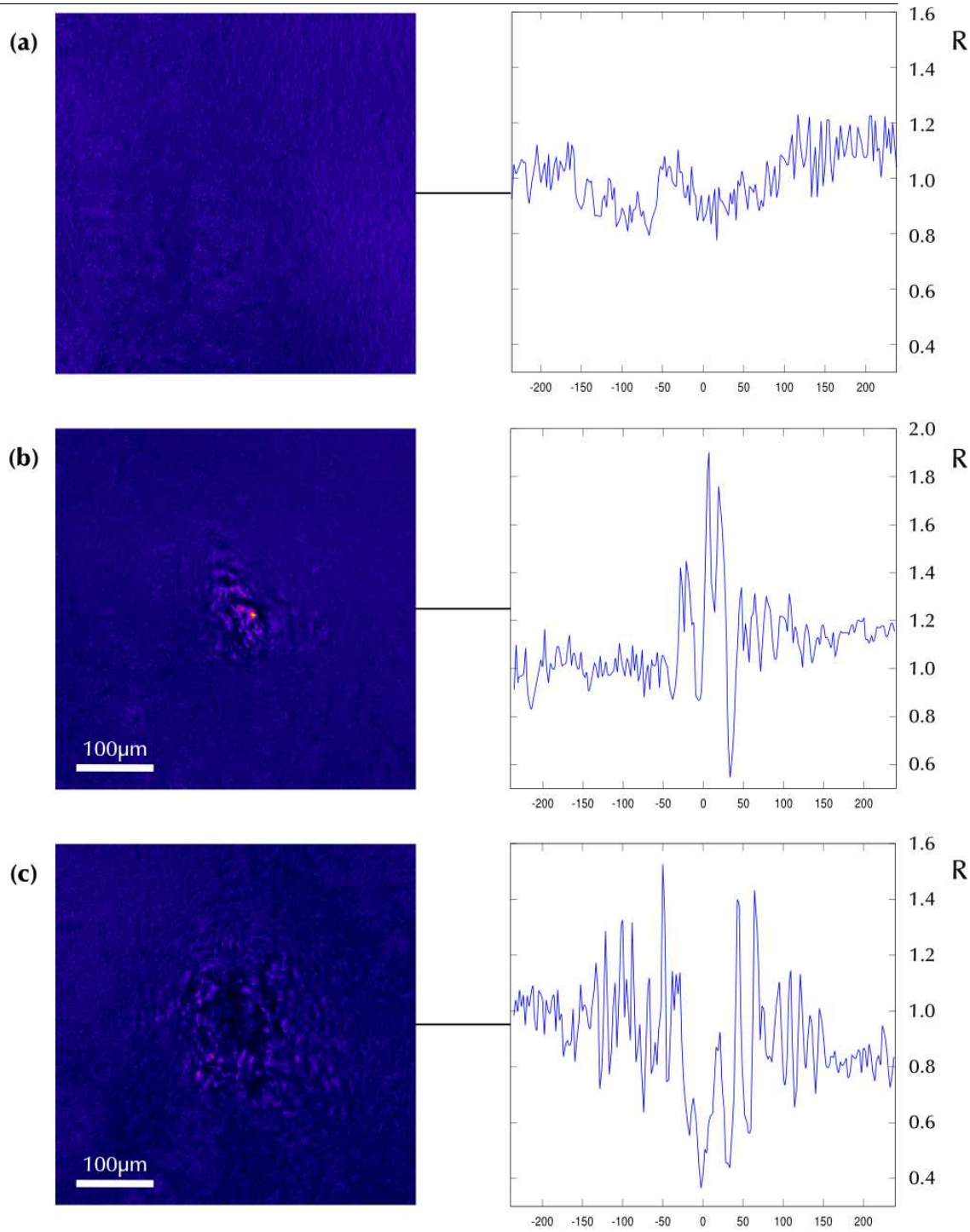


Figure 5.9: $\tilde{R}$ maps (left) and horizontal cuts (right) for three different delays on a $2\mu m$ target; (a) $t = 150ps$ no perturbation is present; (b) $t = 350ps$ speckles deformation results in lighter ($\tilde{R} >> 1$) and darker ($\tilde{R} < 1$) areas, without any net energy absorption; (c) darker areas are clearly visible and a net energy absorption is measurable.

A different behaviour is observed on the $800nm$ target. Here the perturbation appears

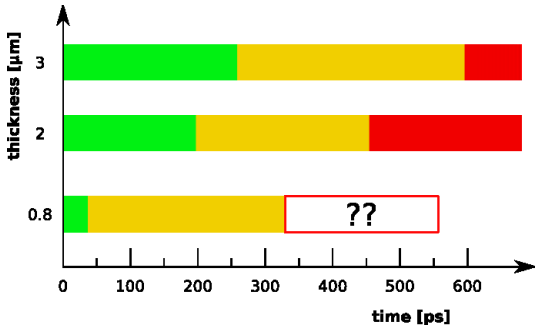


Figure 5.10: Time boundaries between different types of rear surface perturbation for different target thicknesses. Green, Yellow and Red bands represent respectively maps like Fig.5.9-a/b/c. For the $800nm$ case, no clear transition to "red" type was observed in the searched timescale.

within the first $100ps$ as a "deformation-like" image and no transition to the "absorption-like" is observed in the searched timescale. Instead, the perturbed area expands radially without a precisely defined structure.

5.5 Analysis of the Experimental Data

The images are treated numerically. At first the parameters of each shot are measured from the $\tilde{R}$ image; the $shot/reference$ map is filtered in its $2D$ Fourier plane [5]. The purpose of this filter is to eliminate every feature belonging to the target spatial characteristics, its transverse fluctuations and camera electronic noise. The interest of this filtering, while not conserving the experimental information of reflectivity, is to precisely determinate, in a self consistent way for the entire dataset, the geometrical parameters of the shocked area: the position of its center, the diameter of the perturbation (Fig.5.8-*upper*) and the laser reference area. The laser reference area is a square aside of the shocked region where no influence from the *pump* laser is supposed to have happened; its integral in energy, from the untreated images, is used to normalize the total contained energy between the different shots, getting rid of laser fluctuations.
The reflectivity is finally calculated from the ratio between the total energy contained in the shocked region from the two, reference and shot, images; the ratio is renormalized to the ratio of integrals from the two check areas:

[5] I used a 100 pixels FWHM, 10^{th} order bi-dimensional super-gaussian filter.

$$R_{exp} = R_{cold\,Al} \cdot \frac{E_{hole,shot}}{E_{hole,ref}} \cdot \frac{E_{check,ref}}{E_{check,shot}} \tag{5.10}$$

The integration is done via standard trapezoids method. Note that this calculation gives only the difference in reflectivity between the perturbed and the unperturbed case; in order to plot it on an absolute scale, it has to be renormalized to the reflectivity of cold aluminum, $R_{cold\,Al} = 0.98$.

In Fig.5.11 is shown the evolution of the size of the perturbation on the surface versus

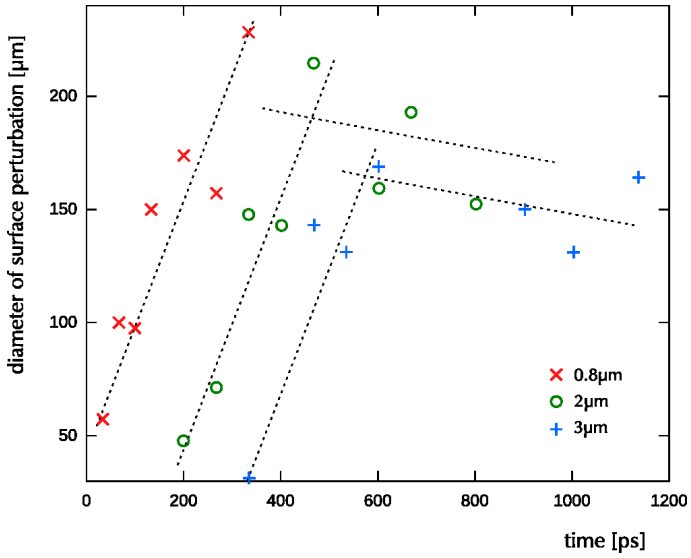


Figure 5.11: Diameter of the perturbation on the rear face of the target measured on the $\tilde{R}(x, y)$ images.

time. The boundaries are measured on the filtered $\tilde{R}$ image (defined by (5.9)). There is a qualitative difference between the target thicknesses. In fact both the thicker targets show a "hole" that grows in diameter until a quasi-static value is reached. The $800nm$ target, on the contrary, doesn't settle, and produces a continuously growing structure until its size reaches the final hole diameter (like the one shown in Fig.5.8-d). No precise absorbing structure (like Fig.5.9-c) is ever produced. For this reason no further data acquisition and analysis is performed on the $800nm$ data after $t = 350ps$ (see 5.6).
For the other two thicknesses the reflectometry results are summarized in Fig.5.12 and Fig.5.13.

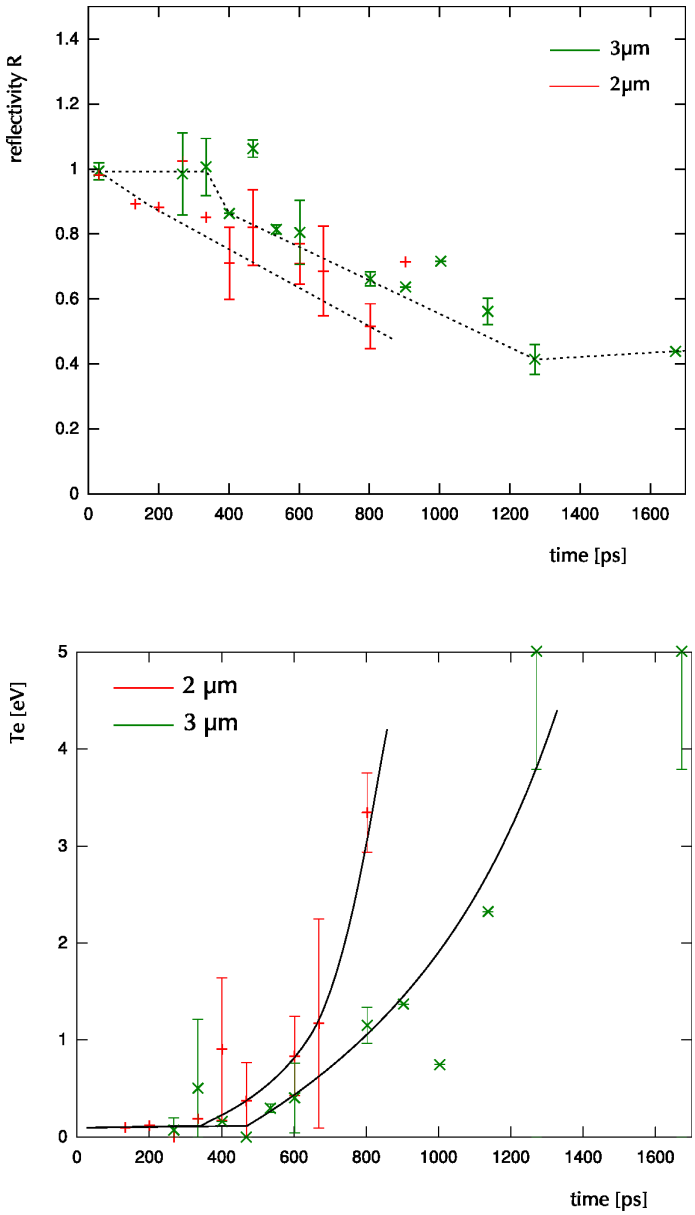


Figure 5.12: *(upper)* The experimental value of R as defined in (5.2) and calculated according to (5.10), for the two thicker targets. *(lower)* Evolution of the electron temperature T_e from the experimental points in the upper plot. The highest point for the $3\mu m$ target are limited in electron temperature by the minimum reflectivity that bulk aluminum in the considered conditions can have ($R = 0.51$ at $T_e = T_i = 5.2eV$).

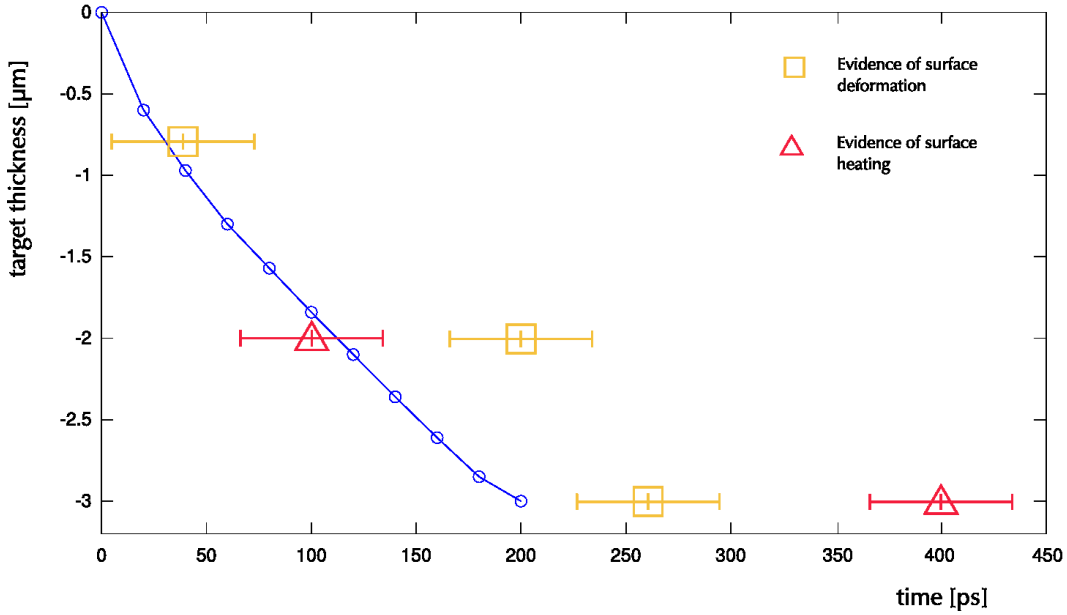


Figure 5.13: Synthesis of the propagation of the shock wave through the metal target. The blue circles represent the propagation of the shock wave in an infinite bulk (extrapolation from the hydrodynamic simulations in 4.4). The yellow points represent the moment where a variation becomes first visible on the $\tilde{R}$ maps. The red points fix the moment when the reflectivity starts falling from the analysis in Fig.5.12-*upper*.

5.6 Discussion

The experimental measurements show an evolution in time which is consistent with the timescale that is obtained from simulations.

The experimental points in Fig.5.13 show a qualitative difference between the three thicknesses. The yellow squares represent the position of the delay line when a structure becomes visible in the $\tilde{R}$ maps, meaning a deformation in the speckle field. The red triangles mark the point where the experimental plots in Fig.5.12 show a fall in reflectivity from the unperturbed value.

The $3\mu m$ targets experience a deformation before a measurable absorption happens. The $2\mu m$ targets show light absorption before a visible deformation of the surface. The moment the absorption starts is consistent with the arrival of the shock wave. The difference between the two behaviours might be due to the different importance of the ion heating. On the $3\mu m$ target the ion heating may happen later than the $2\mu m$, which could explain why on the thicker one, the decrease in reflectivity happens later.

Finally the $800nm$ target: on the point of view of the scale of time, the surface starts to be perturbed in accord with the hydrodynamic simulation. The evolution that follows (the formation of an undefined, expanding structure) can be explained by a consideration. Targets thinner than $1.5\mu m$ are not guaranteed (by the manufacturer) to be light-tight, which means that the production process cannot achieve a real metallic foil, but more probably a cluster of smaller structures. When the structure is stressed it might behave in a different way than a real metallic foil[6].

As for the timescale of the perturbation, the target thickness is traversed by the shock wave at a speed of $3\mu m$ in $200ps$ which motivates, for the forthcoming experiments of proton acceleration, the boundary of

$$d[\mu m] > 15 \cdot \Delta t[ns] \tag{5.11}$$

where d is the thickness of the target and Δt is the distance, in ns, from the beginning of the over-threshold part of the pedestal and the main femtosecond peak. Moreover the information here contained enables us to correlate the gradient scale length that is produced on the illuminated surface and the position of the shock in the bulk (see Fig.4.16 along with Fig.5.13).
As for the characterization of the target surface in presence of the breakout of a shock, the simple reflectometry doesn't allow to obtain sufficient informations. In fact, once the shock has broken out, a second expansion begins. In presence of a density gradient, the simple, single beam, reflectometry measurement cannot distinguish between absorption due to the electron temperature and absorption in the plasma gradient. During our experiment we believe the delay time to be short enough to neglect the formation of a density gradient.
With the aim of studying the effect of laser pedestal in proton acceleration experiments, a precise characterization of the gradients and temperatures should be undertaken. For example, a complete analysis of homodyne speckle fields, like those registered in images (like Fig.5.8), could give a precise mapping of the surface deformation[7] which is reported [57] to be correlated with the angle of emission of the accelerated ions.

[6]This fact seems to be specially true for GoodFellow foils at $800nm$, which shows unpredictable behaviour in the proton acceleration experiment too.

[7]This could be done, for example, by a wavelet analysis on the homodyne speckle field with proper test functions.

Finally, the experimental campaign underlines the importance of a deeper study of the structure of thinner targets and in which ways it could affect the ion acceleration mechanisms.

Chapter 6

Proton acceleration: experimental setup

The *Salle Jaune* experimental area at the *Laboratoire d'Optique Appliquée* contains a multi-terawatt, CPA based, laser chain and the experimental installation that is needed for ultra-high intensity experiments. This chapter is dedicated to a deeper insight on the setup that we realized for the acceleration and characterization of ion beams. The focusing quality of the laser beam influences the cutoff energies and the dynamics of the accelerated beam, which requires a careful alignment of the focusing optics (a parabola at $f/3$) and a precise control of the original laser beam. The large numerical aperture sets very small boundaries on the positioning of the target, whereas the main proton diagnostic (Thomson Parabola and Micro-Channel Plate) requires the tilt of the target to be lower than $1°$. The structure of the laser chain and the optical part of our experimental installation is here presented, from the focusing of the beam to the alignment of the target. A second part is dedicated to the ion diagnostics that have been put in place. The experimental results and their interpretation are presented in Ch.7.

6.1 The laser source

The *Salle Jaune* laser is a Titanium-Sapphire (Ti:Sa) solid state laser and belongs to the category of T^3 lasers (Table Top Terawatt). It is a multi-stage CPA chain composed by a pre-amplified front-end and three multipass amplifiers, capable of delivering up to $2J$ per pulse (before compression) at a repetition rate of $10Hz$. More in detail (see scheme in Fig.6.1):

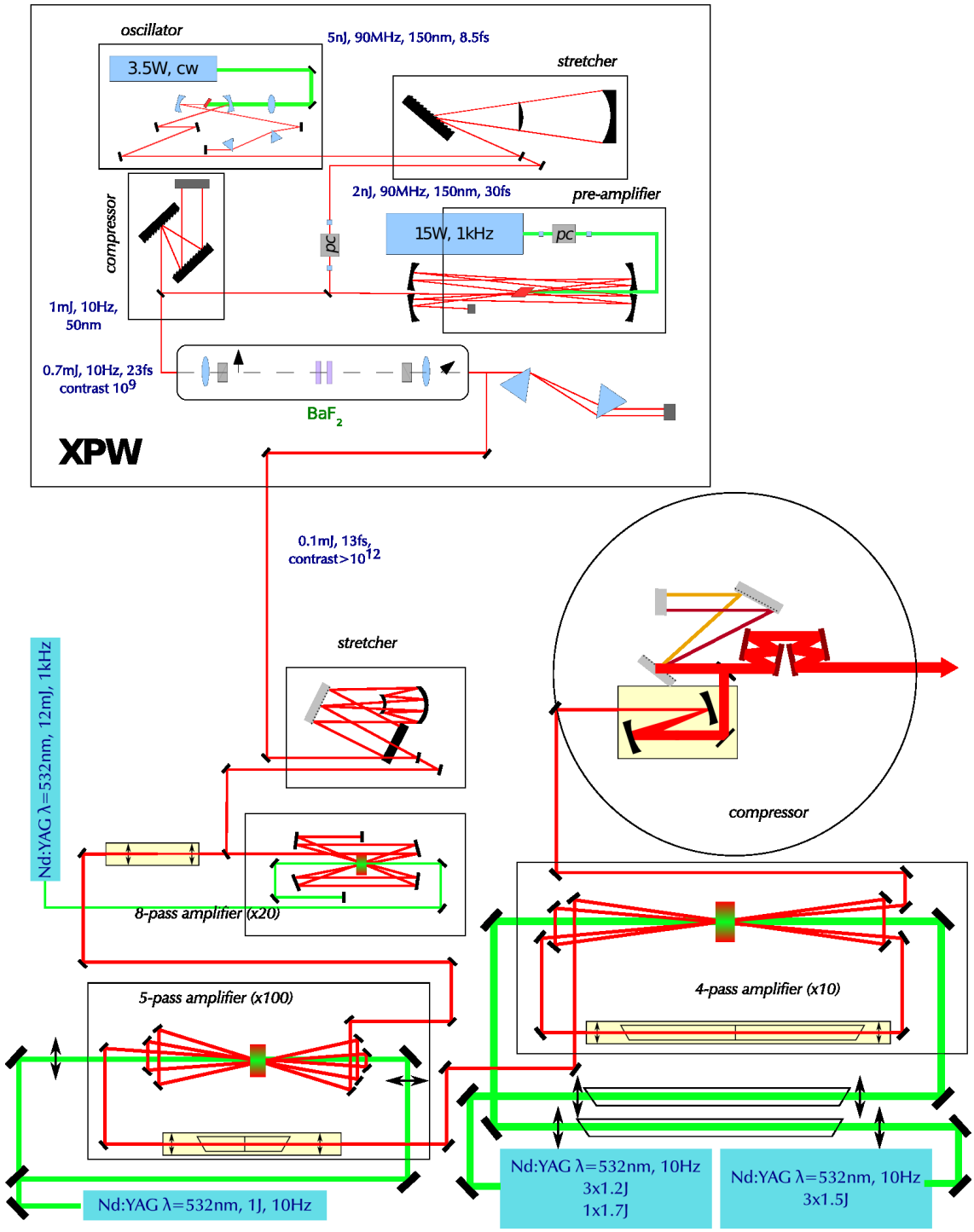


Figure 6.1: Block scheme of the *Salle Jaune* laser system.

Oscillator: a Ti:Sapphire, Kerr-lens mode-locked, oscillator produces a train of $8.5fs$ pulses, with a per-pulse energy of $5nJ$ at a repetition rate of $88MHz$. The central wavelength is $\lambda = 810nm$ and the spectrum is $150nm$ FWHM[1].

Preamplification and XPW: The repetition frequency from the oscillator is cut down to $10Hz$ by Pockels cells. The selected pulse is stretched, pre-amplified to $1mJ$ and compressed back to $23fs$, in order to be injected in the XPW system (see 6.1.1). The preamplifier is charged by a diode-pumped CW laser, which noticeably improves the stability.

Multipass amplification: the pulse is stretched to $600ps$ and injected in a three stages (4-pass, 5-pass and 3-pass) chain of Ti:Sa amplifiers pumped by doubled Nd:YAG lasers. The beam undergoes spatial filtering after each amplifier. The complete amplification process brings $100nJ$ (after XPW) to $\approx 2J$. The contrast worsen from 10^{12} to $10^9 \div 10^{10}$.

Separation of the beams: Before the compression, a partially reflecting mirror (in our experiment was 10%) is used to create a second beam (*probe*) with lower energy. A $\lambda/2$ filter and a polarizer cube are used to introduce a variable loss. Finally, a motorized delay line is provided to change the delay between the two beams.

Compression: The two beams of $400ps$ pulses are compressed by two separate grating compressors to a duration of approximately $30fs$ with an efficiency that ranges between 45% and $\approx 55\%$.

Phase front cleaning: the wave front of the *pump* beam is corrected by a cylindrical symmetry deformable mirror (see 6.2.1).

6.1.1 Enhancement of the Contrast

The contrast ratio (Fig.6.2) of an UHI pulse is a parameter of great importance when speaking of interaction with matter (Ch.3, 3.4). Many features, many of them not completely exploited, of the interaction process are correlated with the total energy and the over-threshold duration of the pedestal that precedes the main peak. From a CPA chain, three types of effects are in general observed.

[1]The effective spectrum width is lowered as the pulse undergoes the following amplifications. This is due to the non-linear gain in the crystals and to the non-constant gain envelope for different frequency components, which makes central wavelengths to be more amplified than peripheral ones.

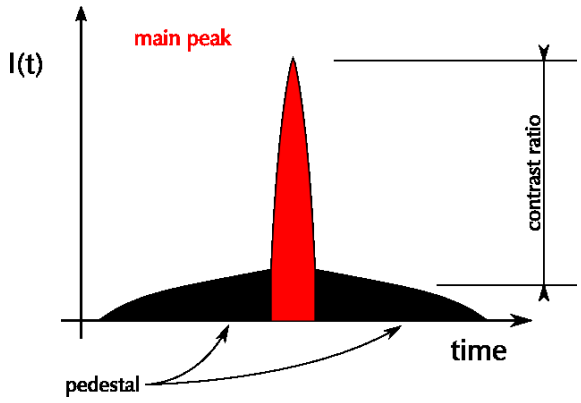


Figure 6.2: The contrast of a short pulse.

Prepulses Replica of the *fs* pulse can be produced, by various reasons, before and after the main pulse. Examples are *(i)* insufficient extinction power of the Pockels cell that selects the pulse from the oscillator, *(ii)* the presence of shortcuts in the optical path or *iii* cuts in the pulse spectrum.

Background light In the oscillator cavity, the production of *fs* pulses (with a repetition rate of $88MHz$ and a per-pulse energy of some nJ) is a process which is in competition with the continuous wave (CW) production, which results in a continuous background around the *fs* pulses. The contrast in the oscillator pulse train can however be as high as 10^9.

Amplified Spontaneous Emission The ASE comes from the spontaneous emission in charged crystals, which is produced before the passage of the main pulse. The ASE is amplified in the forthcoming crystals, worsening the contrast. The importance of the spontaneous emission is directly bound to the gain in the amplifiers and to the timing between the pump laser pulses (used to charge the mediums) and the seed laser pulse (to be amplified).

The path of the pulse in the optical system controlled by optical shutters (Pockels cells). Their synchrony to the pulse sets the mark on the prepulse structure, cutting the sum of the three effects to a well defined light front. In *Salle Jaune*, the Pockels cells cut the pedestal between $2.5ns$ and $3ns$ before the *fs* pulse. In the original chain, before any active contrast enhancement technique was adopted, the peak to pedestal ratio was, $I_{max}/I_{ASE} = 10^7$ from $3ns$ before, and $I_{max}/I_{pre-p} = 10^5$ for prepulses $100ps$ before (Fig.6.3-*(upper)*,[96]).

XPW

The use of **XPW** (acronym for *Crossed Polarized Wave generation*) to improve the contrast in a laser chain has been introduced at the *Laboratoire d'Optique Appliquée* [45, 47, 48] after previous studies [69, 70, 46] on the $\chi^{(3)}$ anisotropy of BaF_2 glasses. The generation of a crossed-polarized wave is a degenerate, $\omega \rightarrow \omega$, four wave mixing process, where a rotation of the polarization is produced between the input and the output wave. From [47] the equations for the non-linear propagation are written as

$$\begin{aligned} \frac{\mathrm{d}A}{\mathrm{d}z} &= \mathrm{i}\gamma_1|A|^2A - \mathrm{i}\gamma_2\left(|B|^2B - A^2B^* - 2|A|^2B\right) + \mathrm{i}\gamma_3\left(2|B|^2A + B^2A^*\right) \\ \frac{\mathrm{d}B}{\mathrm{d}z} &= \mathrm{i}\gamma_1|B|^2B - \mathrm{i}\gamma_2\left(|A|^2A - B^2A^* - 2B^2A\right) + \mathrm{i}\gamma_3\left(2|A|^2B + A^2B^*\right), \end{aligned} \tag{6.1}$$

where $A(z)$ ($A(0) = A_0$) is the input wave amplitude and $B(z)$ ($B(0) = 0$) is the cross-polarized wave; the factor $\gamma_{\{1,2,3\}}$ depends on the non-linear tensor of the material and the polarization angle.

The enhancement of contrast relies on the fact that the III-order non-linear process holds a 3^{rd} order dependency of the output field on the input field. This produces a rotation of the polarization which depends on the 3^{rd} power of the incoming intensity. The effect is optimized by matching the thickness of the BaF_2 crystals with the input amplitude A_0 from (6.1); two polarizers in the final setup are used to *(i)* set the input polarization, *(ii)* select the output. In [5] a contrast of 10^{12} is reported, from 3ω autocorrelation measurements on the *Salle Jaune* front-end.

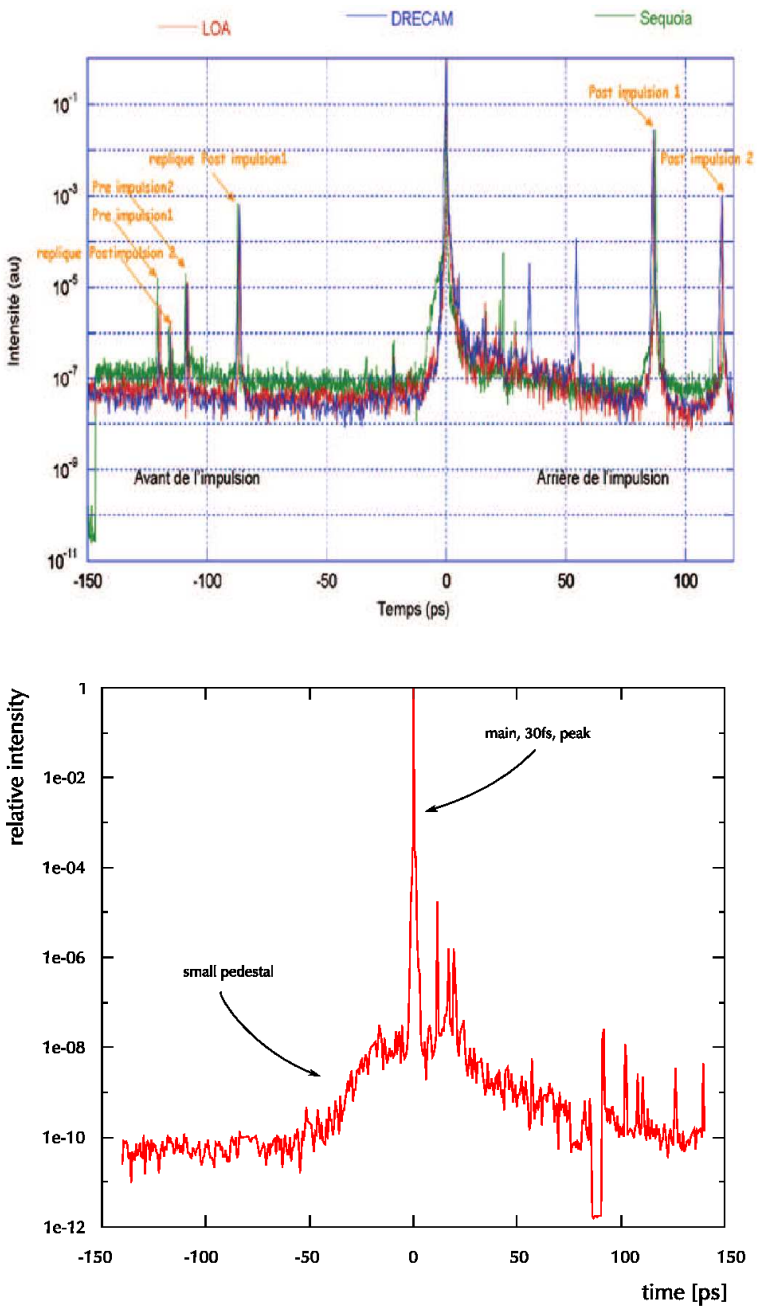


Figure 6.3: *(upper)* Contrast on the previous (up to year 2006) configuration of the *Salle Jaune* laser (excerpt from [96]); *(lower)* 3ω measure of present contrast, with a two crystals XPW system.

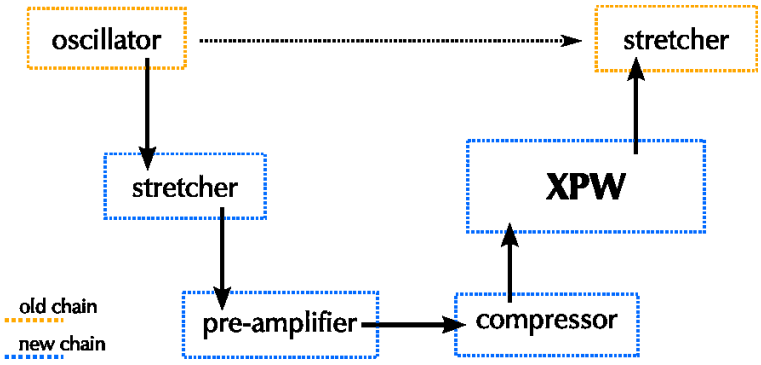


Figure 6.4: XPW system insertion on the laser chain (left), between the oscillator and the 8-pass amplifier, and picture of the setup (right)

The theoretical efficiency in terms of contrast enhancement is limited by the extinction power of the two polarizers (the polarizer before and the analyzer after) that are used to set the input polarization and select the cross-polarized output. The low generation efficiency (12% and 25% respectively for single or double crystal arrangement) and the necessity to work on the compressed pulse made necessary to pre-amplify the pulse (and compress it back) before entering the system (Fig.6.4).

Other systems Different solutions have been proposed to increase the contrast ratio in CPA chains; at present the most common and effectively used among the community of laser ion acceleration are fast Pockels cells and plasma mirrors. The firsts are Pockels cells with an improved high voltage power supply, with reduced rise and fall times, thus able to open and close the optical circuit in a faster way. They are used to directly cut the pedestal to a shorter duration before the *fs* peak. In CPA systems they are best used in the initial part of the chain, where higher gain produces faster contrast worsening and the laser intensity is lower, hence limiting the energy loss in the Pockels crystal. Typical response values are $300ps$ rise time and $150ps$ jitter.

Plasma mirrors use the pedestal energy to produce a plasma on a transparent slab of glass that in turns reflects the laser beam[17, 50, 37, 7]. The beam is focused to a level where the pedestal itself has sufficient energy to produce a supercritical, solid density, plasma. The peak intensity due to pedestal on the mirror have to be accurately calculated to avoid expansion of the plasma (early ionization) or transmission of a part of the main peak (late ionization). In the ideal case, the pedestal is transmitted or absorbed, while the peak is reflected: double plasma mirrors have been shown able to

cut the pedestal to a contrast better than 10^{10}. Recent results [55] reported a total efficiency for the double mirror setup of $\approx 50\%$. Another drawback is that mirrors are damaged in the process and they have to be moved after after each shot.

It has to be underlined that the pulse, once cleaned by a plasma mirror, is qualitatively different from what is obtained by XPW; this fact will be taken in account when comparing our data to proton spectra from literature.

6.1.2 Adaptive correction of the phase front

The extent the beam can be focus to, meaning the ability to concentrate the biggest part of energy into a spot as small as possible, depends on the quality of the beam's transverse profile. On a beam from a CPA is often present a certain level of distortion, due to the number of refractive optics on its path and the non perfectly uniform effect of crystals, including thermal lensing effects and non completely isotropic pumping.

On the *Salle Jaune* laser system, a deformable mirror is used to partially correct the

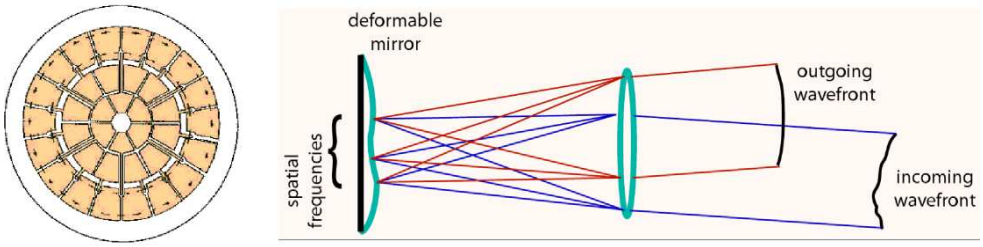


Figure 6.5: Deformable mirror: the mirror surface is on the focal plane of a lens, where the spatial frequencies of the phase surface are mapped.

beam wave front, so the quality of the focused spot. It is composed by 52 bi-morph actuators in cylindrical symmetry, which can correct up to the 6^{th} order of aberration in Zernike polynomials. The correction procedure is accomplished in two steps.

In the first step a self-learning loop builds the matrix of correlation between the movement of actuators and the projection of the phase surface – after the mirror– on the space of Zernike polynomials[2]. The correction matrix depends on the beam characteristics, so that the procedure have to be repeated for every important realignment of the laser system. In the second step a genetic algorithm finds the best actuators' configuration.

[2]The phase surface is measured by a 16×16 Shack-Hartmann analyzer.

The plane on the beam path that is conjugated to the Shack-Hartmann (SH) and the deformable mirror is situated right after the beam compressor. There are some $10m$ of free propagation between this plane and the point where beam is focused on the target. This fact limits the efficacy of the active correction by the DM and does not consider any of the forthcoming optics.

6.2 The experimental installation

The experimental setup provides *(i)* the optics to transport and focus the big, high power, beam, *(ii)* the optical diagnostics for the positioning of the target and *(iii)* the devices related to the ion beam. In Fig.6.6 the general scheme of the installation is presented.

1. Pump beam
2. Probe beam
3. Parabola
4. Target Holder
5. Microscopy of the focal spot (removable)
6. High magnification reference of target focus
7. Motorized delay line
8. (**a-c**) Thomson parabola and MCP
9. Transparency microscopy of the target (removable)
10. Lead screen and motorized image plate

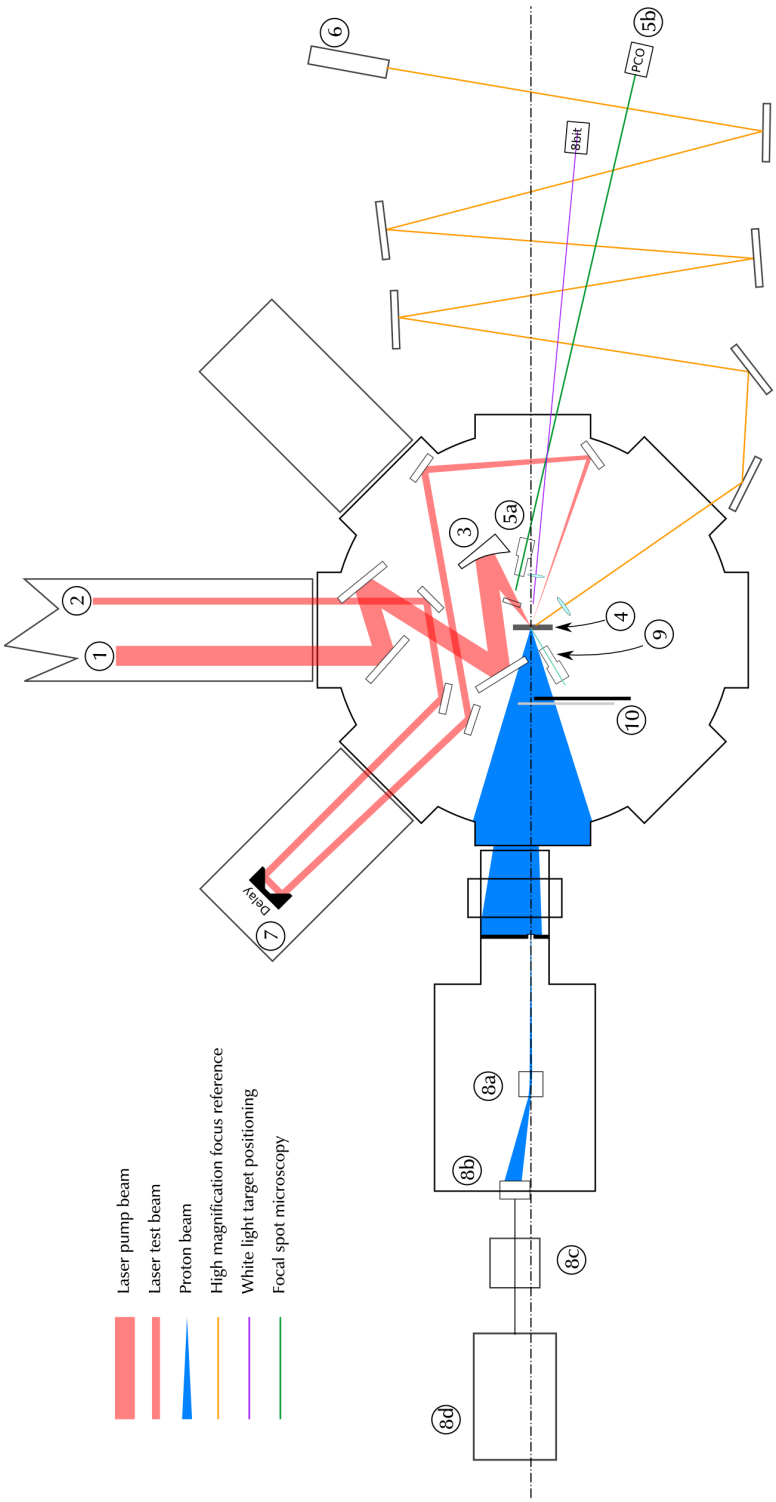


Figure 6.6: Scheme of the setup for laser-ion acceleration.

6.2.1 Laser Diagnostics

Energy

The laser in its present conditions produces $1.5J$ to $2J$ per pulse before compression. The optics chain from the source to the experimental installation transports a total of 37% (measured) in energy. The efficiency of the compressor alone accounts for $\approx 45\%$ of losses, which leaves $\approx 3\%$ loss for each mirror. At the end of the experiment the total transport coefficient decreased to 30%, probably due to aluminum deposition on the mirrors.

Focusing

The main beam is focused by a glass parabolic reflector; the parabola is a 30° off-axis cut, with a numerical aperture of $f/3$ and a focal length of $15cm$. The glass surface is gold coated to optimize the reflectivity. In the case of an ideal gaussian beam, the pump would be focused down to a waist of $w_0 = 1.4\mu m$.
To image the focal spot, the focused beam is intercepted by a removable mirror and sent through a microscope objective to a linearized camera (Fig.6.6-5). The quality of the spot is defined by measuring its transverse size and the ratio of energy contained in its $1/e^2$ contour (Fig.6.7).

Monitor of Laser Parameters

In a laser system of this size it is common to observe fluctuations in the functional parameters. A precise control of shot to shot behaviour is even more important in experiments where a single measurement cannot be repeated a number of times sufficiently high to authorize a statistical treatment. Nevertheless a strong correlation between the different parameters (energy, direction of the beam, contrast, etc.) is observed; this enables us to limit our observation of the laser status to some key parameters and be able to set a rejection criterion out of them.

During the experimental procedures, two diagnostics constantly keep the laser status under control: the pulse integrated energy and the contrast ratio.
The energy is integrated by a linearized camera: the small leak ($< 0.01\%$ of energy) from a dielectric mirror is enough to record the transverse profile of the beam and to

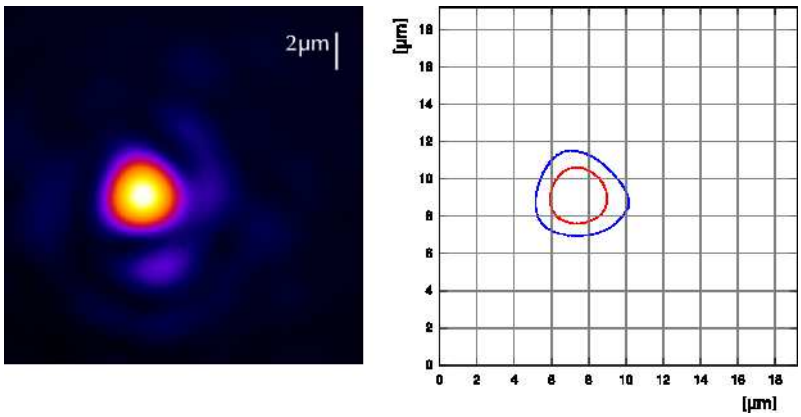


Figure 6.7: Laser focal spot at $800nm$; (a) image of the spot as seen by camera (resolution: $0.040\mu m/pix$, magnification: $230\times$); (b) contour plots of two different levels of intensity; in red the FWHM contour (diameters: vertical $2.92\mu m$, horizontal $3\mu m$); blue is $1/e^2$ (diameters: vertical $4.4\mu m$, horizontal $5\mu m$) which corresponds to an average waist of $2.35\mu m$. In the depicted case, a total of 72% of the energy is contained in the πw_0^2 surface.

observe the variation in energy. Two effects have been noticed in time: *(i)* a strong shot to shot and *(ii)* a slow drift on the average energy (Fig.6.8).

To measure the contrast of the pulse, an aluminum-coated glass blade is used to inter-

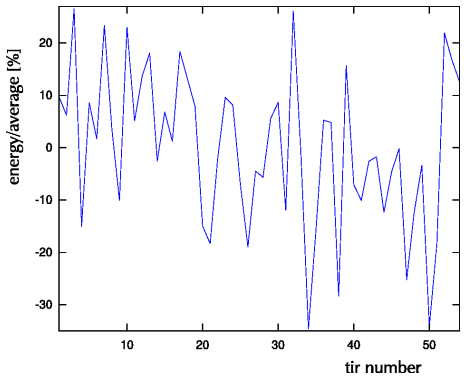


Figure 6.8: Typical shot-to-shot behaviour of integrated laser energy during 54 shots in a row; the peak-to-valley is as large as 60%.

cept a tiny part (smaller than $5mm^2$) of the main beam. The reflection is sent to a fast photocathode (rise time $< 500ps$) that is controlled by a fast oscilloscope. A number of neutral optical densities, enough to observe the peak of the femtosecond pulse, is

added. Once the reference is taken, all of the densities are removed and the pedestal observed. The contrast is calculated from the ratio between the peak and the pedestal, taking in account the number of densities and the integration factor of the photocathode ($500ps/30fs = 1.6 \times 10^4$). The insertion of the blade did not produce any measurable worsening of the focal spot.

Target Positioning

The Rayleigh range of a gaussian beam with a waist of $2.3\mu m$ is $z_0 = \pi w_0^2/\lambda = 20\mu m$ which sets the scale of precision that is needed to align the target. Moreover, a precise absolute reference is important to ensure repeatability and meaningful comparison among different shots. The technique I find to work best is the collection of a part of the light that, from an Helium-Neon laser collinear to the main IR beam, is diffused by the rough target surface. A small lens images the helium-neon spot to a camera (Fig.6.6-6): the lens is aligned to provide a very big magnification ($\approx \times 50$), that is enough to map a range of $50\mu m$ of movement in target focus to the entire chip of an 8bit CCD camera. A small aperture lens is found to work better, for its small level of detail produces a cleaner spot, which eases the reference. I estimate the error on target positioning to be smaller than $15\mu m$.

6.2.2 Proton Diagnostics

Besides of the widely used CR39 or RCF plastics for ion dose integration, new systems are earning importance in the community of laser-ion accelerators, following the need of diagnostics that would produce experimental information in real time, or short time after. This possibility dramatically increases the efficiency of proton acceleration experiments, where some parameters need a direct feedback from the produced beam (the best example being the search of the correct focus position).

New technologies include image plates, scintillating materials and micro-channel plates. During this experiment, the main interest has been focused on the MCP plates, for their sensitivity, the resolution and the real-time availability of the experimental information. Image plates have been used to record the propagation direction of the beam as well as its divergence (see Fig.6.9).

CR39

The CR39 (California Resin-39[3]) is a plastic that is widely used as an ion dose integrator. Its chemical properties are modified by the energy deposition by massive particles traversing its bulk. The used reaction is the increased solubility of molecular fragments in a strongly basic environment[4]. The trajectory of a single particle continuously deposits energy while passing through the solid and no apparent damage is produced. When the surface is etched by a *base*, the volume that experienced radiation damage is corroded faster and holes are produced. Precise calibrations exists to correlate energies and species to the time evolution and the geometrical properties of the produced holes[85]. A simpler approach for spectral characterization of ion beam is obtained by superposing foils of increasing thickness on the detecting slab, to set lower cutoffs on measurable energies. The stopping power of filters can be calculated very precisely, letting to correlate the presence of radiation damage to a well defined energy range.

At the time of writing, no laser effect on CR39 is documented in the literature. I observed a threshold of about $10^{14} W/cm^2$ at $\lambda = 800nm$ to produce on the detector a type of impact absolutely similar to the signal produced by ions. No ablation is produced, and latent tracks appears only upon etching. To avoid the phenomenon it is necessary to protect the dose integrator from intense IR light. During the experiment, at least one non transparent (metallic) filter is put on the foil.

Image Plate

An alternative way for measuring the ion beam profile or the ion spectra is the use of Image Plates. Here a thick plastic foil is covered by a material that is characterized by very long lived molecular meta-levels. The transition from the ground state to a charged state is triggered by the deposition of energy by any kind of ionizing radiation. The material relaxation can happen spontaneously or be stimulated by electromagnetic wave with the proper wavelength, and results in the emission of photons. In a special scanner, the micrometric laser spot from a diode is used to stimulate this emission. The produced signal is read by a photomultiplier tube and digitized, to produce an image. The image resolution is theoretically limited only by the waist of the scanning laser beam which is, for our scanner, $25\mu m$. Some images we realized by exposing the plate

[3] namely *Polyallyl-diglycol-carbonate*, $C_{12}H_{18}O_7$.

[4] The reaction is usually accelerated by heating the bath; the most commonly used bases are the strongest ones, $NaOH$ and KOH. For a deeper insight in the etching process, see [85].

to a radioactive source (^{241}Am, $19kBq$) showed a bigger size for single impact (at least three times) which suggest a worse limit on the spatial resolution.
The foils are erased when exposed to incoherent white light for a certain time ($\approx 10-15$ minutes); they can be re-used afterwards.

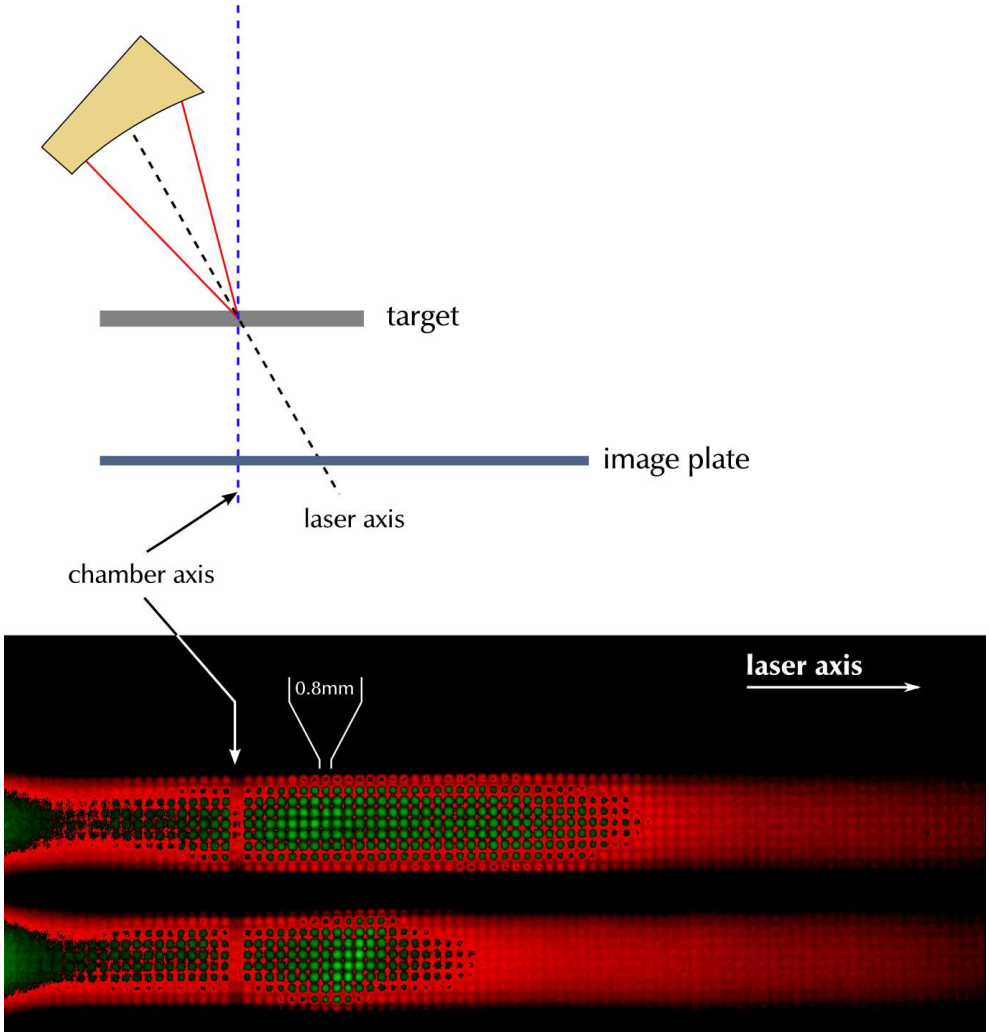


Figure 6.9: Example of use of an image plate to monitor the proton beam direction. The image, in fake colors, shows two shots where the proton axis is moving away from the main axis of the chamber, where the MCP is aligned. A filter of constant thickness composed by $200\mu m$ Mylar and $36\mu m$ Aluminum (total stopping power: $4.8MeV$) is used to cut lower energies, a steel grid of $0.8mm$ spacing to record the scale and a $200\mu m$ thick Aluminum wire is aligned on the MCP proton axis. The distance between the target and the IP is $12cm$; the figure shows the beam whose center travels at 3.5° from the MCP direction. The half-divergence for the over-threshold beams in the tracks is $\sim 7°$.

The resolution, the size of the active area (standard plates are sold in foil of $20\times25cm$) and the ease of digitizing the integrated dose make this kind of detector very useful. The main problem is that they are sensitive to every kind of ionizing radiation of sufficient energy, which limits the possibility of using them in environments were e^- and γs are also present. To be able to discriminate between electrons and ions, I use a dual thickness filter, where a thicker one filters out all of the ion signal and the thinner sets a meaningful cutoff for the searched proton energies. The proton signal is obtained by direct subtraction between the two areas, from the assumption that the thicker filter ($\approx 500\mu m$ Mylar) would very slightly affect the signal from electrons and γs.

In our experiment we used IPs to image the propagation direction and the divergence of the generated proton beam, to ensure the proper alignment of other diagnostics (see later). For this purpose, the IP is positioned normal to the main axis of the chamber and covering with its active surface the space from the target normal to the prolongation of the laser axis (see Fig.6.6-10). The IP can be moved in the vertical direction. Two lead plates limit the exposed area to an horizontal stripe of $\sim 0.7cm$, which makes possible to use the same plate for several laser shots (Fig.6.9).

MCP and Thomson parabola

The main diagnostic system for real time detection of the products of the interaction is a Micro Channel Plate (MCP, Fig.6.6-b) coupled to a Thomson parabola (TP, Fig.6.6-a). A Thomson parabola is a device where an electric and a magnetic field are superposed, one parallel to the other; when a charged particle propagates through the region, two separate motions are set in place, due to the independent action of the two fields, and the particle is deviated according to its mass and charge. The Micro Channel Plate (MCP) (Fig.6.10) can be seen as an array of very high gain amplifiers. A strong electric signal is produced whenever a particle deposits energy on the surface. In the two following sections I analyze the theory of propagation in the TP and the experimental realization of the MCP+TP based detector for the ion acceleration experiment.

Theory The equations of propagation at non-relativistic energies for the generic ion of mass m and charge q in E, B fields like those defined in Fig.6.11 is

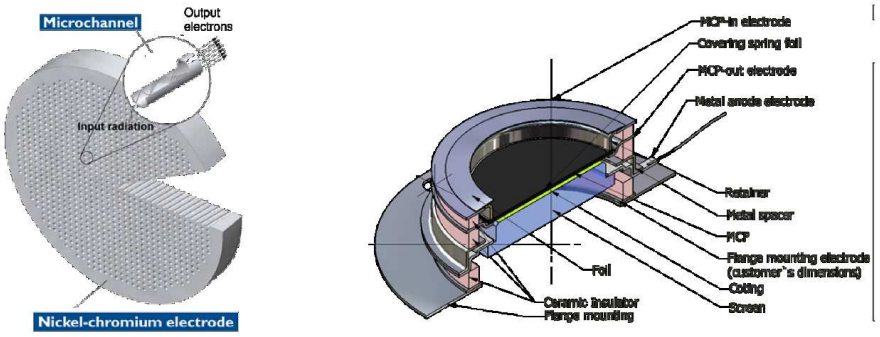


Figure 6.10: Graphical representation of the MC plate (left) and of its assembly (right).

$$\begin{cases} x(t) &= \dfrac{1}{2}\dfrac{qE}{m}t^2 \\ y(t) &= R\left[1-\cos\left(\omega_c t\right)\right] \\ z(t) &= R\sin\left(\omega_c t\right) \end{cases} \tag{6.2}$$

where $\omega_c = qB/m$ is the common cyclotron frequency and $R = v_0/\omega_c$. Following the depicted geometry, the particle is supposed to have $v_0 = v_{0,z}$. The magnetic term in the Lorentz force $\underline{v} \times \underline{B}$ is perpendicular to $\underline{E}$, so the two motions, electric and magnetic, are independent one to the other. The only interaction between the two motions happens due to the finite size of the field region; the interaction with the electric field produces an acceleration of the particle, making a term in v_x to appear. The final value of v_x depends also on the time needed to the particle to exit the area of influence, which is longer than what it would be observed without a B field, for the circular trajectory in the $z-y$ plane. In the simplified case of $L_B = L_E$ (the lengths of the field regions on the $z-$axis), according to (6.2)$-2,3$ the time needed to reach the end of the TP is

$$t_B = \frac{1}{\omega_c}\arcsin\left(\frac{L_B}{R}\right) \tag{6.3}$$

from which on the plane $(x, y, z = L_B) = (x_S, y_S)$ it holds

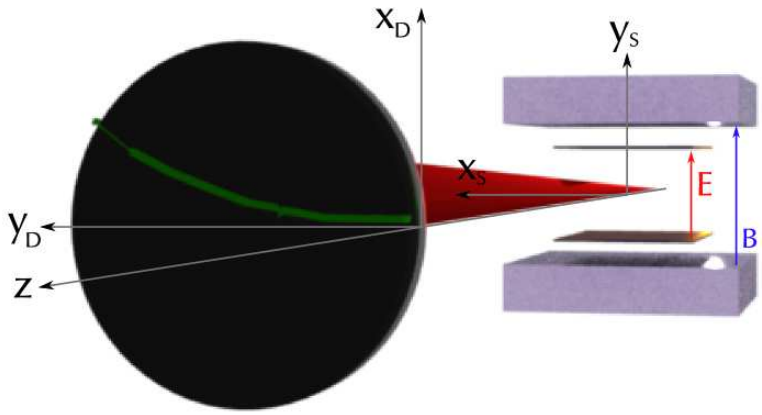


Figure 6.11: Graphical representation of the realized device (Thomson parabola and MCP).

$$\begin{cases} x_S &= \dfrac{1}{2}\dfrac{qE}{m\omega_c^2}\arccos\left(1-\dfrac{L_B}{R}\right)^2 \\ \\ y_S &= R\cdot\left[1-\left(1-\dfrac{L_B^2}{R^2}\right)^{1/2}\right]. \end{cases}$$

The exit angles are calculated through $\theta_x = \arctan\left(v_x/v_z\right)$ on the x projection and from simple geometrical considerations for the y projection. It gives

$$\begin{cases} \theta_x &= \arctan\left[\left(\dfrac{qE}{m}t_B\right)\cdot\left(R\omega_c\sin\left(\omega_c t_B\right)\right)^{-1}\right] \\ \\ \theta_y &= \arcsin\left(\dfrac{L_B}{R}\right). \end{cases}$$

The coordinates on the detector plane $(x_D, y_D) = (x, y, z = L_D)$, where L_D is the distance from the detector plane and the TP entry point $(0, 0)$, are calculated through

$$\begin{cases} x_D &= x_S + (L_D - L_B)\tan(\theta_x) \\ \\ y_D &= y_S + (L_D - L_B)\tan(\theta_y) \\ &= y_S + \frac{L_B/R}{\left(1-L_B^2/R^2\right)^{1/2}} \ . \end{cases} \tag{6.4}$$

Experiment The detector is an array of a *(i)* micro channel plate (MCP, Fig.6.6-b-upper), *(ii)* a phosphor screen (Fig.6.6-b-lower) and *(iii)* a camera (Fig.6.6-d).
The MCP plate is a matrix of hollow glass capillaries ($\phi = 8\mu m$) whose internal walls are coated with a material with a very low work potential. Two electrodes are placed on the entrance and the exit surface of the matrix, to maintain an electrostatic field at a small angle[5] from the channel direction. When an electron set free from the electrode at the entrance, it drifts through the channel; secondary electrons are produced and made drifting upon collisions on the channel walls. The resulting charge distribution at the exit surface keeps in the amount of extracted charge, the relative distribution of energy that was deposited at the entrance. The emerging electron cloud is made drifting by the second electric field, until it impacts on the phosphor screen. In this way, an image on the phosphor screen reproduces the dose distribution that impacted on the plate. From this point of view, the MCP can be regarded as an imaging device, as the spatial information is not discarded in the amplification process.

Our setup uses a stack of two coupled channel plates (Chevron) to enhance the amplification factor. Typical high-voltage values are $-1.2kV$ on the MCP and $+4kV$ on the phosphor (see Fig.6.13 for schematics). To be able to raise the MCP to $1.2kV$ is necessary to isolate the vacuum gauge from the volume were the channel plate sits, as the weak ion signal produced by the cold cathode is strong enough to generate a high rate of random counts. In the MCP chamber a metallic grid, set to fixed potential of $30V$ to the chamber earth, is used for this purpose. Even if a maximum of $2kV$ is allowed ($1kV$ per plate), voltages higher than $1.3kV$ enormously increase the dark current signal, producing a strong fluorescence on the phosphor.
The final setup is mounted in a separate volume which is connected to the main interaction chamber by a $200\mu m$ pinhole[6]. This is set to fix the resolution of the spectrometer and to produce a differential vacuum between the two volumes; the MCP has to sit in

[5] This is a structural parameter of the MCP. Typical values range from 5° to 12°.

[6] The pinhole is realized on a $2mm$ thick lead plate which is screwed on a $\phi = 1mm$ aperture on the vacuum flange behind the vacuum gate (Fig.6.13). The coupling between the plate and the flange is vacuum tight, for a circular blade on the flange surface enters the lead bulk.

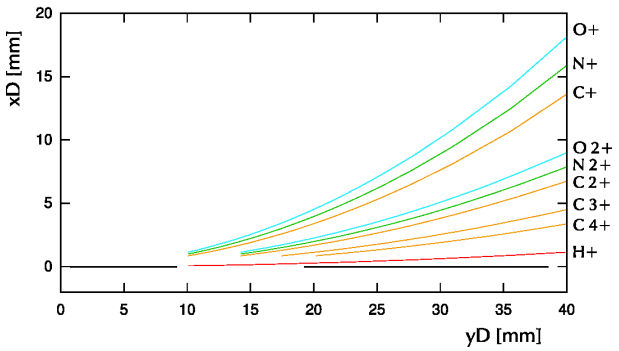


Figure 6.12: Distribution of protons and different ionization degrees for atoms of carbon, oxygen and nitrogen on the MCP plane (Numerical simulation. Magnetic field is experimentally mapped, Fig.6.14. Electric field is set to $E = 2.5{\times}10^5\ V/m$ for $L_E = 4cm$).

a vacuum better than $10^{-5}mbar$ when high voltage is applied.

The pinhole is situated at a distance of $80cm$ from the interaction point. This parameter is very important, as it sets the divergence of the analysed beam and the maximum error that is allowed while aligning the target tilt, in order not to miss the main beam (see 6.2.1). The phosphor window is imaged through a photographic objective (Fig.6.6-8c) on a $16bit$ intensified camera. The final recorded image has a resolution of $44.29\mu m/pix$.

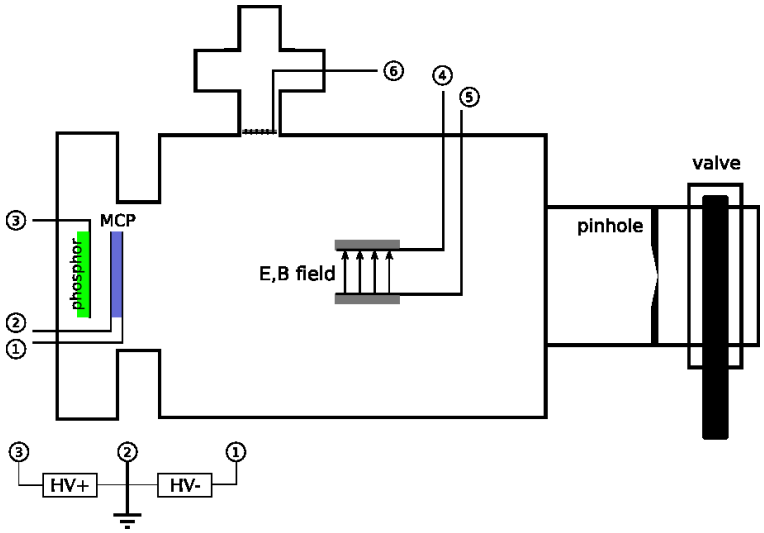


Figure 6.13: Schematics of the TP+MCP chamber (1)-(2) electrodes for MCP polarization; (3) phosphor input electrode; (4)-(5) electrodes for TP electric field; (6) shielding gate

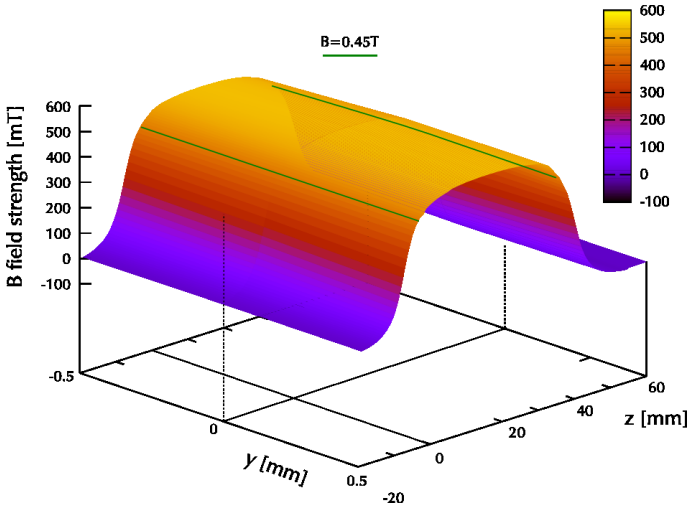


Figure 6.14: Map of the magnetic field strength on the plane $x = 0$. Important fringe field is found, which makes necessary the use of the map in numerical simulations for the calibration of the Thomson parabola.

To analyze consistently the spectral tracks from the MCP, the absolute reference of the spectrometer axis has to be set on the images. The axis is the prolongation of the chamber axis that is pictured in Fig.6.6, defined by the axis between the interaction point and the pinhole. The experimental procedure to observe this point uses the acceleration of non-ionized atoms and molecules from the Aluminum target. When shooting with a strongly attenuated laser (we used 1% of fully amplified power, $I_0 \sim 10^{17}\, W/cm^2$) no ion acceleration exists, though the intense heating of the metal foils produces evaporation. Neutral atoms are spread in the vacuum and their impact on the MCP plate is sufficient to produce a signal on the camera. Since their trajectories are not affected by the E, B fields, the impact point marks the acceleration axis.

During the full power shots, the area of the MCP that lies on the neutral axis has to be shielded[7], for the large quantity of debris that is produced during the interaction strongly saturates both the channel plate and the recording camera; such an electronic signal forms a halo on important part of the recorded image.

[7] I used a $3mm$ thick Plexiglas plate.

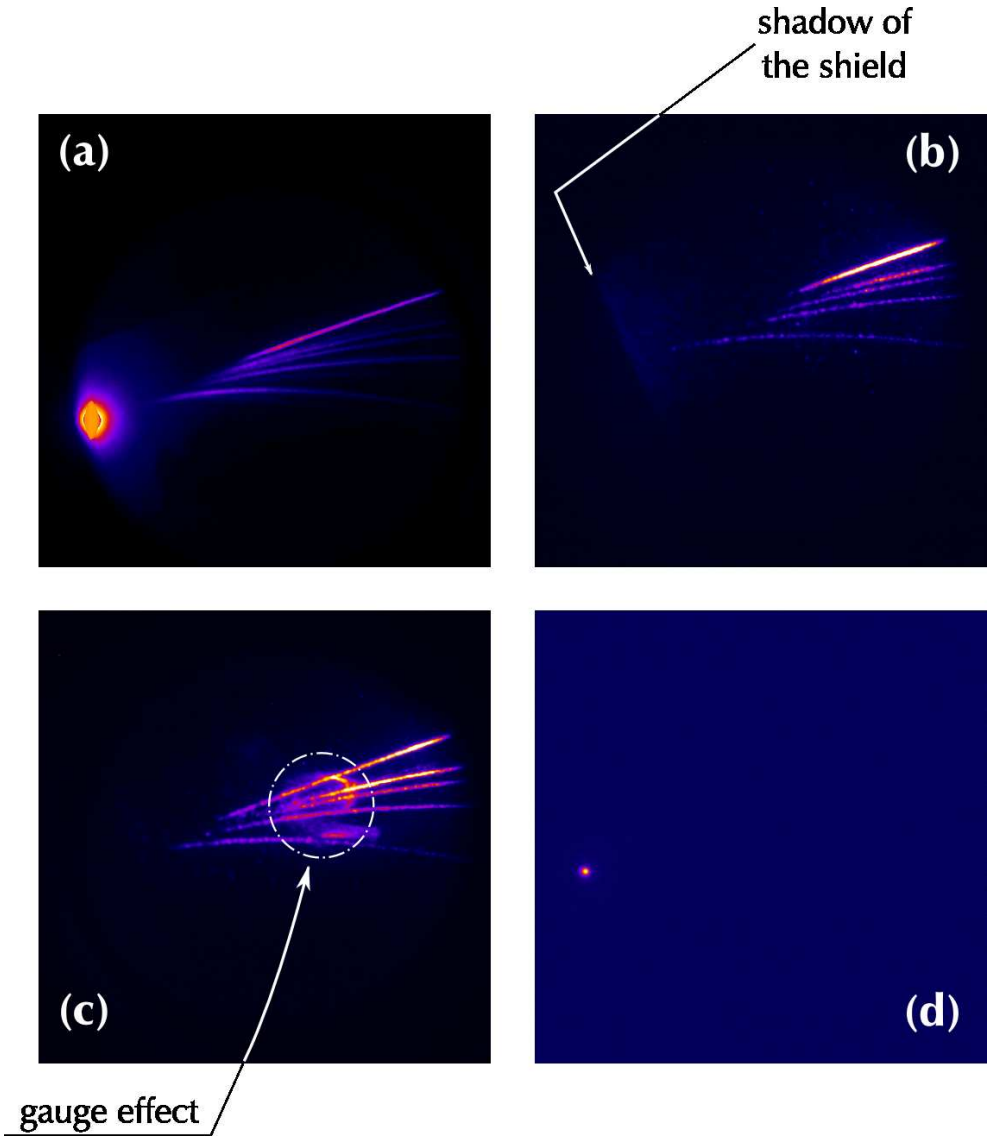


Figure 6.15: Examples of images recorded from the MCP: (a/b) unshielded and shielded zero; (c) effect of gauge ions at high MCP voltage; (d) zero point reference taken at low laser power.

Numerical treatment of images Once the image is recorded, its analysis is done in two steps: *(i)* a numerical integration, to get an histogram from every single track and *(ii)* the inversion of the simulated dispersion curves to define the energy scale.

The numerical integration is necessary to produce an histogram where the position and

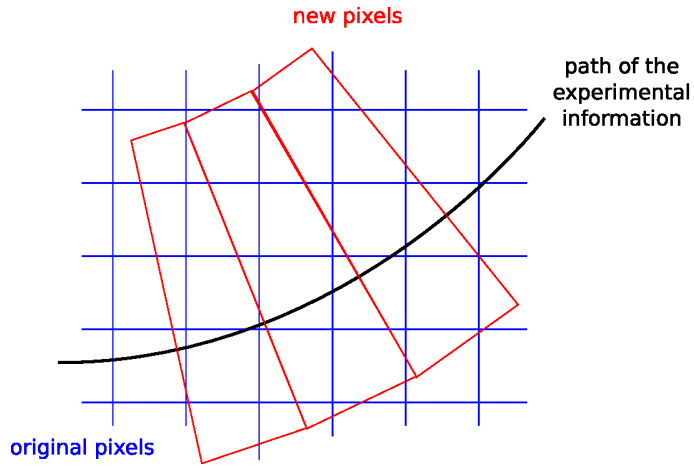


Figure 6.16: Strategy of analysis for the proton/ion tracks on the channel plate: the new histogram is built along the physically meaningful direction and super-pixels boundaries are defined; the count associated on a super-pixel comes from the partial integrals of the underlying histogram, defined by counts on the camera pixels.

the shape of bins is physically meaningful. For example, to analyse the component of the dispersion in energy due to the magnetic field, where the contained physical information is sufficient to obtain the energy spectrum, the bins have to refer, in distance, to a precise dispersion direction, which is not horizontal in the camera frame. The problem is resolved defining a set of super-pixels (marked in red in Fig.6.16) with a different geometry on the image and to associate them a certain number of counts. Assuming the count on each pixel from the original image to be uniformly spread on area, the count for a super pixel is calculated by integrating the underlying counts. The quantities are multiplied by a geometrical weight factor which equals to 1 for those entirely contained and to the surface fraction for the partially contained ones. For a given set of super pixels, the map of geometrical weights is calculated by Montecarlo integration of the two geometries. This is most important when the super pixel size becomes comparable to pixel size (Fig.6.16).

Chapter 7

Proton acceleration in the high contrast regime

The experimental campaign took place in the *Salle Jaune* between January 2007 and April 2008. Despite its long duration, it brought to roughly two months of laser time. The beginning of the experiment coincided with the re-opening of the laser installation after important upgrades of the system, notably the installation of the XPW stage and related devices, with the consequent rebuilt of the entire front-end. The third amplification stage (4-pass, $\times 20$) passed from cryogenic to water-chilled, which re-opened the problem of thermal lensing, needing static (refractive) correction. As a consequence the phase front worsens and day to day variation of the beam divergence is observed; moreover the refractive correction is calculated for a fixed thermal gradient in the crystal, hence for a precise flux of laser pumps. The user is not anymore free to continuously change the laser output energy.

This experimental campaign also aims to test, for the first time, the new proton diagnostic back-end, which includes the use of image plates to monitor the beam direction and divergence and the MCP-based Thomson Parabola setup (6.2.2).

In this chapter I focus on the results that are obtained with the setup described in Ch.6. The first part is dedicated to the results that are published in literature and that represent the present horizon of this topic. A second part is dedicated to the description of the experimental procedure that have been defined during the experiment. Finally the results are extensively presented and discussed.

7.1 Previous Works

The laser ion acceleration was first obtained by Gitomer et al.[36] in 1986, after the growing interest in late seventies on the presence of ion signals of different species coming from laser produced plasmas[18, 19]. Since then, a number of experiments have been performed, to understand the correlation between the characteristics of the accelerated charge (cutoff energy, relative importance of the different species, direction of emission and beam divergence) and the target (material, thickness) and laser parameters (energy, shape, peak intensity). The maximum energy with a long pulse, high energy laser[1] was obtained by Snavely et al. [93, 41] in 2000 on a $125\mu m$ thick aluminum target, with a proton energy cutoff of $E_{MAX} = 58MeV$. In the short pulse, low energy limit, the highest energy ever achieved is $E_{MAX} = 12MeV$ on the *Salle Jaune* laser system by S. Fritzler in 2003 [28] on a $10\mu m$ thick aluminum foil. Two other independent experiments, [79] for $\tau_L = 400fs$, $I_0 = 6.010^{18}W/cm^2$ and [77] for $\tau_L = 450fs$, $I_0 = 5.510^{18}W/cm^2$ report proton energies above $10MeV$ The energy spectrum is a Maxwellian-like distribution with a defined cutoff. The divergence of the proton beam changes depending to the proton energy, and the higher the energy, the lower the divergence. In [15] a divergence of 10° (FWHM) for $10MeV$ protons is measured.

Origin of the proton signal As discussed in 3.4, the expansion of a plasma where a difference in temperature exists between the electron and the ion population, produces the strong acceleration of the ions in the peripheral region. The origin of a proton signal among the different ion species is found in the contamination of the target's surfaces by hydrogenated compound (H_2O, organic molecules). This is in accord with the presence of a proton signal independently of the target material. The effect of the surface contamination has been confirmed by experiments where contaminants have been removed by target heating [66, 42] and laser ablation [67]: in these cases higher ion energies are observed, which confirms the electrostatic nature of the acceleration process.

Mechanisms of acceleration The protons are extracted and accelerated from the two exposed surfaces, the irradiated (*front*) [91, 103, 26, 79] and the non-irradiated (*rear*)[93, 102, 42]. The scientific community has been discussing long time about which of the two effects was producing the most effective acceleration. Some numerical studies

[1] $I_0 = 3 \times 10^{20}W/cm^2$ with $E_L = 48J$.

[83] showed that the most energetic and least divergent beam comes actually from the rear surface, while the front accelerated have bigger spread and lower cutoff energy. An extensive study on the correlation between the front surface accelerated ions and laser parameters has been performed by Habara et al. [40, 39] by using carbon targets that were deuterated only on one of the surfaces. Fuchs [29] experimentally showed that for a $30J$, $350fs$ laser interacting with a $20\mu m$ thick aluminum target, the most energetic protons are accelerated from the non-illuminated surface. Mackinnon [60] used a smaller intensity laser pulse to create a plasma with a gradient scale length of $100\mu m$ on the rear surface of a $25\mu m$ thick aluminum target. He observed that in conjunction with this plasma gradient, the proton energy cutoff was lowered from $21MeV$ to $< 5MeV$. In [49] is underlined that, being the front face accelerating mechanism independent from the target thickness, the front accelerated protons would take over in the spectrum when TNSA is made ineffective by target destruction. This argument is more deeply investigated in section 3.3.

Effect of laser parameters The laser parameters influence the acceleration mechanisms and the proton cut-off energy on a two-fold basis: *(i)* depending on the parameters themselves, like intensity and energy, and *(ii)* in conjunction with the some of the target parameters.
As a general rule, for a given intensity (power over surface), more energetic protons are produced by the most energetic pulse. Different situations need however to be analyzed specifically. For the front surface acceleration (3.4.1), the scaling law (3.26) shows a linear dependence between the cutoff energy and the normalized amplitude parameter $a \propto \sqrt{I_0} \propto \sqrt{E_L/\tau}$.

For the rear surface accelerated ions, no precise scaling law exist. Limiting ourselves to the dependence on the laser intensity, a simple rule can be obtained from the isothermal model (3.34)[2]. Neglecting for the moment the term in $\log()$., the energy is proportional to $k_B T_e$. From an extremely simplified calculation, one can write the electron temperature from

$$k_B T_e = (\gamma - 1)\, m_0 c^2 \tag{7.1}$$

[2]Note that the dependence to $k_B T_e$ outside the log() is the same in the adiabatic model (3.37)

for electrons having relativistic γ in the laser field (as defined in (2.13))[3]. For $a \gg 1$ it holds $\gamma \approx a$, which brings to $E_{max}^{(TNSA)} \propto k_B T_e \propto \sqrt{I}$. A more precise insight on the distinction between the dependence on the intensity and the dependence on the energy is presented in the discussion of the experimental results.

The dependence on the duration of the laser pulse is not completely clear. Some authors [61, 78, 68] reported of an ideal condition for the ion acceleration when the laser pulse is longer than $\tau_{recirc} = 2d/c$ where d is the target thickness. According to [61, 91] if the laser duration is higher than the time taken by hot electrons to cross twice the entire thickness, they experience a second heating on the -still- illuminated front surface after having been reflected in the Debye sheet on the rear one.

Effect of target thickness For front emitted protons, the thickness of the target plays only for its variable stopping power. Protons emitted by the illuminated surface of a thicker target will loose a larger amount of energy crossing the target bulk than those who were emitted from a thinner one. The correspondence between the measured energy and the initial energy is calculated through the numerical inversions of the continuous energy losses in a solid bulk (Fig.7.1).

In the TNSA acceleration, the charge separation depends on the density of hot elec-

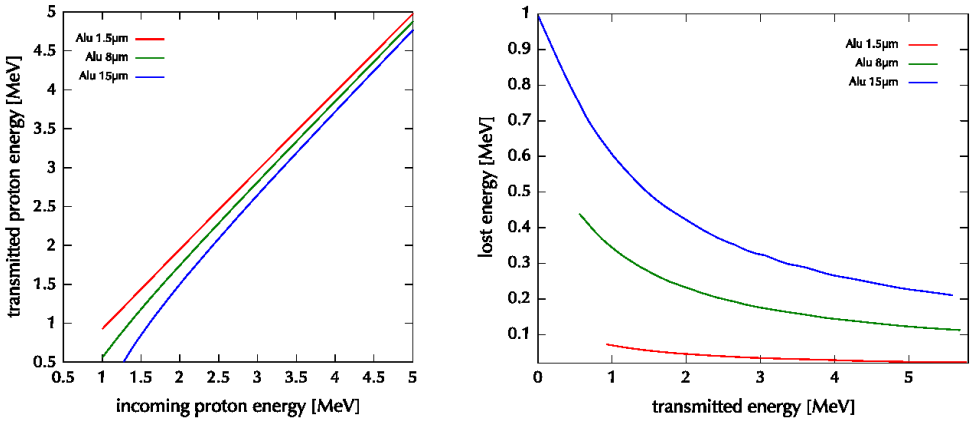


Figure 7.1: GEANT4[31, 32] simulation of proton energy loss depending on the thickness of an Aluminum bulk; *(left)* final energy vs. initial energy; *(right)* lost energy vs. final energy.

[3] $\gamma = \sqrt{a^2 + 1}$, $a = eA/mc$

trons that form the Debye sheath. The electron density n_e decreases according to the divergence in the electron transport [89, 90] through the target thickness which makes thinner targets to produce more energetic ions (Fig.7.2).

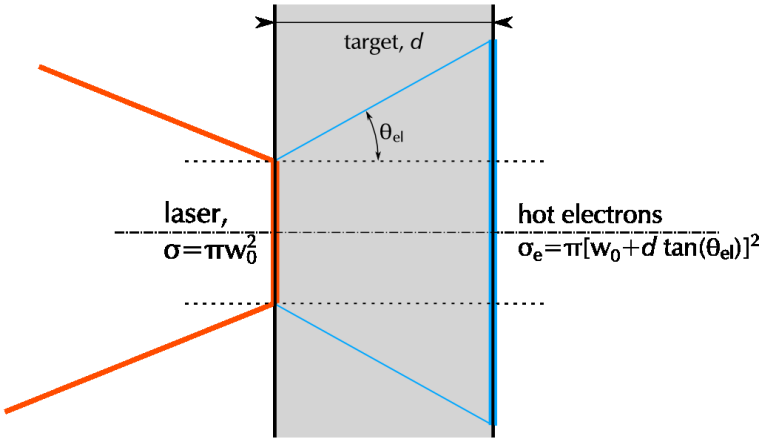


Figure 7.2: The divergence of the electron cloud being transported through the target results in a lower hot electron density on the non-irradiated surface. This adds the dependence on the target thickness for TNSA accelerated protons (neglecting the ASE and recirculation effects).

Effect of the laser pedestal In Ch.6 and Ch.3 I respectively introduced the reasons of the presence of a pedestal before the main femtosecond peak from a CPA laser chain and the effects of the heating of a metallic surface by an over-threshold intensity pulse. The production of a plasma gradient on the illuminated surface acts on the interaction mechanisms between the incoming laser peak and the electrons in the plasma: as discussed in section 3.3 the relative importance between the different interaction phenomena depends on the gradient scale length. Some authors [87] report a variation in the direction of acceleration of hot electrons as the gradient increases in length, making laser directed ponderomotive effects more important than Brunel and resonant absorption. The scale length depends on the pre-pulse intensity and on its duration. The presence of a pre-formed plasma density gradient can be beneficial for laser energy absorption and coupling to the electron component. In [4] is suggested that an optimum exists of a plasma gradient length of $L_{grad} = 4\lambda_{laser}$ in front of the target to maximize the laser absorption.

The ASE pedestal is also recognised as the main limitation to the use of thinner targets. In [49] an extensive study is presented to correlate the proton cutoff energy to the target thickness for three different pre-pulse durations. The laser peak with an intensity of $I_0 = 10^{19} W/cm^2$ is preceded by a pedestal of $\tau_{ASE} = 2.5ns$ at a contrast of 10^7. An optimum target thickness exists, and it is found to be dependent on the ASE duration. A reduction of τ_{ASE} of the 80% (from $2.5ns$ to $0.5ns$) reduces by the same factor the ideal thickness and increases the proton cutoff energy from $2.5MeV$ to $3.5MeV$. The linear variation of the ideal thickness with the ASE duration confirms the presence of a perturbation that is initiated by the ASE front itself and that travels at a finite velocity through the bulk. According to the same paper, the ideal thickness does not change when varying the laser intensity (keeping constant the contrast ratio). Nevertheless it has to be underlined that I_0 is reduced only by a factor of 0.67.
Following the argument in [49], thinner targets experience a limitation in the TNSA mechanism due to the formation of a plasma density gradient on the non-illuminated surface, as a consequence of the ASE-created shock breakout. The linear propagation law presented in [49] states

$$d_{ideal}[\mu m] \; = \; 3.6 \cdot \tau_{ASE}[ns] \tag{7.2}$$

which defines the timescale of the pre-pulse effect on the TNSA acceleration[4].

In [57] a deviation from the target normal is observed for the accelerated proton beam; it is suggested to be caused by the induced deformation and tilting of the normal direction of the rear surface, as a consequence of the shock wave breakout.

7.2 Experimental procedure

The thin aluminum foils are positioned between two nickel holders on a 5-axis (3 spatial, 2 tilts) mount. The initial focus position is set in a range of $\sim 200\mu m$ by simply looking at the speckle field that is produced by the helium-neon laser (collinear to the pump beam path) on the metallic target. This position is set as reference on the high-magnification focus reference (Fig.6.6-6). The two tilt axis are regulated so that moving

[4]This law apparently contrasts with the experimental results that are presented in Ch.5 for the reflectometry experiment. This discrepancy is discussed in 7.4.1.

the target holder in a range of 3×3 shot positions[5] doesn't change the relative focus reference by more than $50\mu m$[6]. This ensures a maximum tilt of $\sim 0.9°$ with respect to the pinhole-TP-MCP axis. The chamber is pumped down to a vacuum better than 10^{-3} and MCP is activated.

Error Estimation

The principle source of uncertainty in the experimental procedure is represented by the laser system itself. I believe that the fluctuation of its parameters can absorb all other errors on motors and image analysis. For this reason, in the rest of the chapter, the experimental the experimental proton energies are an average of many (at least three) shots of the same experimental configuration; the associated error bars are calculated from the width of distribution of the acquired data.

[5]There are $1.5mm$ between two adjacent shot positions.

[6]The perpendicularity between horizontal/vertical target movements and the MCP axis –referenced by a second Helium-Neon laser– has been previously checked by substituting the target holder with a mirror.

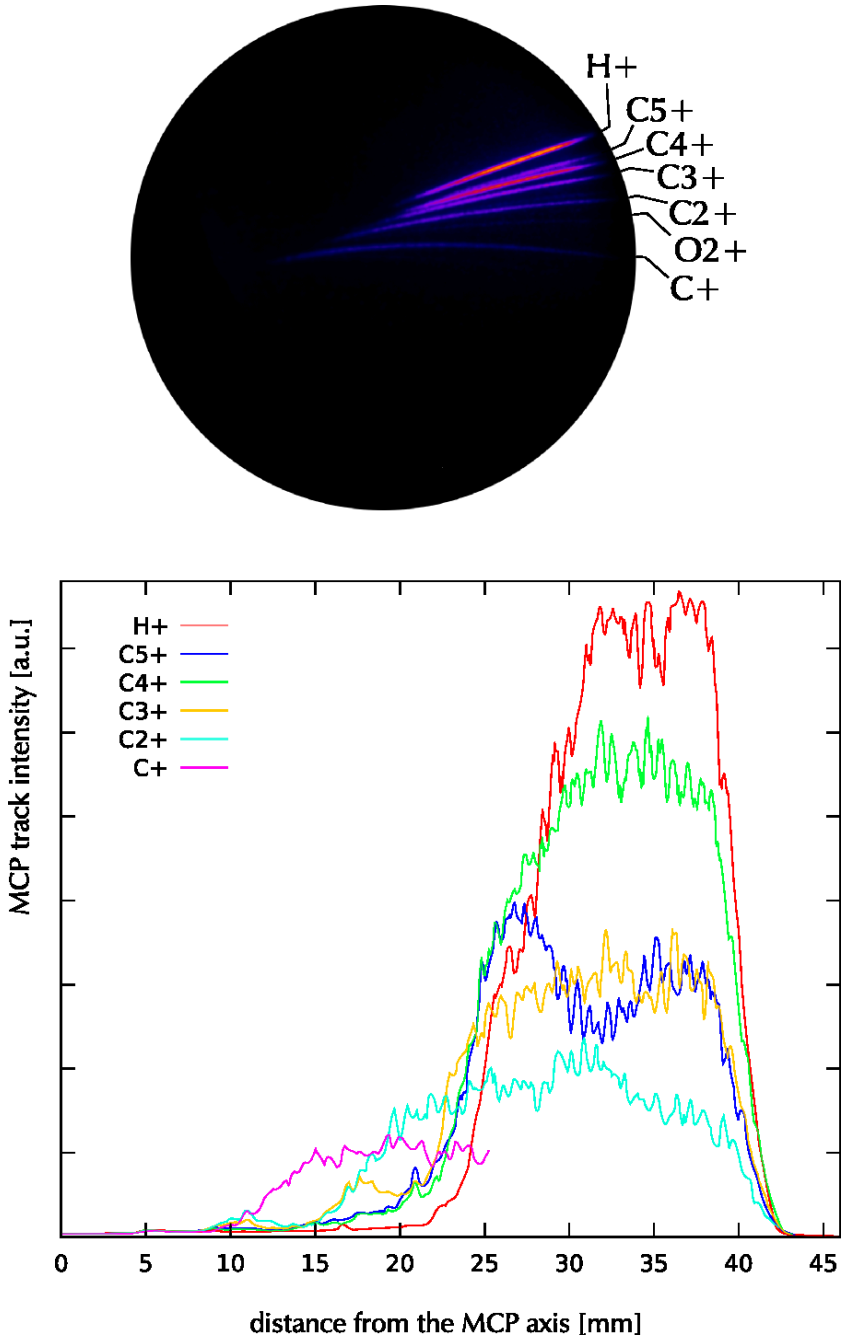


Figure 7.3: Real time result from a laser shot; *(upper)* MCP image (in fake colors) from a $d = 400nm$ aluminum target; *(lower)* spectral plot from the track on the image, obtained from spatial integration of the tracks (see Ch.6.2.2 for details on the analysis algorithm).

7.3 Validation of experimental parameters

7.3.1 Target focusing

The correct position in focus is searched from the direct experimental feedback of the proton signal: targets are moved around the first reference by steps of $25\mu m$ (which is above the resolution limit of the focus reference and about the Rayleigh depth of the parabola) and shot at least twice. According to (2.8) the peak intensity is changed which affects the expected ion energy cutoff. In the normal case, a single peak is found, well reproducing the change in intensity (Fig.7.4). The focus position is normally found no further than $150\mu m$ away from the helium-neon alignment and normal laser conditions give fluctuations lower than 10% in proton energy. In the waist, our laser and optics parameters produce a peak intensity in the order of $\sim 5 \times 10^{19} W/cm^2$.

The procedure shows two kinds of deviations from the standard behaviour: *(i)* a two-peaks structured plot and *(ii)* a flat region well wider than the expected Rayleigh range. This simple fact underlines the extreme improvement that a real time diagnostic system represents for the laser ion acceleration experiments. The two effects are now briefly discussed.

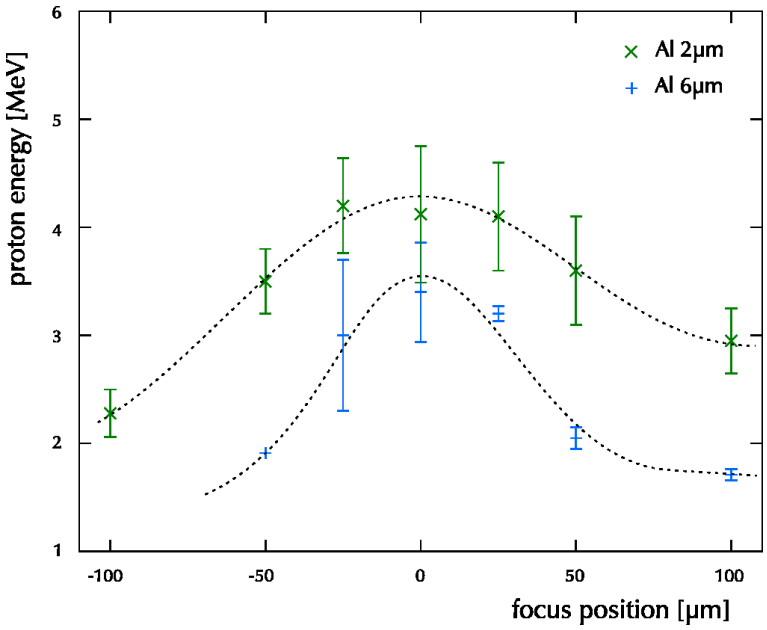


Figure 7.4: Proton cutoff energy for different focus position on Aluminum targets of $6\mu m$ and $2\mu m$. In the entire scanned area, more energetic protons are generated from the thinner target (dashed lines are added to help visualization).

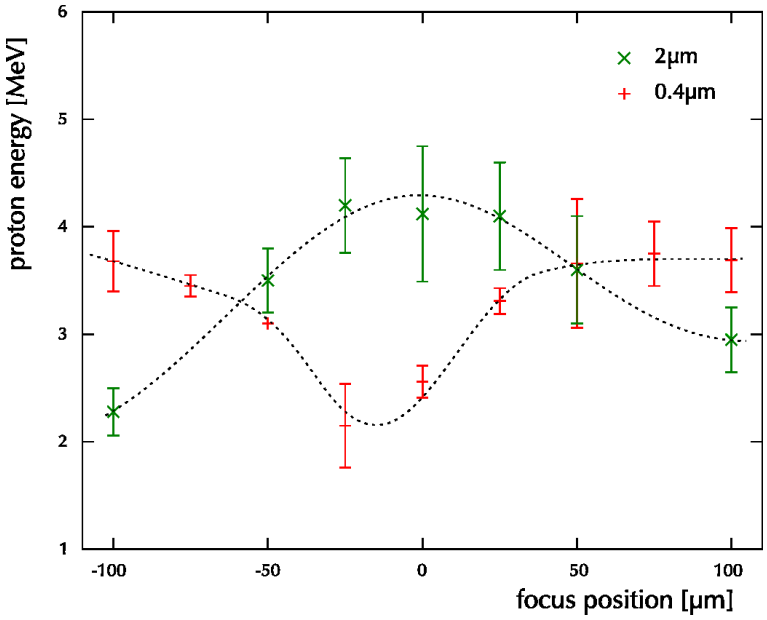


Figure 7.5: Proton cutoff energy for different focus position on Aluminum targets of $2\mu m$ and $400nm$. The plot for the thinner target exhibits a minimum in the focus position where a thicker target has a maximum (dashed lines are added to help visualization).

Contrast As the target is moved away from the beam waist, the peak intensity and the pedestal intensity decrease accordingly. In the case where the used target is too thin to hold the pedestal flux in the beam waist, a reduction of the peak intensity through the movement in focus (Fig.7.6) can produce better interaction conditions. In this case two peaks appears in the focus scan, symmetric around the beam waist (Fig.7.5). When this situation happens, even measurements from thicker targets have to be discarded.

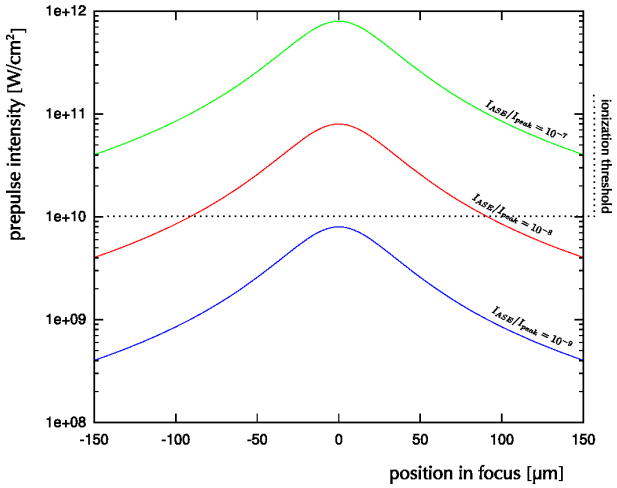


Figure 7.6: Theoretical pedestal flux for a 2.5ns pre-pulse at different contrast ratios.

Beam Aberrations It's been reported in literature of experiments where the proton energy cutoff seemed to be less sensitive than expected to the position of the target on the laser propagation direction. A proton signal of almost constant energy is sometimes found in a range in focus that is bigger than the supposed Rayleigh depth. The described case is showed in Fig.7.7. We believe this to be caused by a highly deformed phase front, possibly in conjunction with a misalignment of the parabola (which introduces strong astigmatism). In these cases the intensity distribution is not gaussian anymore and the peak intensity is less sensitive to the focus position. Moreover the quality of the beam in its waist is worsened, which produces less energetic ions even at the best focus position. This effect is normally removed by acting on the parameters of the deformable mirror (specially the radius of curvature) or the alignment of the parabola.

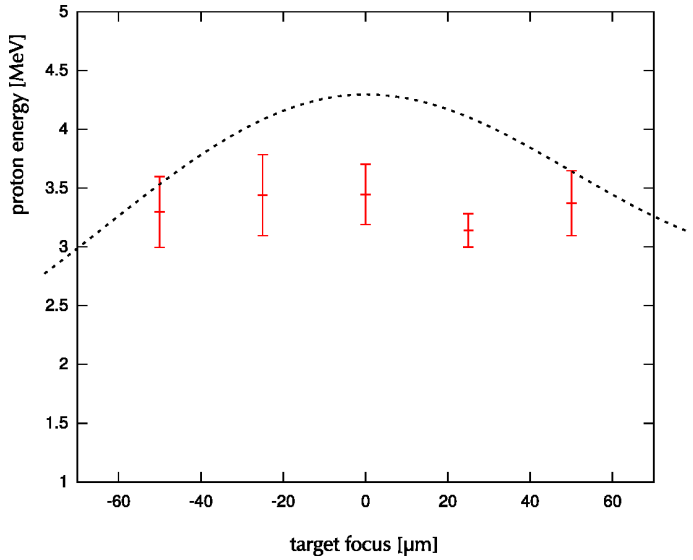


Figure 7.7: Maximum proton energy for different positions of a $6\mu m$ thick Aluminum foil. The dashed line is the same as Fig.7.4.

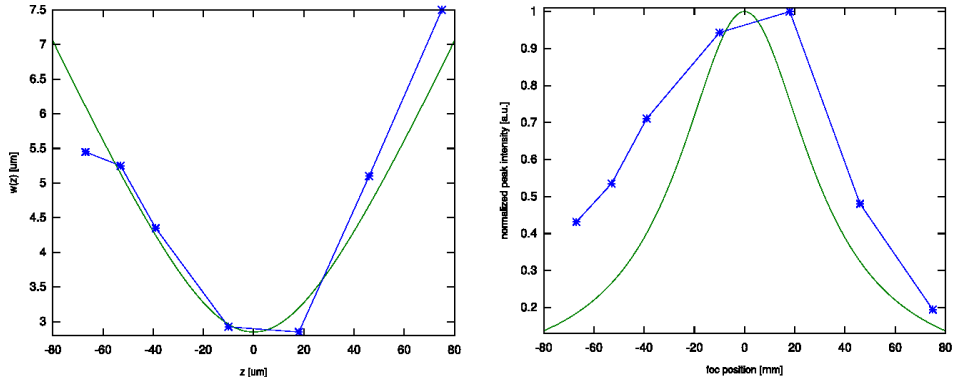


Figure 7.8: Comparison between the laser transverse profile at different positions around the focal spot (from images recorded by the camera) and a perfect gaussian beam; (*left*) waist size, (*center*) normalized peak intensity. The theoretical Rayleigh range is $z_0 = 34\mu m$.

.

7.3.2 MCP Calibration and Alignment

The MCP-based diagnostic system has to be validated from the point of view of *(i)* the direction of the measure, i.e. the solid angle where the incoming charge is collected, and *(ii)* the absolute measure of the proton energy.

In the realized setup, the MCP entrance pinhole sets a solid angle of beam integration of $\sim 5 \times 10^{-8}$sr that corresponds to an horizontal sweep angle of ~ 0.25mrad. This axis is fixed on the chamber axis. As previously discussed in section 7.2, the targets are aligned to a tilt better than $\sim 0.9°$ to the chamber axis. The typical half divergence of the more energetic part of the ion beam is in the order of 7° to 10° [15] which makes our alignment good enough not to miss the main beam. Nevertheless the possibility of a misalignment of the ion beam due to pre-pulse effect have to be considered, to ensure the self-consistency of the acquired data. In [56, 88, 57], the deformation of the rear target surface induced by the emerging shock wave is considered responsible of a lateral drift of the most energetic part of the ion beam, towards the laser axis. Given $\Delta\theta_P$ the half divergence of the highest energy part of the beam and θ_P the described deviation on the horizontal plane, in the typical case of $\theta_P = 5°$ and $\Delta\theta_P = 10°$ [7], the remaining uncertainty due to target tilt must be lower than $\sim 5°$. As a general precaution, whenever contrast effect like the one in Fig.7.5 are observed on the thinnest target, any other data from thicker foils is discarded.

Proton energy calibration The maximum proton energy is calculated from the distance between the cutoff of the proton track and the measured zero point. The distance is converted in microns and the calibration curve for the dispersion in the magnetic field (6.2.2) interpolated to find the corresponding energy. To validate the energies that are obtained in this way (so to validate the entire process in detection, measure and calibration of the Thomson Parabola), a certain number of shots has been repeated on MCP and on multiple CR39 foils covered by filters of appropriate stopping power.

7.4 Proton Acceleration with Enhanced Contrast Laser

This section is dedicated to the results that are obtained during the experimental campaign. The proton beam is generated varying the different parameters that enters in the interaction, the thickness of targets, the laser energy and the duration of the pulse. The last two do couple together in changing the flux on the target; crossing the two scans separates the correlation between the proton cutoff energy and the intensity/energy effects. In order to underline the dependence on laser contrast, the results are compared with the experimental data that was obtained by A. Tafo[96] on the same laser chain

[7] From [57] for $4MeV$ protons from Aluminum target with $3ns$ pre-pulse at 10^7 contrast.

(before the XPW was inserted) and what is obtained by T. Ceccotti et. al [12] at the CEA-Saclay with a double plasma mirror.

Laser Conditions

If not specified otherwise, the experimental data here presented are obtained with a total laser energy of $1.5J$ before compression and a contrast better than 10^9 up to $500ps$ before the main peak.

7.4.1 Correlation with Target Thickness

The proton signal is recorded from targets of different thicknesses, from $15\mu m$ to $400nm$ at the best focus position. The evolution of the proton energy cutoff (Fig.7.9, red points) shows a meaningful dependence. In the direction of increasing thickness the proton en-

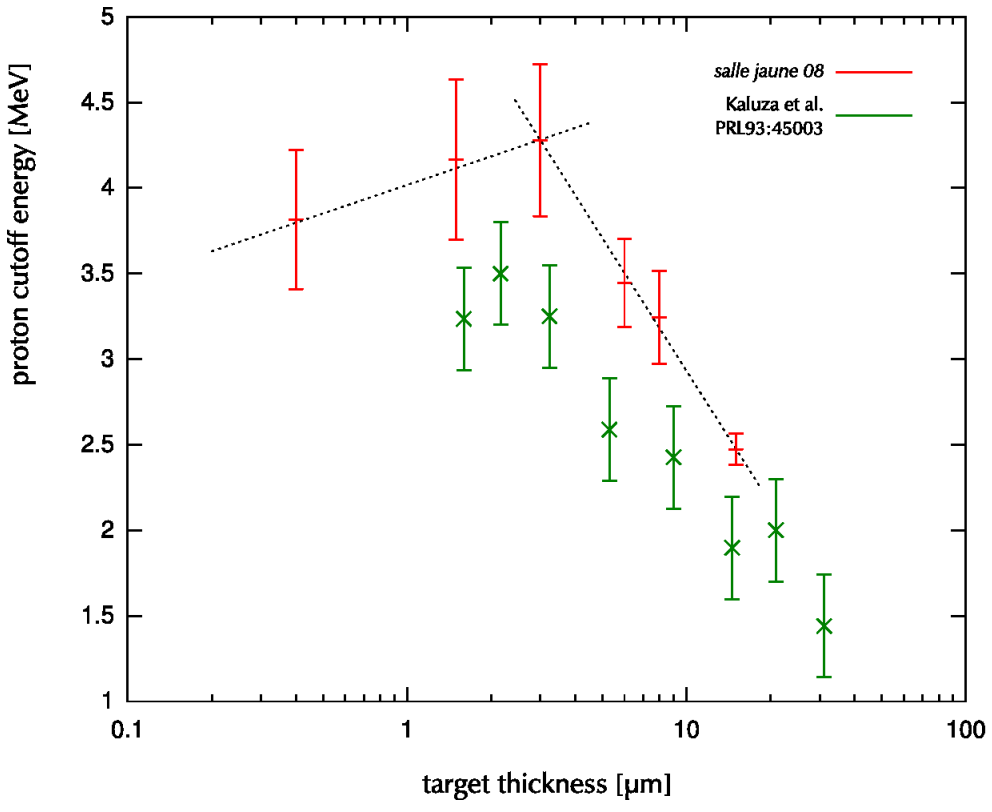


Figure 7.9: Correlation between proton cutoff energy and target thickness. The experimental data *(red)* is compared with points *(green)* from Kaluza[49] Fig.1 for $I = 1.0 \times 10^{19} W/cm^2$ and $t_{ASE} = 0.5ns$.

ergy decreases, consistently with the increased spread of the electron cloud, travelling through the thicker target. An ideal thickness is found for $d = 2\mu m$.
The *green* set in Fig.7.9 reports, for comparison, the points from the best contrast case in [49], for a contrast of 10^7 and a pre-pulse cut to $0.5ns$ from the main pulse, at $I = 10^{19}W/cm^2$([8]). Our data on the plot changes in derivative around $2\mu m$ thickness: for lower thicknesses the proton cutoff energy is found to decrease. It is important to underline that the behaviour in the two cases is qualitatively different. In our experimental case the supposed detrimental effect of the pre-pulse has a timescale which is longer than expected. Over a span of $\times 5$ in target thickness (from $400nm$ to $2\mu m$) the decrease in energy is around the 10%, and almost absorbed in the error bars. In the cited paper it is suggested that the ion signal for thicknesses $d < d_{ideal}$ could be produced mostly by front surface acceleration, achieving lower energies but remaining active even when TNSA is made ineffective by the plasma expansion on the rear surface. Since the scaling in energy for front face acceleration is only due to the stopping power of the target, this would in principle explain why in our scan (Fig.7.9) the proton cutoff energy remains almost constant; in fact (see Fig.7.1) for $E_p \sim 4MeV$ and $d < 2\mu m$, the stopping power would account for less than $100keV$ of energy loss. Nevertheless, if the $4MeV$ signal were originated from the front surface, higher energies on targets at $d > 2\mu m$ should have been observed. A possible explanation might instead come from [73]. The ion acceleration during the expansion of the high electron temperature plasma is limited by the presence of a density gradient in the cold ion distribution (see section 3.4.2). The timescale of the expansion of this gradient is bound to the electron temperature that is produced by the shock itself. The difference between the two plots in the figure can be explained by two experimental conditions with a very different contrast level (10^7 vs. 10^9) although with comparable τ_{ASE}.

Estimation of the Contrast

If we follow the argument in [49] for the presence of an ideal thickness, the plot in Fig.7.9 enables us to infer an estimation of the duration of the laser pedestal. The reflectometry measurements showed a shock wave that propagates at a speed of $15\mu m/ns$ ((5.11)), whereas in the cited paper, the experimental fit of the ideal thickness of the target versus ASE duration gives an "effective" speed of propagation of the shock of $3.6\mu m/ns$. Considering that in Fig.7.9 the optimal thickness is $1.5\mu m$, from the two speeds I get

[8] For proton energy comparison it should be taken in account that green points are for $\tau = 150fs$, $w_0 = 2.5\mu m$ and $E_L = 510mJ$.

$$100ps < \tau_{ASE,estim} < 400ps \tag{7.3}$$

7.4.2 Correlation with Laser Energy and Pulse Duration

Energy The proton spectra are recorded varying the energy in the laser pulse but keeping the optimal compression ($\tau < 35fs$). The energy is varied by inserting neutral optical densities of different thicknesses at the end of the laser chain, just before the compressor, to attenuate the intensity of factors $10^{-1/3}$, $10^{-2/3}$ and 10^{-1}. The proton energy cutoff is shown in Fig.7.10-*(upper)*. The continuous lines are $E_p \propto \sqrt{I_0}$ and $E_p \propto \log(I_0)$ to show how the scaling in intensity changes from the first to the second dependence as target gets thicker. The reason of this behaviour is not clear. A still unconfirmed hypothesis suggests that the target thickness may act on the weight of the logarithmic term in the relationship (3.34)

Pulse duration The duration of the pulse is increased by acting on the separation between the gratings in the compressor, which produces a longer and chirped pulse. The proton cutoff energies are plotted in Fig.7.10-*(lower)*; to ensure that no dependence on the chirp sign exists, the gratings are moved in the two directions (increasing and decreasing their separation, thus producing a negative and a positive chirp) and the couples of points that correspond to the same pulse duration, superposed. The behaviour for the two shown thicknesses is different. From the thinner one ($d = 1.5\mu m$), the proton cutoff energy decreases monotonically with the laser peak intensity; on the thicker one ($d = 15\mu m$) we observe *(i)* a smaller sensitivity on the pulse duration and *(ii)* the presence of an ideal duration, with a maximum in proton energy that situates around $\tau_L = 200fs$. In [61] it is observed that for a pulse of a given duration, a transition in the maximum proton cutoff energy exists when the thickness becomes smaller than $d < c \cdot \tau_L/2$, which means that the laser pulse duration is longer than the time that is needed to relativistic electrons to cross twice the target thickness. The proposed explanation is that if previously heated electrons, reflected in the Debye sheath on the rear surface, arrive to the front when the laser pulse isn't over yet, a more effective heating can take place, which results in the acceleration to higher ion energies. The recirculation time is $\tau_{recirc} \simeq 2d/c$ and the recirculation condition $\tau_L > \tau_{recirc}$. In our experimental case, the optimal duration is found at $\tau_L = 200fs$ on a $d = 15\mu m$, which doesn't correspond to the expected recirculation time of $\tau_{recirc} = 100fs$.

I hypothesize that the observed maximum happens at the equilibrium between *(i)* the

enhancement of the laser light absorption, as a consequence of the longer pulse tails and the slower plasma heating, and *(ii)* the decreasing of the laser peak intensity.

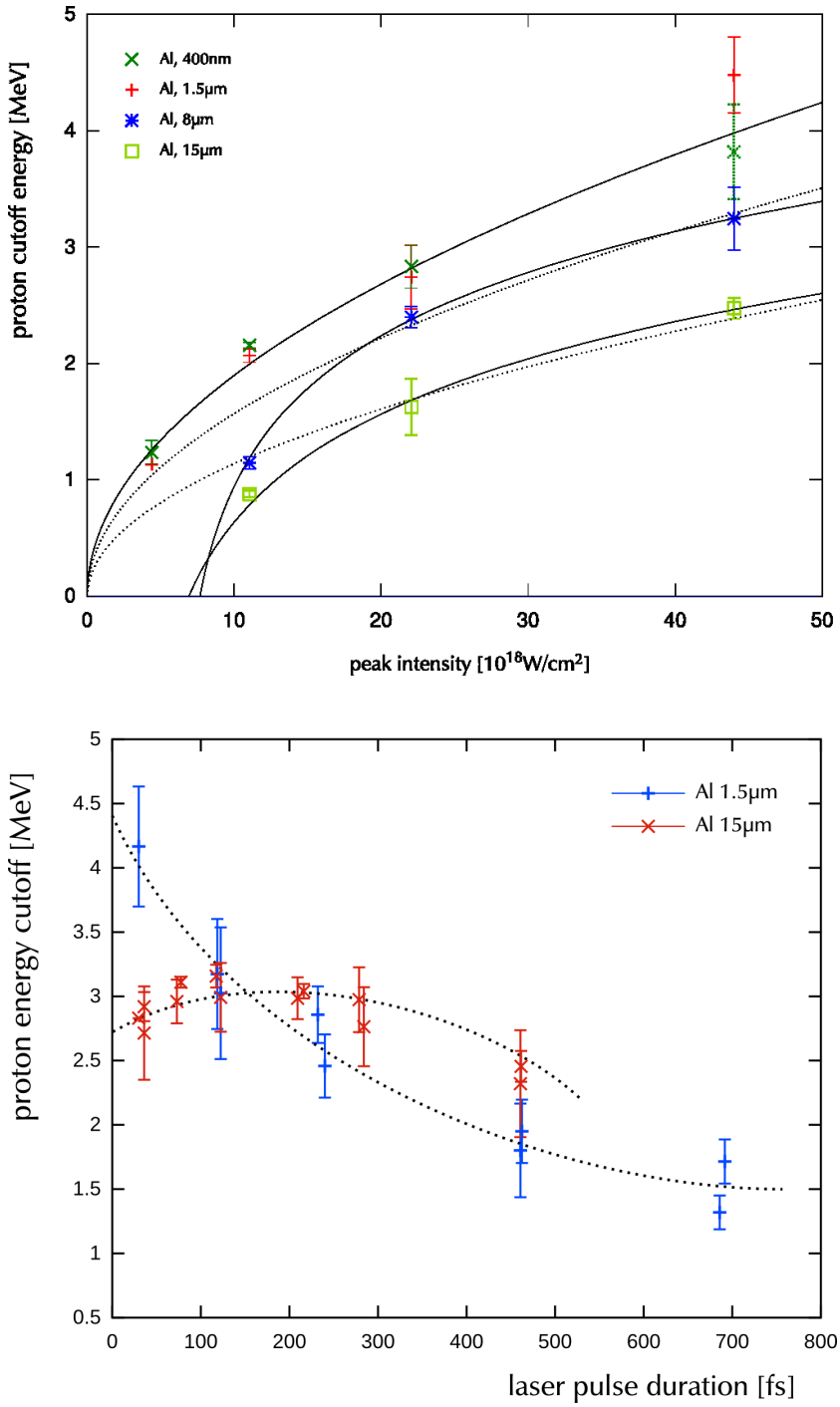


Figure 7.10: *(upper)* Scan in laser energy (laser duration is kept constant) for different target thicknesses. Black lines are plotted with $E_p \propto \sqrt{I_0}$ and $E_p \propto \log(I_0)$. Note that the point at $d = 400nm$ at the highest laser intensity has a proton energy lower than the $d = 1.5\mu m$. *(lower)* Scan in laser duration (at constant energy).

Intensity correlation In Fig.7.11 the experimental points from duration and energy scans (Fig.7.10 upper and lower) are presented in correlation of the final peak intensity for the two thicknesses $1.5\mu m$ and $15\mu m$. The qualitative difference is clear:

- The red points (duration is changed at constant energy) show a fast decrease (logarithmic) on the $d = 1.5\mu m$, and the maximum at $\tau_L = 200fs$. It is interesting to note that, for $\tau_L > 200fs$, the proton signal from the thicker target is more energetic than the one from the thinner.
- The green points (energy is changed) confirm the logarithmic behaviour for the $15\mu m$ target and a slower decrease (on the lower intensity side) for the $1.5\mu m$.

As a general rule, the emerging scenario is a more marked sensitivity on total energy for thick targets and a strong correlation to peak intensity for thinner ones.

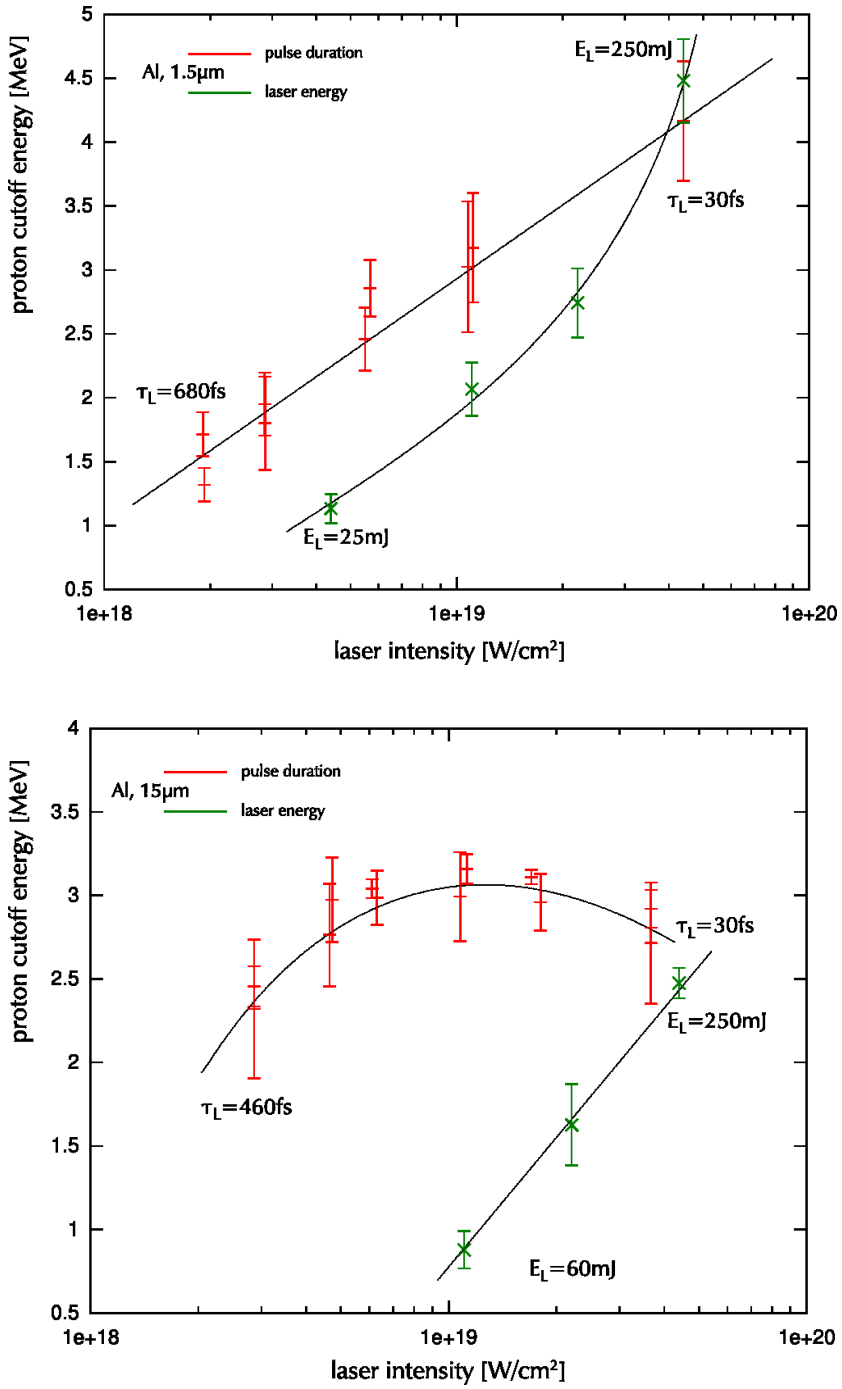


Figure 7.11: Scan in peak intensity from the experimental points in Fig.7.10 for Aluminum $1.5\mu m$ *(upper)* and $15\mu m$ *(lower)*. Red points show the behaviour for constant laser energy ($E_L = 250mJ$); green points for constant laser pulse duration ($\tau_L = 30fs$).

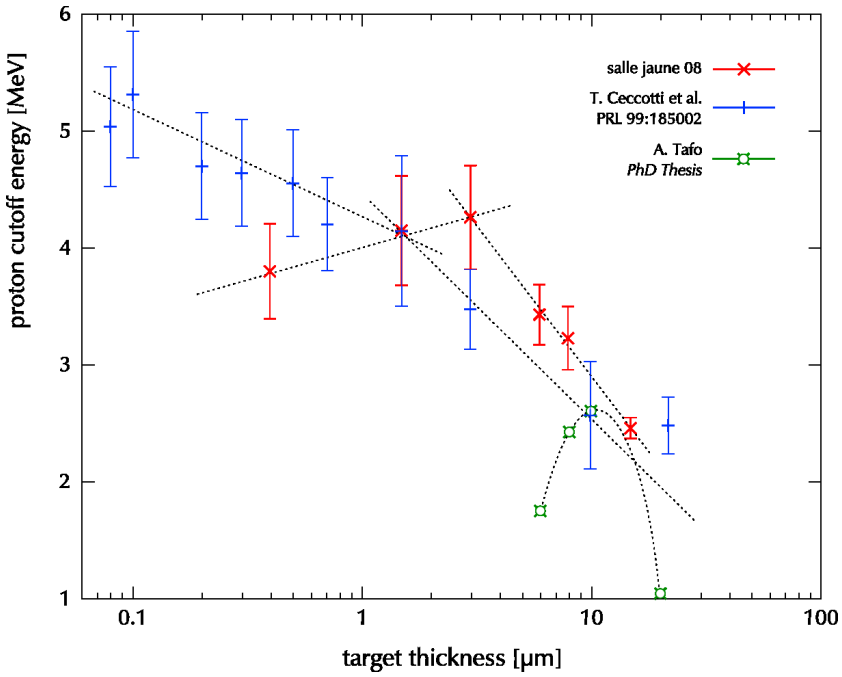


Figure 7.12: Comparison between different thickness scans. Red × are the experimental points that are reported in Fig.7.9; blue + are the results reported by T. Ceccotti et al. in [12] for $E_L = 650mJ$, $\tau_L = 65fs$ and $I_0 = 5 \times 10^{18} W/cm^2$, with a 10^{10} contrast ratio from a double plasma mirror. Green circles are the results that were obtained by A. Tafo [96] in 2004 on the *Salle Jaune* laser system before the installation of the XPW system.

7.5 Discussion and Conclusions

During the experimental campaign, ions and proton beams have been produced by the direct interaction between a laser pulse and a thin solid target. These are the first results that are produced with the XPW system for the contrast enhancement. The ion signal that is produced is stable and repeatable: in Fig.7.13 is reported the proton peak energy for 8 shots in a row, in the same experimental condition. The quality of the contrast is confirmed by the possibility to shot on thinner targets. For example in Fig.7.12 is presented the direct comparison between the proton cutoff energies with the XPW and what is obtained by T. Ceccotti et al. [12] with a double plasma mirror, which guarantee a contrast of 10^{10} and a perfectly clean pedestal. As a reference are presented, in the same image, the experimental points for a thickness scan that were obtained in 2004 by A. Tafo et al., using the *Salle Jaune* laser chain without any contrast improvement technique (the 3ω profile is presented in the upper part of Fig.6.3).

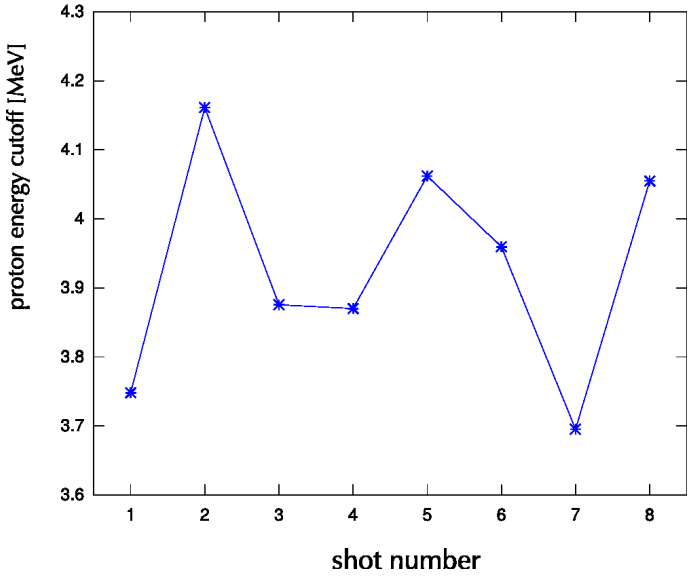


Figure 7.13: Proton cutoff energy for 8 shots in a row on $3\mu m$ thick aluminum target. The average energy is $E_p = 3.9MeV$ with a peak-to-valley fluctuation of 12%.

Further studies are needed to completely understand the experimental evidence here presented. During the very last part of the experimental campaign, a two beams experiment is set up. Here a small part of the pump beam is used to pre-heat the target surface before the interaction with the main UHI peak. The preliminary studies on front and rear face in Ch.4 and Ch.5 enable us to define the space of parameters for a pre-heating pulse, with the aim of observing the correlation between a preplasma (that is created with known parameters) and the accelerated proton beam. A preliminary analysis of the obtained results is presented in App.A.

Part IV

Résumé en Français

Chapter 8

Contexte du Travail de Recherche

Les récents développements techniques des lasers permettent de produire des impulsions laser de très fortes puissances. Le dynamisme des recherches, l'évolution rapide des techniques optiques et de leurs maîtrises ainsi que la variété des applications ont ouvert la course à la production industrielle de chaînes lasers de plus en compactes, de plus en plus stables et délivrant des puissances de plus en plus élevées. Les ultra-hautes intensités ainsi obtenues ouvrent la voie à l'exploration de domaines de recherche ou de régimes d'interaction nouveau comme le régime relativiste au sein duquel les électrons soumis au champ laser oscillent à des vitesses relativistes. Ils permettent aujourd'hui la production efficace de faisceaux de particules chargées et énergétiques. Mon travail de thèse s'inscrit dans le cadre de la production compacte de faisceaux d'ions, créés à partir de cible mince irradiée par le faisceau laser intense.

8.1 Les sources laser ultra-intenses

A chaque saut technologique correspond en général une avancée scientifique. Dans le domaine des lasers l'augmentation progressive de la puissance des lasers a suivi la même règle. Ceci a été rendu possible en augmentant l'énergie des lasers et/ou en diminuant la durée des impulsions laser. La technique dite de **CPA** (*"Chirped Pulse Amplification"*, amplification à dérive de fréquence), développée à partir des années '80, consiste dans l'amplification optique des impulsions laser étirées (ref. équation 1.1-p.5 et figure Fig.1.2-p.5). L'utilisation de ces impulsions étirées permet de limiter la puissance crête pendant l'amplification, augmentant ainsi la quantité maximale d'énergie par impulsion sans endommagement des amplificateurs. La compression temporelle finale des impulsions amplifiées permet enfin d'achever des impulsions ultra-brèves ($\tau <$

$1ps$) ayant des puissances crêtes pouvant atteindre les dizaines/centaines de terawatts. De telles installations peuvent aujourd'hui fonctionner à des taux de répétition de l'ordre de la dizaine de Hz, avec des énergies par impulsion limitées à quelques Joules.

8.2 L'accélération d'ions par laser

Lors de l'interaction d'une impulsion laser avec une cible solide, la pré-impulsion ou le pied de l'impulsion laser ionise très rapidement la cible, libérant les électrons qui vont absorber la plus grande partie de l'énergie du laser (pour les seuils d'endommagement, voir figure Fig.3.2-p.19): un plasma est ainsi créé[1]. Une impulsion laser (visible) ayant une intensité supérieure au seuil à $10^{18}W/cm^2$ est dite "relativiste", car les électrons soumis à son champ électrique y oscillent à des vitesses relativistes (équation 2.9-p.13). Étant donnée la brièveté de l'impulsion ($\tau < 1ps$), la composante du plasma la plus active au cours de l'interaction est celle électronique (les composantes ioniques ont des fréquences plasmas – éq. 3.1-p.15 – inférieures). Lors de l'interaction laser - plasma, différents mécanismes collectifs se produisent et permettent le couplage de l'énergie laser en énergie cinétique communiquée aux électrons (absorption collisionnelle, chauffage $j \times B$, absorption résonante, chauffage de Brunel): leurs importances relatives est liées aux paramètres du plasma présent sur la surface éclairée. Les électrons les plus chauds ainsi créés à la surface traverse la cible. Les courants associés sont si forts que les électrons peuvent se propager dans la cible non perturbée de façon très collimatée. Lors de leur émergence en face arrière, celle-ci devient rapidement ionisée et transformée en plasma qui va se détendre dans le vide: son expansion est responsable de l'accélération ionique et de la formation de faisceaux d'ions très collimatés dont les énergies augmentent du fait de la séparation de charge produite à l'interface plasma/vide du fait de la séparation de masse. Plus la température électronique est grande et plus la séparation de charge est importante, et, par là même la valeur du champ électrique accélérateur. Ce mécanisme, est connu sous le nom du "TNSA" (*Target Normal Sheath Acceleration*, accélération de gaine à la normale à la cible) et il est, avec les paramètres explorés dans ma thèse, le mécanisme le plus efficace d'accélération ionique.

8.2.1 Dépendance du couplage avec les paramètres laser

Les paramètres laser jouent plusieurs rôles dans l'ensemble du processus d'accélération ionique, de façon dépendante ou pas des paramètres de la cible. Ce travail de recherche

[1] Pour les différents mécanismes d'ionisation, voir équation 3.11-p.18

est spécialement dédié aux effets du contraste laser. Le piédestal d'une impulsion laser est l'énergie laser qui précède l'impulsion crête, en général elle s'étale sur une échelle entre la centaine de picosecondes et quelques nanosecondes. La forme de ce piédestal aussi bien que son intensité moyenne (le rapport, dit contraste, entre le valeur crête du pic d'intensité et le niveau du piédestal) sont propres à chaque chaîne laser. Étant données les intensités extrêmes en jeu ($I > 10^{18} W/cm^2$) les niveaux de contraste normalement obtenus ($10^6 - 10^8$) sont tels que le flux d'énergie du piédestal dépasse le seuil d'ionisation de la matière. C'est ainsi que la présence du piédestal intervient dans l'interaction laser-cible. Dépendamment de ses paramètres (durée, énergie) le piédestal va créer un plasma de surface dont la mesure des paramètres, tels que température, densité, longueur du gradient, est cruciale pour l'évolution des phénomènes produits lors du passage de l'impulsion courte. Le temps de débouché du choc provoqué par le piédestal dépend de l'épaisseur de la cible. L'arrivée de cette onde de choc sur la surface arrière produit sa détente dans le vide, réduisant l'efficacité du TNSA.
Les dernières techniques d'amélioration du contraste (miroirs plasma, absorbants saturables, XPW[2]) permettent d'augmenter significativement le contraste, jusque des valeurs de $10^{10} - 10^{12}$: ces niveaux de contraste sont suffisants pour éliminer la formation d'un plasma qui précèderait l'impulsion principale. L'absence de ce pré plasma peut réduire l'absorption de l'énergie du laser, améliorer la stabilité de l'interaction et donc du faisceau de protons, et permettre enfin l'accélération de protons plus énergétiques issus de cibles de plus en plus minces.

8.3 Structure du manuscrit de thèse et de son résumé

Ce manuscrit est organisé comme suit. Les chapitres Ch.2 et Ch.3 sont dédiés aux notions de physique de laser et de plasma, nécessaires à la définition du cadre de recherche. Les chapitres Ch.4 et Ch.5, résumés dans le chapitre Ch.9, sont dédiés aux expériences préparatoires sur le sujet de l'interaction laser-matière à intensité moyenne: deux campagnes expérimentales ont été menées dans l'installation laser de la *Salle Verte* au LOA pour la caractérisation des surfaces avant et arrière (éclairée et non éclairée) soumises à des impulsions femtosecondes. Les chapitres Ch.6 et Ch.7, résumés dans le chapitre Ch.10, sont enfin consacrés aux expériences d'accélération de protons avec le laser femtoseconde, multiterawatt de la *Salle Jaune*. Les conclusions des activités de recherche et ses perspectives sont enfin résumées dans le chapitre Ch.11.

[2]Génération d'onde à polarisation croisée

Chapter 9

Expériences préparatoires sur l'interaction laser - matière à moyenne intensité

Une partie importante de mes activités de recherche concerne la caractérisation de l'interaction entre une impulsion laser d'intensité moyenne ($I > 10^{11} W/cm^2$) et une cible solide. L'activité expérimentale présentée concerne l'évolution temporelle des surfaces *avant* (éclairée par le laser) et *arrière* de cibles minces, suite à son interaction avec l'impulsion. Pour ces expériences les paramètres du laser sont choisis afin de reproduire au mieux l'interaction du piédestal d'une impulsion à ultra haute intensité.

Deux expériences ont été réalisées sur l'installation expérimentale de la *Salle Verte*, au sein du *Laboratoire d'Optique Appliquée*; les deux sont du type *pompe/sonde*: une impulsion (dit *pompe*, ayant une intensité suffisante) est utilisée afin de créer le plasma sur la surface d'une cible. Une deuxième impulsion (dit *sonde*), se propageant à un délai connu par rapport à la première, est ensuite utilisée pour examiner la situation produite.

9.0.1 Source laser utilisée

La chaîne laser de la *Salle Verte* (voir Fig.4.3-p.39) est une chaîne CPA, capable de produire des impulsions ayant une durée de $\tau = 150 fs$ à la longueur d'onde de $\lambda = 800 nm$. Au début du système, un train d'impulsions est produit par un oscillateur Titane-Saffire (Ti:Sa), pompé par un laser continue à l'argon. Les impulsions sont ensuite étirées jusqu'à $\tau = 400 ps$ et amplifiées par deux systèmes amplificateurs (8

et 4 passages): l'énergie finale atteinte est de $100mJ$ pour chaque impulsion avant compression. Une lame biréfringente est utilisée pour générer deux faisceaux séparés selon la direction de polarisation, permettant ainsi à l'utilisateur la liberté de choisir les rapports d'énergie à envoyer vers deux compresseurs séparés. Pour les deux expériences qui suivent, la lame polarisée est réglée afin d'avoir $E_p \approx 30mJ$ d'énergie dans le faisceau de *pompe* et $E_s < 10mJ$ d'énergie dans le faisceau de *sonde*. L'impulsion de pompe est focalisée, en atteignant une intensité sur cible de $\approx 10^{15} W/cm^2$.

9.1 Étude interférométrique des premiers instants d'expansion d'un plasma crée par laser

L'interaction entre une impulsion laser dépassant une intensité de seuil (Fig.3.2-p.19) et une cible à densité sur-critique provoque le passage à l'état plasma d'une partie du solide. On y observe *(i)* la formation et la détente d'une couronne plasma, *(ii)* la création d'une zone de transition se propageant vers la partie non perturbée du solide (Fig.4.1-p.38). L'intérêt de cette première expérience est d'étudier l'évolution temporelle de la plume plasma créée, dans les premiers instants de son expansion.

Le plasma est créé par l'impulsion *pompe* sur la surface d'un fil d'aluminium de $200\mu m$ de diamètre (Fig.4.2-p.39). Un système de Mach-Zender (Fig.4.6-p.42) est mis en place, un des deux bras traversant le plasma en direction normale par rapport à sa détente (Fig.4.7-p.43). Un des miroirs du Mach-Zender dévie un des faisceaux par rapport aux autres, ce qui fait apparaître une fréquence spatiale (dit "hétérodyne") sur l'interférogramme; l'information expérimentale est enregistrée sous forme de déviation des franges.

Le faisceau *sonde* est doublé en harmonique ($\lambda_{sonde} = 400nm$) par un cristal doubleur BBO. Cette procédure est introduite afin de *(i)* pouvoir pénétrer des densités plasmas plus élevées et *(ii)* de différencier les deux longueurs d'onde, celle du *pompe* et celle du *sonde* sur la caméra CCD qui enregistre les interférogrammes. Le délai entre les impulsions sonde et pompe est réglé par une ligne de retard à précision micrométrique.

9.1.1 Reconstruction de la carte 3D des densités

La géométrie du problème est schématisée dans la figure Fig.4.2-p.39. La carte en trois dimensions de la densité électronique $n_e(\underline{x}) = n_e(r, d, \theta)$ du plasma est obtenue en partant d'une mesure du déphasage intégré long de l'axe y. La dépendance entre l'indice de

réfraction local $n\,(\underline{x})$ du plasma et sa densité électronique est calculée à partir du modèle de plasma froid (le calcul détaillé est présenté en annexe B; la formule finale est celle de l'équation 4.2-p.50-*bas*). Pour ce qui concerne l'analyse des images expérimentales, les cartes de phase sont calculées numériquement; grâce aux développement des outils de nettoyage numérique, spécifiquement conçus, on a pu obtenir une information expérimentale même dans les cas des images avec un faible rapport signal/bruit. Dans l'hypothèse d'une plume plasma de symétrie cylindrique, la carte 3D est obtenue à partir de l'inversion d'Abel appliquée à la tomographie mono dimensionnelle mesurée 4.2-p.50-*haut*.

9.1.2 Procédure expérimentale

La ligne à retard est réglée pour que les deux faisceaux soient synchronisés. Le retard entre le Sonde et le Pompe est changé après chaque tir. Pour chaque délai, l'ensemble des images permettant la caractérisation du plasma (voir Fig.4.10-p.48) est enregistré. Cet ensemble comprend un interférogramme de référence avant le tir du *pompe*, l'interférogramme pendant l'expansion du plasma, à un retard donné et une image d'ombroscopie après le tir, afin de visualiser la position du trou crée. Les interférogrammes sont ensuite nettoyés numériquement et analysés selon la procédure décrite auparavant (pour la procédure complète, voir annexe B). Les cartes de phase et de densité électronique sont ainsi produites. La mesure du profil de densité est répétée à des intervalles réguliers séparés de $3ps$, produisant ainsi une carte complète de l'évolution lors des premières $100ps$ d'expansion (Fig.4.12-p.50).

9.1.3 Comparaison avec les simulations

L'interaction entre l'impulsion femtoseconde et la cible solide, ainsi que l'expansion du plasma, sont simulées avec l'aide d'un code hydrodynamique lagrangien $1D\,^1/_2$, CHIVAS, qui simule l'interaction en régime femtoseconde avec un plasma surdense.

La comparaison entre la vitesse d'expansion du front plasma mesurée et simulée par le code hydrodynamique (Fig.4.15-p.55) permet de valider la modélisation utilisée dans le code pour le cas expérimental présenté. La validation des simulations autorise l'utilisation des profils de densité simulés afin de prédire la propagation dans le temps du pic de surdensité (onde de choc) traversant les parties non perturbées de la cible (Fig.4.14-p.55). Les résultats finaux de l'expérience sont résumés dans la figure Fig.4.16-p.56; à gauche est montrée l'évolution des longueurs de gradient plasma et des positions

de la surface à la densité critique; à droite est montrée l'évolution du choc dans la cible.

9.2 Étude du débouché de l'onde de choc par variation de réflectivité

Les résultats précédemment obtenus relatifs à l'expansion de la plume plasma créée par le laser permettent de connaître l'évolution des longueurs de gradient créés en face avant de la cible. Afin de valider expérimentalement la loi de propagation de l'onde du choc, une expérience de contrôle de la surface non illuminée d'une cible mince a été réalisée.

Les simulations montrent que l'onde du choc qui se propage à travers la partie non perturbée de la cible est le mécanisme dominant le plus rapide parmi ceux qui sont produits suite au dépôt de l'énergie laser. Pour cette raison la surpression qui représente le précurseur de cette onde va être utilisée comme temps limite à partir duquel la surface non illuminée sera considérée perturbée. Le principe de l'expérience repose sur le fait que la présence d'un plasma à la surface d'une cible change sa réflectivité. En mesurant ainsi le changement de valeur de l'intensité d'un faisceau laser sonde qui se réfléchit sur la surface arrière il est possible, non seulement de connaître le temps de débouché de choc mais aussi la température électronique de face arrière.

9.2.1 Mesure optique de température électronique

D'après les simulations hydrodynamiques le précurseur de la perturbation (Fig.5.1-p.60) produit des températures électroniques de l'ordre de l'électron-volt.

En appliquant le modèle de Drude, la constante diélectrique d'un métal, donc sa réflectivité, dépend directement de sa fréquence de collision électron-ion (eq:5.3-p.61). Celle-ci est modélisée par l'interpolation d'Eidmann-Hüller (eq:5.8-p.62) pour des températures intermédiaires entre celles d'applicabilité de la formule de Spitzer[1] et la fréquence de collision électron-phonon[2]. En couplant les deux relations on peut reconstruire la température électronique du matériel à partir d'une seule mesure de réflectivité. La géométrie utilisée pour la mesure est schématisée dans Fig.5.2-p.60.

[1] La formule de Spitzer (eq:5.4-p.61) est une modélisation de la fréquence des collisions électron-ion dans le cas de plasma chaud.

[2] Les collisions entre électrons et phonons représentent le phénomène le plus important à faible températures électroniques.

9.2.2 Réalisation expérimentale

Le plasma est crée sur la surface des cibles minces en aluminium par une impulsion laser de $\tau = 150fs$ à une intensité sur cible de $10^{15}W/cm^2$. Les épaisseurs utilisées sont $3\mu m$, $2\mu m$ et $800\mu m$. L'impulsion *sonde* est produite par la même chaîne, et a par conséquent les mêmes paramètres que l'impulsion utilisée pour l'expérience d'interférométrie ($E_L < 10mJ$, $\tau \approx 400fs$, $\lambda = 400nm$). Ce faisceau *sonde* est incident à 45 degrés de la surface arrière de la cible, et donc de l'axe de propagation de l'onde de choc (voir géométrie Fig.5.4-p.64 et Fig.5.6-p.66). Le faisceau *sonde* est préalablement synchronisé au faisceau *pompe*, permettant de mesurer la réflectivité du matériel à différents instants après le début de l'interaction.

9.2.3 Résultats Expérimentaux

Les cibles utilisées n'ont pas de qualité optique, ce qui produit un champ de speckles sur les images. Deux stratégies sont utilisées pour analyser les images. Premièrement on enregistre une image de référence et une image avec impact laser, ensuite nous calculons pour chaque pixel le rapport d'intensité. L'image de référence est celle de la cible juste avant avoir été irradiée par le faisceau *pompe* (Fig.5.8-p.68). Les images ainsi obtenues montrent les cartes $R(x, y)$ de réflectivité autour de l'axe de propagation du choc. En augmentant le retard entre les deux faisceaux, trois types de cartes sont observés (Fig.5.9-p.70):

a. Aucune perturbation n'est visible le long de l'axe du faisceau *pompe*;

b. Une déformation est visible, mais la courbe montre qu'aucune absorption d'énergie n'est mesurée (i.e. l'intégral de la courbe n'est pas perturbé);

c. Une partie absorbante ($R < 1$) apparaît.

Un deuxième type d'analyse (quantitative) a été réalisé en intégrant l'énergie sur la même zone des images référence et tir. Pour chaque retard, la réflectivité moyenne est obtenue par le rapport entre ces deux quantités. (Fig.5.12-p.73-*haut*). La correspondance entre la réflectivité R ainsi mesurée et la température électronique $T_e(t)$ (Fig.5.12-p.73-*bas*) est finalement obtenue en inversant numériquement la courbe du modèle d'Eidmann - Hüller[3].

[3]La courbe montrée est calculée dans l'hypothèse d'équilibre thermique entre les populations électronique et ionique, $T_e = T_i$.

L'échelle temporelle de la propagation du choc traversant la cible se déduit des temps de débouché en fonction de son épaisseur. La comparaison entre les résultats expérimentaux[4] et la simulation hydrodynamique de la propagation du choc est résumée dans Fig.5.13-p.74. Deux typologies de débouché sont ici considérées:

Points jaunes: ils définissent le moment à partir duquel une discontinuité est observée sur la carte de réflectivité: cet événement est associé à une déformation de la surface réfléchissante.

Points rouges: ils définissent le moment où la courbe de la réflectivité intégrée (Fig.5.12-p.73-*bas*) numériquement tombe en dessous du seuil de $R = 0.8$.

La comparaison montre une confirmation partielle des simulations; la dynamique observée expérimentalement souligne la nécessité d'expériences complémentaires. Néanmoins les données obtenues donnent une mesure précise du temps de propagation de l'onde du choc.

9.3 Conclusion

Ces deux expériences ont permis une meilleure compréhension des phénomènes se déroulant lors de l'interaction entre une impulsion laser ultra-brève à intensité moyenne et une cible surdense. Ces résultats peuvent maintenant être appliqués au cas expérimental du piédestal d'une impulsion laser ou d'une pré-impulsion chauffant la cible avant l'arrivée de l'impulsion principale à ultra-haute intensité. En particulier l'étude de l'évolution de la longueur du gradient plasma permet de reconstruire à tout moment l'état de surface de la cible. La mesure du temps de propagation de l'onde de choc créée par une impulsion courte et sa confrontation avec les temps issus de codes hydrodynamiques permettent de mieux définir les paramètres de cibles autorisées pour des expériences d'accélération ionique. Cette étude permet ainsi de définir deux grandeurs cruciales pour l'accélération ionique. D'une part la longueur de gradient des plasmas de face avant, sièges des mécanismes d'absorption de l'énergie du laser et de sa conversion en électrons supra-thermiques, et d'autre part les épaisseurs de cible, pour un retard pompe-sonde donné, autorisées, i.e. pour lesquelles aucune détente en face arrière ne survient pendant le processus d'accélération ionique (détentes dont les conséquences nuisent à l'obtention de champs électriques ultra intenses).

[4] L'analyse donne des résultats consistants pour des épaisseurs de $3\mu m$ et $2\mu m$.

Chapter 10

Expériences de génération de faisceaux énergétiques de protons par laser

Les expériences d'accélération d'ions et de protons par laser ont été menées sur l'installation laser de la "*Salle Jaune*" du *Laboratoire d'Optique Appliquée*. Cette chaîne utilise la technique CPA (amplification à dérive de fréquence) pour atteindre des puissances de plusieurs dizaines de terawatts. Le système laser (Fig.6.1-p.78) est composé par *(i)* un oscillateur Titane:Saphir, *(ii)* un étireur, *(iii)* trois étages d'amplification et *(iv)* un compresseur à réseaux. Le système complet fournit des impulsions de durée $\tau = 30fs$ et d'énergie $E_L \approx 800mJ$, avec un taux de répétition égal à $10Hz$.

Au cours des deux dernières années le système XPW (génération d'onde à polarisation croisée, voir section 6.1.1-p.79) a permis d'améliorer le contraste et d'atteindre des valeurs proches de 10^{10} sur une échelle de quelques *nanosecondes* avant l'impulsion principale (i.e. fs) (Fig.6.3-p.82). Ce résultat est obtenu grâce à un effet dégénéré non linéaire du troisième ordre, qui produit une onde à polarisation différente selon l'intensité d'entrée de l'onde laser.

10.1 Réalisation des expériences

La structure de base de l'installation expérimentale (Fig.6.6-p.86) comprend *(i)* les optiques de transport et de focalisation du faisceau laser à ultra haute puissance, *(ii)* les

systèmes de positionnement et de contrôle des cibles minces et *(iii)* l'ensemble des diagnostiques pour la détection et la caractérisation des espèces ioniques accélérées.

L'impulsion femtoseconde est focalisée par une parabole hors axe à $f/3$ d'ouverture. La tache focale ainsi obtenue (Fig.6.7-p.88) présente un *waist* de l'ordre de $2-3\mu m$; en prenant en considération les pertes introduites par le transport du faisceau pompe, l'impulsion laser incidente sur cible contient un total de $E_L \approx 300mJ$, ce qui correspond à une intensité crête de $I_0 \approx 4 \times 10^{19} W/cm^2$.

10.1.1 Détection des faisceaux ioniques

La détection des faisceaux ioniques produits par interaction laser matière est rendu difficile par la faiblesse des énergies et la variété des espèces présentes. Au cours des expériences précédentes, la détection était entièrement basée sur les intégrateurs de dose CR39, utilisés dans la plus grande partie des laboratoires et bien connus par la communauté des scientifiques qui travaillent sur le sujet. Étant données ses limitations et le temps nécessaire à son utilisation[1] des nouveaux diagnostiques ont été mis à point.
Dans le montage expérimental réalisé, les mesures spectrales ainsi que la distinction entre les différentes espèces ioniques sont obtenues par une *galette à micro-canaux* (MCP) couplée à une *parabole Thomson* (TP, Fig.6.13-p.98).

Une parabole Thomson est l'ensemble de deux électrodes et deux aimants permanents, ajustés de façon à produire des champs électrique et magnétique parallèles. De la sorte les particules chargées qui se propagent à travers la région où les champs sont actifs (voir équations (6.4) et figure Fig.6.12-p.97) sont séparées selon leur énergie, et leur rapport charge/masse.

Une *galette à micro-canaux* (Fig.6.10-p.94) consiste en une matrice de capillaires micrométriques dans une galette en verre. Les capillaires ont leur axe orienté de quelque dégrée par rapport à la normale à la surface de la galette elle même. Pendant son utilisation un champ électrique de quelque kV est appliqué entre les deux surfaces: le dépôt de dose sur la première surface produit des électrons qui sont ensuite accélérés vers la paroi d'un capillaire: chacun des impacts est capable d'extraire des électrons

[1] Le CR39 est sensible à la dose ionique déposée et il ne peut pas facilement distinguer ni les énergies ni les espèces; chaque détecteur qui se présente sous forme de feuille, doit être enlevé après l'exposition au rayonnement et développé ensuite, afin d'en sortir l'information expérimentale.

secondaires, accélérés à leur tour. L'effet d'ensemble est celui d'amplifier la distribution spatial de dose incidente sur la surface irradiée en produisant un effet d'avalanche vers l'autre surface. La vague d'électrons ainsi produite est transportée et révélée par son impact sur un milieu scintillateur; dont l'image est enregistrée sur une caméra CCD procurant ainsi la distribution spatiale des ions à la sortie de la parabole de Thomson (Fig.6.15-p.100).

L'ensemble des deux systèmes constitue un dispositif qui ne nécessite pas de manipulation pendant son fonctionnement et qui délivre le spectre complet de toutes les espèces ioniques présentes en temps réel. Après sa validation par comparaison avec un ensemble de mesures obtenues avec du CR39, l'utilisation du système TP+MCP dans l'expérience d'accélération des ions par laser a représenté une véritable amélioration de notre protocole expérimental.

10.2 Résultats expérimentaux

10.2.1 Validation des paramètres et des diagnostiques

Les paramètres laser sont validés expérimentalement pendant la première partie de l'expérience. Cela est surtout vrai pour le niveau de contraste, tant qu'une mesure de grande dynamique du piédestal sur une échelle temporelle inférieure au $500ps$ n'était pas fiable. La bonne qualité du contraste est confirmée en réduisant l'épaisseur des cibles et en regardant la corrélation entre la position de focalisation (c'est à dire la taille de la tache, donc l'intensité crête) et l'énergie maximale des protons (voir Fig.7.4-p.112 et Fig.7.5-p.112).

10.2.2 Accélération des protons dans un régime de haut contraste

L'amélioration du contraste, qui permet l'interaction à haute intensité avec une cible mince dont la face arrière est peu ou prou perturbée, ouvre accès à des configurations expérimentales qui devraient produire des faisceaux de protons encore plus énergétiques. Ce résultat est schématisé dans la Fig.7.12-p.123, où les symboles rouges représentent les énergies obtenues à haut contraste et les verts sont ceux obtenues à bas (10^6) contraste.

La corrélation entre intensité crête et énergie proton est étudiée selon deux parcours: *(i)* variation de la durée et *(ii)* variation de l'énergie de l'impulsion.

Dans le premier cas, l'étirement de l'impulsion provoque une baisse de son intensité crête (selon l'équation 2.4-p.12). Les résultats expérimentaux (Fig.7.10-p.120-*bas*) pour deux épaisseurs de test de $15\mu m$ et $1.5\mu m$ montrent un comportement qualitativement différent. En utilisant des cibles plus minces, l'énergie maximale des protons n'est sensible qu'à l'intensité crête; alors que dans le cas des cibles plus épaisses une durée optimale est trouvée. L'effet observé ne semble point être explicable par le mécanisme physique dit de « récirculation électronique », il indique plutôt une dépendance entre le couplage laser-plasma en énergie et la durée des mécanismes de chauffage. Ce type d'effet ne peut être observé qu'en utilisant des impulsions à hauts contrastes, pour lesquelles la faible intensité du piédestal rend négligeable la présence du pré-plasma sur la surface de la cible avant l'interaction principale. Une étude plus approfondie serait néanmoins nécessaire afin de comprendre la corrélation entre la durée idéale de l'impulsion laser et l'épaisseur de cible.

Dans le deuxième cas, l'énergie laser est changée grâce à des filtres neutres qui sont insérés sur le trajet du faisceau avant compression. Les résultats présentés (Fig.7.10-p.120-*haut*) montrent l'énergie maximale des protons pour quatre énergies différentes et sur quatre épaisseurs ($15\mu m$, $8\mu m$, $1.5\mu m$ et $400nm$). Les traces noires (superposées aux points expérimentaux dans la même figure) montrent l'interpolation des données avec deux courbes analytiquement différentes. De la même façon que dans le cas précédent, les cibles les plus épaisses ont un comportement différent par rapport aux plus fines. Pour les cibles de $15\mu m$ et de $8\mu m$ le comportement est mieux représenté par une fonction du type $E_p \propto \log(I_0)$; alors que pour les épaisseurs de $1.5\mu m$ et de $400nm$ le comportement correspond plutôt à celui de $E_p \propto \sqrt{I_0}$.

Les figures Fig.7.11-p.122 *haut* et *bas* montrent l'énergie maximale des protons pour différentes énergie et durée de l'impulsion, en fonction de l'intensité crête. Les deux figures illustrent clairement un comportement différent.

10.3 Conclusions

Les résultats présentés dans ce chapitre montrent la première application du nettoyage de contraste par XPW à l'accélération de proton par laser. Les courbes expérimentales confirment les comportements prévus dans la littérature et montrent la corrélation en-

tre les paramètre de cible et de faisceau. Cette amélioration du contraste, qui permet d'une part d'obtenir des spectres ioniques très reproductibles, permet aussi d'avoir des conditions d'interaction beaucoup mieux contrôlées. Elle rend enfin possible une étude extrêmement plus pointue sur le rôle que jouent les différents paramètres pour l'accélération ionique. La figure Fig.7.13-p.124 montre l'énergie maximale des protons obtenue lors de huit tirs dans les mêmes conditions laser. Elle illustre parfaitement l'amélioration de la stabilité des faisceaux de protons qui résulte du contrôle temporel de l'énergie laser.

Chapter 11

Conclusions

Ce manuscrit de thèse rapporte les résultats de près de trois années d'activités expérimentales dans le domaine de l'interaction laser matière dans le régime classique et relativiste, et dont la finalité est le développement de la technique d'accélération compacte en milieu plasma d'ions énergétiques. La qualité, la reproductibilité et la fiabilité des faisceaux de particules produits par laser n'ont pas cessé de s'améliorer, au fur et à mesure des développements des technologies laser. Néanmoins certains mécanismes physiques qui rentrent en jeu dans ce processus d'accélération ne sont toujours pas complètement expliqués. En bref:

- L'énergie totale et la distribution temporelle de l'intensité de l'impulsion laser agissent sur l'état de la cible (soit en surface, soit en profondeur). Ces conditions initiales, imposées par le piédestal gouvernent les mécanismes de couplage de l'énergie du laser en énergie cinétique. Différents comportements collectives sont responsables du transfert d'énergie de l'onde à la composante électronique du plasma; les simulations indiquent que la présence d'un gradient plasma est bénéfique à l'absorption. Néanmoins il n'existe pas de modèle complet qui puisse prédire soit l'évolution de l'interaction soit le spectre électronique à la fin de l'impulsion laser.

- Si le laser se propage avec un angle par rapport à la normale à la cible, il existe une corrélation entre les paramètres du pré-plasma et *(i)* la direction et *(ii)* la divergence de la population d'électrons chauds qui est responsable de la création du champ accélérateur sur la surface arrière.

- La propagation d'une onde de choc traversant la cible peut entrainer de changement sur la surface arrière; notamment la présence d'un gradient de densité sur

cette surface responsable de la diminution du champ accélérateur TNSA.

Les paramètres du piédestal d'une impulsion laser ultra courte sont les plus difficiles à contrôler. L'intérêt d'utiliser des sources laser à ultra-haut contraste réside dans la possibilité de réduire voir d'éliminer certaines incertitudes dans le processus d'interaction. Les activités expérimentales ici présentées ont eu pour but l'étude de l'accélération des particules avec un laser où le contraste est amélioré avec la technique XPW. Cette technique et son intégration sur une chaîne CPA à plusieurs terawatts ont permis d'obtenir des conditions d'interaction meilleures et plus contrôlables. À partir de résultats expérimentaux (voir Fig.7.9-p.116), on peut estimer la durée du piédestal devant l'impulsion laser de la Salle Jaune $100ps < \tau_{ASE} < 400ps$. Celle-ci nous fournit des paramètres de travail différents du cas à ultra-haut contraste (par exemple voir Fig.7.12-p.123) et qui ouvrent des conditions expérimentales inexplorées.

La première partie des activités expérimentales a été concentrée sur l'étude de l'interaction entre des impulsions à intensité moyenne (et une énergie comparable a celle d'un piédestal) et des cibles d'aluminium. Les mesures interférométriques ont permis la reconstruction des premiers instants d'expansion du plasma, alors que celle de réflectométrie en ont mesurées les effets sur la surface arrière. En particulier la loi temporelle de propagation du choc, qui est déduite des simulations, n'est pas complètement confirmée par les observations expérimentales sur les cibles les plus minces. Cela peut indiquer qu'une meilleure connaissance de la structure réelle des cible minces est envisageable. Dans la deuxième partie de la thèse, une impulsion laser XPW est utilisée pour l'accélération des ions sur des cibles minces. Les paramètres du laser et des cibles sont variés afin de mettre en évidence la dépendance entre l'énergie maximale des protons et la condition expérimentale. En conclusion:

- Une épaisseur optimale est déterminée pour l'accélération des ions dans nos conditions expérimentales.
- Suite à la variation, à énergie constante, de la durée d'impulsion, des comportements différents sont observés avec des cibles épaisses ($15\mu m$) et minces ($1.5\mu m$, $3\mu m$). En particulier, la variation de l'énergie maximale des protons en fonction de la durée de l'impulsion laser présente un optimum pour des cibles épaisses, et décroît de façon monotone pour des cibles minces.

Les résultats expérimentaux mettent en évidence certains points qui ne sont pas complètement compris.

- On a observé une différence entre l'échelle temporelle des perturbations induits par choc entre [49] et l'expérience de réflectométrie.
- L'épaisseur optimale déterminée expérimentalement est située autour de $d = 2\mu m$. La dépendance observée entre l'énergie maximale et l'épaisseur, pour $d < 2\mu m$ est plus faible qu'attendue. Dans l'hypothèse que la diminution d'énergie des protons est due à la perturbation de la surface arrière des cibles plus minces que l'idéal, la faible dépendance observée suggère que d'autres paramètres du piédestal entrent en jeu.
- La présence d'une durée optimale de l'impulsion pendant l'accélération avec une cible épaisse est controversée. L'hypothèse la plus probable est qu'une impulsion plus longue puisse chauffer de façon plus lente et efficace la surface d'une cible.

Ces résultats suggèrent des effets encore plus fins, qui font, en ce moment, l'objet des campagnes expérimentales à venir.

Les études préparatoires sur la formation du pre-plasma et sur l'échelle temporelle de la propagation du choc motivent l'utilisation d'une impulsion à haut contraste pour l'accélération des protons à deux faisceaux. Dans ce contexte, une impulsion laser, à intensité moyenne, est utilisée pour préparer la surface de la cible à l'interaction avec l'impulsion laser d'ultra-haute intensité. À cause de contraintes techniques, je n'ai pu que réaliser cette expérience dans une configuration préliminaire. Elle a mis en évidence certaines difficultés techniques et n'a pas pu produire un ensemble complet de données expérimentales. Néanmoins l'expérience (voir annexe A) a confirmée l'existence d'une longueur de plasma optimale pour le couplage laser-matière dans le cadre de l'accélération des protons par laser.

Part V

Conclusions and Perspectives

Conclusions

This thesis is the report of approximately three years of experimental work in the domain of laser-matter interaction to study the production of energetic proton beams.

The laser acceleration of proton beams from solid targets has received a great and increasing interest in the past years. The ion beams accelerated by laser have been increasing in quality, in energy and in repeatability as laser technology keeps improving. Still some of the physical mechanisms that are involved in the processus remain unclear. The presence of the pedestal before the high peak laser pulse introduces many unknowns in the accelerating conditions that are created on the front and on the rear surface of the target. Briefly:

- The total contained energy and its distribution (i.e. the flux profile) in the laser pedestal affect the surface of the target. They define the shape and the extension of the plasma gradient on the illuminated surface, hence the state of the matter the laser peak interacts with. Several collective mechanisms are recognised where a net energy transfer between the laser light and the electron component happens, and simulations indicate that the presence of a plasma density gradient can be beneficial to the laser energy absorption. Nevertheless the overall behaviour is not easily modelled. In the same way, no model exists to tell the electron spectrum after the interaction has happened.

- When the laser is impinging with an angle to the target normal, a correlation exists between the preplasma characteristics and *(i)* the direction *(ii)* the divergence of the hot electron population which is responsible for the accelerating field on the rear surface.

- The propagation of the compressional shock through the target bulk affects the rear surface, where the charge separation produces the TNSA acceleration effect. The

correlation between the ASE duration and the variation of the ion cutoff energy have been experimentally observed and understood; besides of that the presence of a plasma on the accelerating surface is recognised responsible of voiding the TNSA mechanism.

The features of the pulse pedestals are among the parameters of most difficult control on a laser system. The interest of having laser sources of enhanced contrast relies in the elimination or reduction of the uncertainties in the interaction process. The experimental activities during my thesis aim to characterize the use of a XPW-enhanced laser pulse. The XPW technique and its integration on a large CPA installation proved to be still in a premature state but to provide more controllable conditions.

From the experimental results, I estimate the duration of the pedestal part that is effective in the interaction to be $100ps < \tau_{ASE} < 400ps$ (see 7.4.1). This makes our experimental case different from the "ultra-high" contrast that is obtained with double plasma mirrors (see Fig.7.12).

The first part of the experimental activities is focused to a better comprehension and the experimental validation of the interaction of a "pedestal-like", moderate intensity, laser pulse on Aluminum targets. The developed interferometric technique proved to be reliable and produced a complete set of maps of the early stages of the plasma expansion. The reflectometry experiment stresses the importance of the quality of the metallic targets and underlines some obscure points on the behaviour of the rear surface of the illuminated foil. In particular:

- The temporal law that is inferred from simulations for the propagation of shocks is not completely validated for thinner targets. This fact indicates that it is necessary a better characterization of the target bulk to be able to extend the scaling laws to thinner foils.

- The reflectometry measurements on the thicker targets are significantly different from what is foreseen by the simulations about the timescale of the shock breakout. This deviation motivates deeper studies.

In the second part, the XPW laser pulse is used in ion acceleration from thin metal foils. The laser and target parameters are varied to put in evidence the dependence of the ion beam to the experimental condition. In conclusion I can say that

- During the variation of the target thickness, an optimum is put in evidence.
- The correlation between the laser pulse duration and the proton cutoff energy is qualitatively different between thicker ($15\mu m$) and thinner ($1.5\mu m$, $3\mu m$) targets. For the first, an optimal pulse duration exists while for the seconds, no variation is found – in the searched space– from the monotonic decreasing of the cutoff energy with the peak intensity.

The experimental results put however in evidence some points that are not completely understood.

- There is a substantial difference in the timescale of perturbation between [49] and the reflectometry experiment. This might indicate that the ASE pedestal is active not only on a duration basis.
- The cutoff energy for targets that are thinner than the optimal ($d < 2\mu m$) shows a loosely bound dependence on the target thickness. If we accept that the optimal is defined by the limit of perturbation on the rear face, we must conclude that the detrimental effect on that face is slower, in our experimental case, than what is commonly known in literature. This might corroborate the hypothesis of other correlations to the pedestal characteristics (eg. its total energy content).
- The presence of an optimal pulse duration for acceleration on thick targets, while normally explained by electron recirculation, is controversial. The stretched pulse contains the same energy of the compressed one, although longer tails precede it, which might result in a slower and more effective heating of the target.

The preparatory studies, on preplasma formation and on shock timescale measurement, motivate the use of a high contrast laser pulse for a two beam proton acceleration approach, the first preheating and producing the ideal plasma condition for the second to heat electrons. Due to time constraints, I performed this experiment in a preliminary configuration, which underlined some technical issues, did not produce a complete and self-consistent set of data, but, nevertheless, confirmed the existence of an optimum plasma scale length for laser-target coupling. The setup and the preliminary analysis of the results are presented in App.A.

Perspectives

The experimental results that are presented in this manuscript report of the creation of energetic ion beams from the interaction between an UHI laser pulse at high contrast and an overdense target. This is the first report of the use of XPW technique to enhance the contrat ratio for this kind of experiments. The ion beams produced during the experimental campaign proved to be stable and repeatable. The peculiarities of laser accelerated ion beams (the brilliance, the duration, the emittance) in conjuction with the practical realizability (there is no need of radioprotected areas for the entire laser installation) explains the interest and suggests the future feasability of laser-produced beams in many fields of industry, research and medicine. In the past years, the evolution of the laser-ion acceleration has been evolving following step by step the improvements that were introduced in the laser technology. Soon the PetaWatt class laser systems will make possible the increase in ion energy that is, for the moment, one real limitation to a practical use of the accelerated beams.

Nevertheless many limits in the experimental realization and in the modelling of the phenomena are underlined. The improvement in the stability and the repeatability of the acceleration process follows the introduction of the XPW on the laser chain; this fact stresses the importance of the precise control and knowledge of the parameters to understand how the acceleration process can be optimized. The basic idea for future experiment on solid target, should be based on a two beams laser-target interaction while optical diagnostics are put in place to directly monitor the two surfaces of the target.

The careful discrimination among the processes that bring to the electron heating and the experimental measure of the electron spectra in correlation with the preplasma conditions might bring to *(i)* a precise modelling of the interaction with solid targets and

(ii) the research of an optimal plasma gradient shape. A possible investigation is to probe the created plasma just before the main peak interacts with it; this task could be accomplished by interferometry or by radiography in the X range.

The effects of the laser pedestal on the rear face conditions are a field of great interest. Our experiment showed that more parameters than the simple duration of the ASE enters in the interaction between the rear surface condition and the TNSA acceleration process. A more precise definition is needed of the boundaries of the induced perturbation (timescale, initial temperature, surface deformation) on the non illuminated surface and their correlation with the TNSA efficacity and the ASE parameters. From a numerical analysis of the experimental data of the reflectometry experiment (Ch.5) one should be able to rebuild the surface deformation from the distortion that is produced in the speckle field. A future experiment with a two beam reflectometry will also enable to extend the searched timescale to the times where a plasma gradient exists on it.

The new improvements in laser technologies are pushing further the pulse energies. At PetaWatt levels, the technology for contrast improvement will face new challenges, as the required contrast levels will increase accordingly.

At the same time, many groups in the world are working on the production of materials specifically conceived for laser-ion acceleration, to enhance the acceleration of certain species or to emit collimated beams. A major breakthrough might be represented, in coming years, by the plasma micro-machining technique in laser-underdense interaction. Here a tunable plasma structure is created in a gas jet by a first laser. Ideal structures for ion acceleration could be produced in this way.
For what concerns the used diagnostics, the use of real time systems, like the TP+MCP spectrometer proves to be a milestone in laser-plasma ion acceleration. The benefit of direct experimental feedback let the user to define the interaction parameters in a faster and safer way; the measure of all the ion species at the same time produces a more precise picture of the experimental event. The main limitation in our experiment is represented by the small integration angle of the spectrometer; this makes it of critical use in condition where any doubt exist on the direction of the accelerated beam and its spatial movements. This might be the case when multiple laser beams are used at the same time on the target surface, varying the direction of the plasma gradient and pos-

sibly producing deformations on the rear surface. A complete diagnostic system should include, aside of the high resolution MCP spectrometer, a general purpose diagnostic, like for example a wide scintillator, or a multi-sector Faraday cage, to be able to monitor, at the same time, any lateral movement. In parallel, an electron spectrometer can be useful to correlate the electron spectrum to the ion beam.

For medical applications, one should consider the production of proton (ion) beams with a higher efficiency and a quasi-monoenergetic energy distribution. Among the various directions, *(i)* the use of structured dots and *(ii)* the use of circularly polarized laser beam are promising techniques and need further investigation. Structured dots and volume-limited targets are conceived to limitate the current spread in areas that are not directly interested by the acceleration process; a circularly polarized beam is expected to reduce the volumetric (electron) heating of the target that is responsible for the TNSA acceleration. In this case the interaction of intensities in the order of $10^{18} - 10^{20} W/cm^2$ on very thin targets would results in the production of monoenergetic ion beams by direct momentum transfer from the incoming photons to the ions at rest (radiation pressure acceleration, [59, 58]).

The completion of ongoing international projects like HiPER or ELI, for which powers of $10PW$ to $100PW$ are planned at full specifications, will open a new interaction regime, where also ions will experience relativistic motion in the laser field. This subject has started to be investigated and is expected to produce new and exciting results in a near future.

Part VI

Appendices

Appendix A

Two beams proton acceleration

In chapters Ch.6 and Ch.7 I presented the experimental setup and the results that are obtained for laser ion acceleration. The experimental measurements in section 7.4 show the the dependence of the proton signal on some laser and target parameters when a laser pulse with improved contrast is used. The use of high contrast beams enables the use of thinner targets which in turns increases the proton cutoff energy. Nevertheless the reduced presence of a plasma in front of the illuminated surface is known to reduce the absortpion of the laser energy. The beneficial effect of a certain plasma gradient length in front of the target surface is underlined in simulations [4] and in experimental works [92].

In this appendix I show the use of a moderate intensity beam to produce a plasma gradient on the illuminated surface of a metallic target before the arrival of the main UHI peak. The results from the two preparatory experiments described in Ch.5 and Ch.4 are used to *(i)* define the maximum allowable time delay between the heating pulse and the pump pulse and *(ii)* correlate this delay to the obtained gradient length. The measurements are produced on the installation that is summarized in Fig.6.6 and are taken in the last part of the *Salle Jaune* campaign (April 2008, Ch.6).

A.1 Two beams setup

For the two beams experiment a second beam is taken from the laser source. The beam is derived by a 10% reflecting blade on the main beam-line, before compression, and sent to a separate compressor. In our experimental condition, a total of $\approx 180mJ$ is available on this beam. The beam is attenuated by a $OD = 0.3$ neutral density before compression. The final energy that is transported to the chamber, including compressor

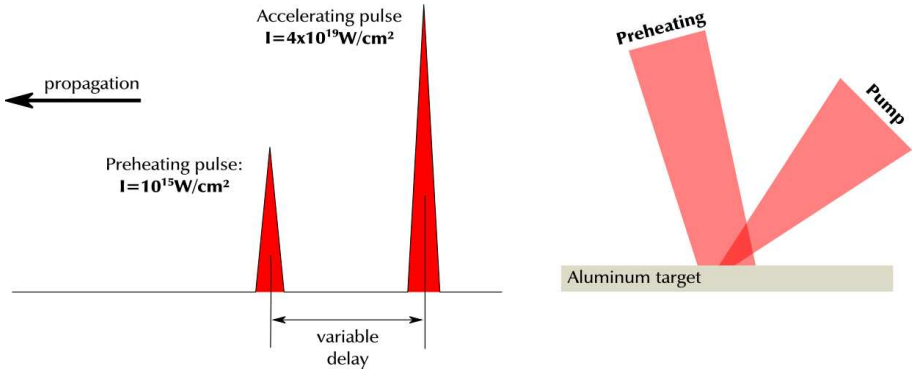


Figure A.1: Principle of the two beams acceleration. A moderate intensity femtosecond pulse is sent before the main, ultra-high intensity peak *(left)*. The two are superposed on a metallic target: the less intense is focused less tightly to produce a plasma expansion; the most intense is shot through the created plasma *(right)*.

and transport losses, results to be $\approx 30mJ$.
This pre-heating beam (Fig.A.1) is sent to a delay line (Fig.6.6) and then focused by a $f = 50cm$ lens onto the target surface.

Beam Alignment in focus

The calculated spot size in the waist is $2w_0 = 12\mu m$ and the Rayleigh range $z_0 = 170\mu m$. This estimation doesn't take in account the fact that no phase front correction exists on this beam, which is known to reduce its focusability. No direct measurement on the point of focus of the lens could be put in place. The positioning of the lens is corrected by a micrometric translation using as a feedback the damage threshold on the thick aluminum target holder aligned in the pump beam focus. When the heating beam is strongly attenuated, the flash on the aluminum surface is observed in a range on $\approx 1.5mm$. From values of z_0 and w_0 we estimate the spot on target to be $2w < 50\mu m$ which results in a peak intensity $I_{pre-heat} > 9 \times 10^{16} W/cm^2$. The total energy per surface flux is $F > 15\mu J/\mu m^2$ which is comparable to the experimental condition in the *Salle Verte* preparatory experiment (see section 4.1.1).

Spatial superposition of the beams

The pre-heating beam is superposed to the pump beam by acting on the motorized mirror that is situated after the focusing lens. The superposition condition is checked by looking at the craters that are formed by the two strongly attenuated beams on a

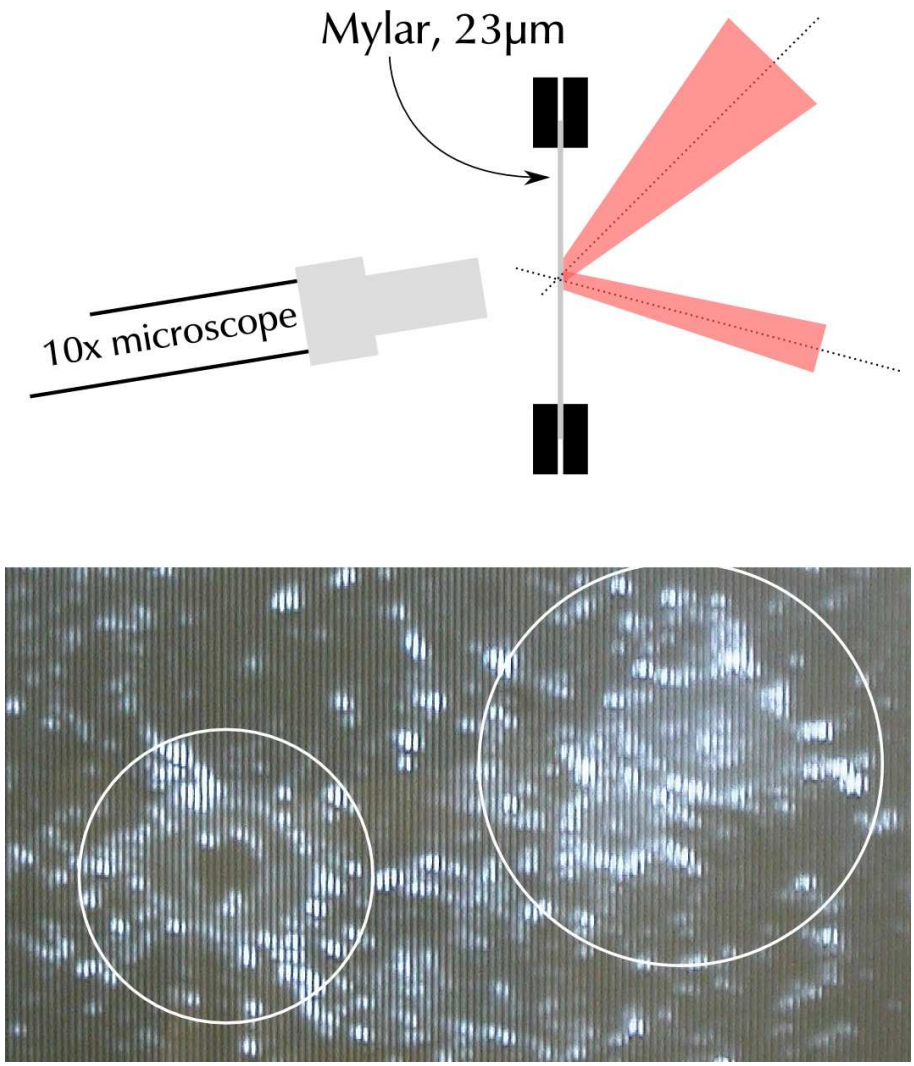


Figure A.2: Principle for the superposition of the two beams. *(Upper)* A microscope objective is used to image in transmission a thin mylar foil, where craters are created by the two beams. The spot of the heating beam (the lowest one in the figure) can be moved by a motorized mirror. *(Lower)* Real time image (200×) of the mylar foil: two separated craters are visible on the right, while, on the left, the two superpose on a single circular structure.

thin mylar foil (Fig.A.2). The foil is illuminated in white light from one side and imaged in transparency by a microscope on the other side (Fig.6.6-9).

During the experimental procedure we noticed the superposition to be sensitive on *(i)* the position of the delay line and *(ii)* the coupled drift of the two laser beam. This last

proved to be very difficult to control; in fact the two beams, the pre-heating and the pump, follow very different geometric path and undergo a different number of reflections (even and odd), so that a drift of the beam in the CPA chain results in the two spots drifting in opposite directions. This fact required a continuous checking and correction of the superposition, which sensibly slowed the experimental procedure.

Synchronization

The two pulses are synchronized by checking the interference condition. The two beams are superposed by a thin ($150\mu m$) glass blade mounted on the target holder, in a way that the pre-heating beam is reflected on the continuation of the pump beam propagation direction.

A.2 Experimental Results

The delay line is varied between $0ps$ and $100ps$ and the proton cutoff energy is recorded. In Fig.A.3 is shown the dependence beteen the proton energy and the delay time; each experimental point represents the average of three to four separate shots. The gray line

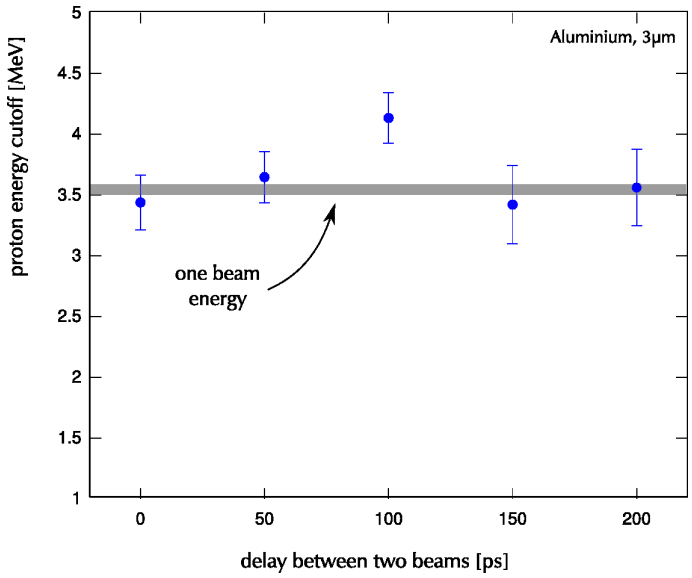


Figure A.3: Proton cutoff energies from a two beam ion acceleration experiment with a $3\mu m$ thick aluminum target. The grey line represents the energy cutoff that is obtained in the same conditions with a single beam (the width of the line represents the error).

represents the energy that is normally obtained in the case of a single beam.

A.3 Discussion and Conclusion

The presence of a plasma gradient on the illuminated surface if found to affect the cutoff energy of the accelerated proton beam; a peak is found for a delay between the two pulses of $\Delta t = 100ps$. This delay corresponds, from the simulations presented in Ch.4, to a plasma gradient of $L_{grad} = 3.5\mu m$. In the searched timescale, no detrimental effects are observed. The preliminar study for the shock breakout timescale (reflectometry, Fig.5.13) puts a limit at a delay $200ps < \Delta t < 400ps$ before a perturbation of the rear surface could be produced on a $3\mu m$ target. From the theoretical introduction that is presented in section 3.3 we believe the increase to be a consequence of an optimal equilibrium between the different phenomena that regulate the energy transfer from the laser pulse to the electron component in the plasma. This hypotesis is supported by PIC simulations shown in [80]. To our knowledge, this is the first time this experiment is

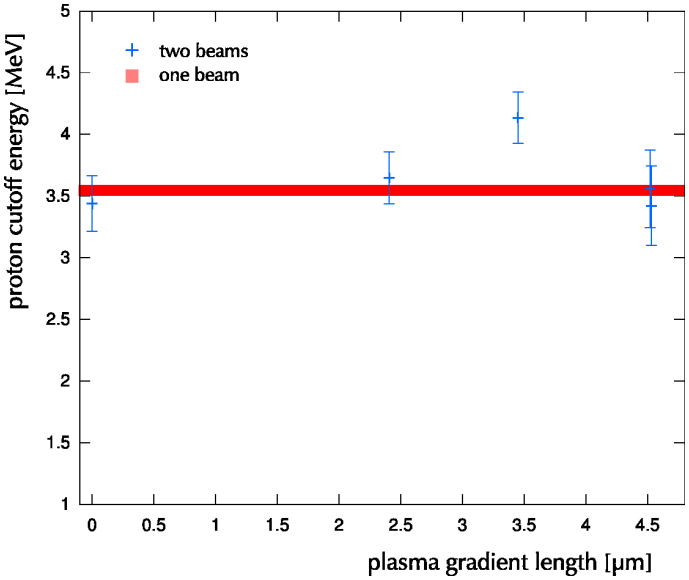


Figure A.4: Two beams proton acceleration: correlation between the proton cutoff energy and the plasma gradient length obtained in the interferometry experiment, Fig.4.16.

realized. Given the size of the required plasma gradient (see Fig.A.4) it is clear that this interaction condition cannot be produced and controlled by the pedestal of a single laser

pulse. Moreover, the required control over the parameters underlines the importance of the technological improvement on the contrast of CPA laser chain.

This preliminary result motivates further studies to completely correlate the condition of the illuminated surface with the proton cutoff energy, and to be able to discriminate among the different interaction phenomena. Forthcoming experiments should include diagnostics to monitor the condition of the rear surface, while the thickness is decreased and the delay between the two pulses is pushed further.

Appendix B

Fundamentals of Plasma Interferometry

This chapter is dedicated to the application of interferometric measurements to the characterization of a plasma. It focuses on the physics concepts and the assumptions that have been made for the plasma interferometry experiment described in chapter Ch.4. In particular the analytical calculation is presented in detail to obtain the dispersion law for a transverse electromagnetic wave in the cold plasma approximation, and how this is used to obtain a full three dimensional density profile out of a single axis tomography measurement of the plasma plume. The numerical approach for image cleaning and analysis of interferometric maps is also presented. This approach proved to be necessary to obtain meaningful experimental data out of measurement with a low signal to noise ratio.

B.1 Fundamentals of plasma interferometry

B.1.1 Maxwell equations

The Maxwell equations for a non-magnetic conductor are[43]:

$$\begin{aligned} &\text{(a)} \quad \underline{\nabla} \cdot \underline{\mathrm{E}} = \frac{\rho}{\varepsilon_0} \qquad \text{(b)} \quad \underline{\nabla} \times \underline{\mathrm{E}} = -\frac{\partial \underline{\mathrm{B}}}{\partial t} \\ &\text{(c)} \quad \underline{\nabla} \cdot \underline{\mathrm{B}} = 0 \qquad \text{(d)} \quad \underline{\nabla} \times \underline{\mathrm{B}} = \mu_0 \underline{\mathrm{J}} + \mu_0 \varepsilon_0 \frac{\partial \underline{\mathrm{E}}}{\partial t} \end{aligned} \tag{B.1}$$

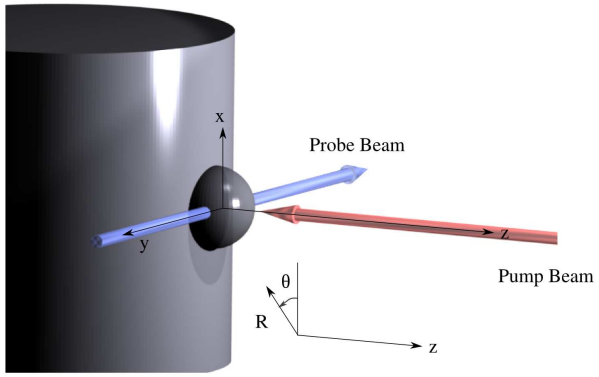


Figure B.1: General scheme of transverse probing (single axis tomography) of a laser created plasma plume.

where the symbols hold their usual meaning[1]. From the substitution of (B.1)d in the curl of (B.1)b, one gets

$$\left(\underline{\nabla}\,\underline{\nabla} - \nabla^2\right)\underline{\mathrm{E}} = -\mu_0 \frac{\partial \underline{\mathrm{J}}}{\partial t} - \mu_0 \varepsilon_0 \frac{\partial^2 \underline{\mathrm{E}}}{\partial t^2}. \tag{B.2}$$

The electric field is decomposed in its frequency components and the equation transformed to its dual in the Fourier space[2]:

$$\begin{aligned} \left(\frac{\underline{\mathrm{k}}\,\underline{\mathrm{k}}}{k^2} - 1\right)\underline{\mathrm{E}} &= \frac{\omega_0}{c^2 k^2}\left[\frac{\mathrm{i}}{\varepsilon_0 \omega_0}\underline{\mathrm{J}} + \underline{\mathrm{E}}\right] \\ &= \frac{\omega_0^2}{c^2 k^2}\left[\frac{\mathrm{i}}{\varepsilon_0 \omega_0}\underline{\underline{\sigma}} + 1\right]\underline{\mathrm{E}}\,. \end{aligned} \tag{B.3}$$

Expressing the current density via the conductivity tensor, $\underline{\mathrm{J}} = \underline{\underline{\sigma}}\,\underline{\mathrm{E}}$, one gets the tensorial equation for the propagation of a whichever, ω-oscillating, *electromagnetic* radiation in a conducting, non-polarized and non-magnetic fluid. For all the cases where the electric field is purely transversal ($\underline{\mathrm{E}} \perp \underline{\mathrm{k}}$) the tensorial term $\underline{\mathrm{kk}}$ voids and the equation is simplified to

$$\frac{\omega_0^2}{c^2 k^2}\left[\frac{\mathrm{i}}{\varepsilon_0 \omega_0}\underline{\underline{\sigma}} + 1 - \frac{c^2 k^2}{\omega_0^2}\right]\underline{\mathrm{E}} = 0. \tag{B.4}$$

[1] MKSA.
[2] $\underline{\nabla} \to \mathrm{i}\underline{\mathrm{k}}$, $\frac{\partial}{\partial t} \to -\mathrm{i}\omega_0$

B.1.2 Electrical permittivity for a cold plasma

The physical properties of the medium are set in (B.4) by the tensor quantity $\underline{\underline{\sigma}}$. This defines the current that is produced in the volume as a consequence to the applied electric field. In a plasma such a reaction can be studied in the fluid approach (see section 3.1). The considered physical conditions (transverse electromagnetic wave of low intensity at $\omega_0 \gg \omega_{pe}$) justify the use of the cold plasma approximation, which neglects the contribution of the kinetic energy of the plasma species during the interaction with fast phenomena. Here are used first order momenta (3.9) for each of the species in the plasma, with $T_\alpha = 0$

$$n_\alpha \frac{\mathrm{D}}{\mathrm{D}t} \underline{\mathrm{u}}_\alpha = \frac{q_\alpha}{m_\alpha} \underline{\mathrm{E}}, \tag{B.5}$$

where q_α is the charge, m_α the mass, $\underline{\mathrm{u}}_\alpha$ the fluid velocity and the operator $\mathrm{D}/\mathrm{D}t$ the convective derivative[3]. From a first order approximation, substituting $n_\alpha = n_{0,\alpha} + n'_\alpha$, $\underline{\mathrm{E}} = \underline{\mathrm{E}}'$ and $\underline{\mathrm{u}}_\alpha = \underline{\mathrm{u}}'_\alpha$ in (B.5) and changing ∂_t in $-\mathrm{i}\omega_0$ one obtains

$$\underline{\mathrm{u}}_\alpha = \frac{\mathrm{i} q_\alpha}{m_\alpha \omega_0} \underline{\mathrm{E}} \tag{B.6}$$

which gives from the definition of $\underline{\mathrm{J}}$ summed over all the species in the plasma

$$\underline{\mathrm{J}} = \sum_\alpha \underline{\mathrm{J}}_\alpha = \sum_\alpha \mathrm{i} \frac{n_\alpha q_\alpha^2}{m_\alpha \omega_0} \underline{\mathrm{E}}\,. \tag{B.7}$$

It is finally defined

$$\underline{\underline{\sigma}} = \sigma \underline{\underline{1}} = \sum_\alpha \mathrm{i} \frac{n_\alpha q_\alpha^2}{m_\alpha \omega_0} \underline{\underline{1}}\,. \tag{B.8}$$

B.1.3 Refraction index for a cold plasma

The $\omega(k)$ relationship is finally calculated by substituting (B.8) in (B.4) and revolving the term in parenthesis. The resulting

$$\frac{c^2 k^2}{\omega^2} = 1 - \sum_\alpha \frac{\omega_{p\alpha}^2}{\omega^2} \tag{B.9}$$

[3] $\mathrm{D}/\mathrm{D}t = \partial/\partial t + \underline{\mathrm{u}} \cdot \underline{\nabla}$

is the searched dispersion relation, where the dependence between the phase velocity ω/k and the plasma parameters is expressed through the plasma α frequency $\omega_{p\alpha}^2 = n_\alpha q_\alpha^2/\varepsilon_0 m_\alpha$. From the definition of the refraction index, it is finally found

$$n = \frac{c}{v_{phase}} = \sqrt{1 - \sum_\alpha \frac{\omega_{p\alpha}^2}{\omega^2}}. \tag{B.10}$$

In equation (B.10) the oscillation of all the species in the plasma is considered. Nevertheless, the contribution of ions can be safely neglected in most cases, as the ion plasma frequency is smaller than the electron one by several orders of magnitude. For example in an Aluminum plasma (Al: $Z = 13$, $A = 27$), the ratio ω_{pi}/ω_{pe} ranges between 10^{-4} and 10^{-5}, depending on the degree of ionization. In forthcoming calculations, the dispersion relation in the electron plasma

$$n\left(\omega_{pe}\right) = \sqrt{1 - \frac{\omega_{pe}^2}{\omega^2}} \tag{B.11}$$

is used instead.

B.1.4 Plasma Interferometry

The relationship (B.11) binds the refraction index to the electron density n_e in the plasma, which opens the possibility of measuring by optical probing the density of an underdense plasma. If a laser probe is let propagate through a region where a plasma exists, its phase plane records the variation of refraction index. Supposing the probe to have travelled a total of Δy at a refraction index of n, the absolute difference in phase is

$$\Delta\varphi = k_0 \left(n - 1\right) \Delta y. \tag{B.12}$$

Considering that, from (B.11), $n(\omega_{pe}) \leq 1$, the resulting variation on the phase is $\Delta\varphi \leq 0$. Inverting the relation (B.12) and using (B.11) one reconstructs the electron density as

$$\left[\frac{1}{k_0}\frac{\Delta\phi}{\Delta y} + 1\right]^2 = 1 - \frac{\omega_{pe}^2}{\omega^2} \longrightarrow n_e = \omega^2 \frac{m_e \varepsilon_0}{e^2} \left\{1 - \left[\frac{1}{k_0}\frac{\Delta\phi}{\Delta y} + 1\right]^2\right\} \tag{B.13}$$

The (B.13) is valid for a constant density medium. Whenever the considered volume contains density gradients, the (B.13) doesn't hold any more and the phase variation has to be integrated along the beam propagation:

$$\Delta\phi = \int \left(\frac{\mathrm{d}\phi}{\mathrm{d}y}\right) \mathrm{d}y = \int k_0 \left[n\left(y\right) - 1\right] \mathrm{d}y. \tag{B.14}$$

The explicit spatial dependence of $n\left(\underline{\mathrm{x}}\right)$ in (B.14) shows that, in general, the probing from a single direction ((B.2)a) does not contain enough information to rebuild the structure.

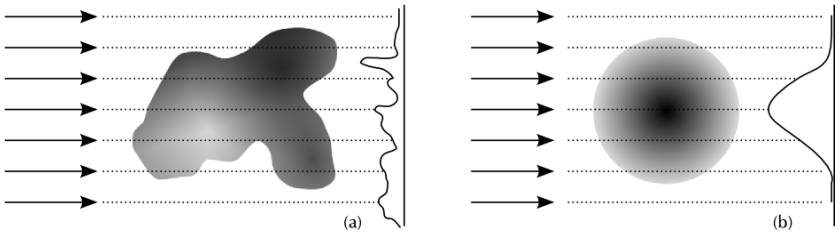


Figure B.2: Probe from single direction; (a) random object, (b) symmetric object

Abel inversion

A particular case (Fig.B.2b) is when the probed object has cylindrical symmetry, so that the integration along every direction gives the same result. In this case, an analytical solution exists (Abel transform, [99]) to reconstruct the entire 2D map from the result of a single direction integration.
This technique can be used every time a scalar quantity on a cylindrical symmetry is integrated on a single direction. In a geometry like the one depicted in Fig.B.1, Fig.B.2b, defined the scalar function $F(x)$, it is possible to calculate the originating distribution via:

$$\epsilon(R) = -\frac{1}{\pi} \int_R^{R_0} \frac{\mathrm{d}F(x)/\mathrm{d}x}{\sqrt{x^2 - R^2}} \mathrm{d}x. \tag{B.15}$$

In the application to the present case the symmetry axis is taken parallel to $\hat{z}$. The inversion calculation is not changed by the presence of the dependence in z, which simply results in the iteration of (B.15) over the symmetry axis; explicitly:

$$\epsilon(R,z) \;=\; -\frac{1}{\pi}\int_{R}^{R_0}\frac{\mathrm{d}F(x,z)/\mathrm{d}x}{\sqrt{x^2-R^2}}\mathrm{d}x \tag{B.16}$$

If $F(x,z)$ is a pure number, for the inverted quantity it holds $[\epsilon(R,z)] \;=\; [length^{-1}]$. Noting that for the local phase distortion is $\Delta\phi = k(n-1)\Delta y$, one can write:

$$n(R,z) \;=\; \frac{1}{k}2\pi\epsilon(R,z)+1 \tag{B.17}$$

which gives the relationship between the Abel-inverted phase-map and the local refraction index. From the cold plasma dispersion relation (B.11) and the refraction index definition, one finally gets

$$n_e(R,z) \;=\; \sqrt{\frac{\omega_{pe}(R,z)^2}{k^2c^2}+1} \;=\; \sqrt{\frac{e^2}{m_e\varepsilon_0k^2c^2}\,n_e(R,z)+1} \tag{B.18}$$

thus

$$n_e(R,z) \;=\; \frac{1}{\eta}\left[\frac{1}{k^2}4\pi^2\left(\epsilon(R,z)+1\right)^2-1\right], \tag{B.19}$$

where all the constant parameters have been shrunk in $\eta = e^2/m_e\varepsilon_0k^2c^2 = 1.45\,10^{-28}$ for $\lambda = 400nm$.

Error on Abel inversion

The radial phase variation is calculated from the experimental value ϕ_{exp} via the relationship

$$\epsilon\,(r) \;=\; \left(\frac{\partial\phi}{\partial r}\,(r,z)\right) \;=\; -\frac{1}{\pi}\int_{r}^{r_0}\frac{\partial\phi/\partial x}{\sqrt{x^2-r^2}}\mathrm{d}x \tag{B.20}$$

which is afterward used in

$$n_e\,(r,z) \;=\; \frac{m_e\varepsilon_0c^2}{e^2}\left[2k_0\left(\frac{\partial\phi}{\partial r}\right)+\left(\frac{\partial\phi}{\partial r}\right)^2\right] \tag{B.21}$$

to obtain the electron density as a function of the radial coordinates. The quantity ϕ_{exp}, as an experimental quantity, will be affected by an error: here I focus on its propagation in the forthcoming calculation, until the 2D density maps. Let $\Delta\phi_e$ and $\Delta\epsilon_r$ be the

absolute error on the reconstructed phase and the resulting error on $\varepsilon(r)$ (as defined in (B.20)) respectively. By definition of absolute error one gets:

$$\Delta\varepsilon_r(r) = \Delta\phi_e \cdot \left(\frac{\mathrm{d}\varepsilon(r)}{\mathrm{d}\phi_e}\right) \tag{B.22}$$

To calculate the derivative is first important to note that not only ϕ_e is a function of (x, z) but also that $\epsilon(r)$ implicitly depends on x; one have so to expand the derivative in

$$\frac{\mathrm{d}}{\mathrm{d}\phi_e} = \frac{\partial x}{\partial \phi_e}\frac{\partial}{\partial x} + \frac{\partial z}{\partial \phi_e}\frac{\partial}{\partial z} \tag{B.23}$$

Substituting (B.23) in (B.22) and applying on (B.20) one gets:

$$\frac{\mathrm{d}}{\mathrm{d}\phi_e}\epsilon(r) = -\frac{1}{\pi}\int_r^{r_0}\left(\frac{\partial x}{\partial \phi_e}\frac{\partial}{\partial x}\right)\frac{\partial\phi_e/\partial x}{\sqrt{x^2-r^2}}\mathrm{d}x \tag{B.24}$$

$$= -\frac{1}{\pi}\int_r^{r_0}\left\{\frac{\left(\partial^2\phi_e/\partial x^2\right)/\left(\partial\phi_e/\partial x\right)}{\left(x^2-r^2\right)^{1/2}} - \frac{x}{\left(x^2-r^2\right)^{3/2}}\right\}\mathrm{d}x \tag{B.25}$$

where the term on $\partial/\partial z$ has been dropped [4]. Substituting the last term

$$\int_r^{r_0}\frac{x}{\left(x^2-r^2\right)^{3/2}}\mathrm{d}x = -\frac{2}{\sqrt{r_0^2-r^2}} \tag{B.26}$$

one obtains the final relationship

$$\Delta\epsilon_r = \Delta\phi_e \cdot \left\{\frac{2}{\pi\sqrt{r_0^2-r^2}} - \frac{1}{\pi}\int_r^{r_0}\frac{\left(\partial^2\phi_e/\partial x^2\right)/\left(\partial\phi_e/\partial x\right)}{\sqrt{x^2-r^2}}\mathrm{d}x\right\} \tag{B.27}$$

$$= \Delta\phi_e \cdot \left\{\frac{2}{\pi\sqrt{r_0^2-r^2}} - \frac{1}{\pi}\int_r^{r_0}\frac{\phi_e^{''}/\phi_e^{'}}{\sqrt{x^2-r^2}}\mathrm{d}x\right\} \tag{B.28}$$

Final substitution in (B.21) gives

$$\Delta n_e(r) = \frac{m_e\varepsilon_0 c^2}{e^2}\left[2k_0\,\Delta\epsilon(r) + 2\Delta\epsilon(r)^2\epsilon(r)\right] \tag{B.29}$$

[4] The inversion procedure is applied independently on "slices" parallel to x-axis, therefore no z-error propagates through the integration process. Errors on z-axis will be taken in account as a distance uncertainty from the target surface.

which will be used for error estimation in interferogram analysis.

B.2 Numerical Analysis of Interferograms

As shown by the calculation method in [62] the phase retrieval process is more easily accomplished if a heterodyne frequency is introduced in interferometry figure. In this way the phase perturbation information is contained in a deformation of the carrier spectrogram.

Retrieval of the phase information

The intensity pattern in the interferogram is represented on the $\underline{x} = (x, z)$ plane by:

$$\begin{aligned} i(\underline{x}) &= m(\underline{x}) \sin[\underline{k}_h \cdot \underline{x} + \phi(\underline{x})] + b(\underline{x}) + n(\underline{x}) \\ &= m(\underline{x}) \frac{1}{2i} \left[\xi(\underline{x}) \, e^{i2\pi \underline{\nu}_{h0} \cdot \underline{x}} - c.c. \right] + b(\underline{x}) + n(\underline{x}) \end{aligned} \tag{B.30}$$

where $m(\underline{x})$ is the low-frequency amplitude envelope, $b(\underline{x})$ the low-frequency background fluctuations and $n(\underline{x})$ the random noise; $\xi(\underline{x}) = \exp(i\varphi(\underline{x}))$. The vectors $\underline{k}_h = (k_{h,x}, k_{h,z})$ and $\underline{\nu}_{h0} = (\nu_{h0,x}, \nu_{h0,z})$ represent respectively the heterodyne wave number and the carrier spatial frequency on the interferogram. A term for the non-linear response of the recording medium, normally found in other procedures (es. [8][5]), is here neglected.
By direct transform one obtains:

$$I(\underline{\nu}_h) = M(\underline{\nu}_h) * \Xi(\underline{\nu}_h) * \delta(-\underline{\nu}_h - \underline{\nu}_{h0}) + M(\underline{\nu}_h) * \Xi^*(\underline{\nu}_h) * \delta(\underline{\nu}_h - \underline{\nu}_{h0}) + B(\underline{\nu}_h) + N(\underline{\nu}_h). \tag{B.31}$$

The first two terms clearly represent the direct transform of the sought experimental information[6], translated by positive and negative heterodyne frequency; the two last terms are the F-transforms of the corresponding terms in (B.31).
The experimental information has been moved, by the heterodyne frequency, between the area surrounding the zero order, where the low frequency noise and intensity fluc-

[5] This would be necessary when using non-linear recording media, like standard CCD cameras or photographic films; good quality scientific cameras show, nowadays, a good linearized response.
[6] $\xi \rightarrow \Xi$

tuations are, and the high frequency peripheral zone[7]. The $\varphi(r)$ term can be isolated through

$$\xi(\underline{x}) = \mathfrak{F}^{-1}\left\{\chi_{[-a,a]} \cdot [I(\underline{\nu}_h) * \delta(\underline{\nu}_h \pm \underline{\nu}_{h0})]\right\} \tag{B.32}$$

$$\varphi(\underline{x}) = \tan^{-1}\frac{\mathrm{Im}[\xi(\underline{x})]}{\mathrm{Re}[\xi(\underline{x})]}. \tag{B.33}$$

Here the convolution with $\delta()$ is used to translate back to the origin one of the heterodyne peaks and the χ term represents the filter which eliminates any other component.

Direct subtraction of the heterodyne component

The procedure here presented is followed almost exactly in the numerical case. Some authors suggest [62] to avoid the $\delta()$ convolution or a direct translation/rotation of the 2D Fourier plane as a way to eliminate the heterodyne component.
In fact the $\underline{\nu}_{h0} \cdot \underline{x}$ term in (B.31) introduces nothing else than a two-dimensional plane in the space (x, z, ϕ). A direct subtraction of the heterodyne plane in the phase space provides a cleaner way of isolating the experimental information.
It is then calculated

$$\xi(\underline{x}) = \mathfrak{F}^{-1}\left\{\chi_{[a_1,a_2]} \cdot I(\underline{\nu}_h)\right\} \tag{B.34}$$

$$\varphi(\underline{x}) = \tan^{-1}\frac{\mathrm{Im}[\xi(\underline{x})]}{\mathrm{Re}[\xi(\underline{x})]} - \phi_{het}(\underline{x}). \tag{B.35}$$

The $\phi_{het}(\underline{x})$ term in (B.35) is easily calculated by performing a numerical fit on the retrieved phase plane ($\tan^{-1}(\cdots)$).

B.2.1 Application to the experimental case

The interferograms presented in Ch.4 are treated numerically and analysed in their 2D Fourier plane. From the point of view of the physical content of the experiment, the choice of the term $\chi(\underline{x})_{[a_1,a_2]}$ in (B.35) is the most critical. From the analytical point of view, the χ function has a supergaussian envelope of the 10^{th} order. The parameters of the filtering term are chosen from physical considerations. The boundaries that are

[7] Qualitatively, the heterodyne frequency should have the smallest possible wavelength but having a sufficiently high number of pixels per period.

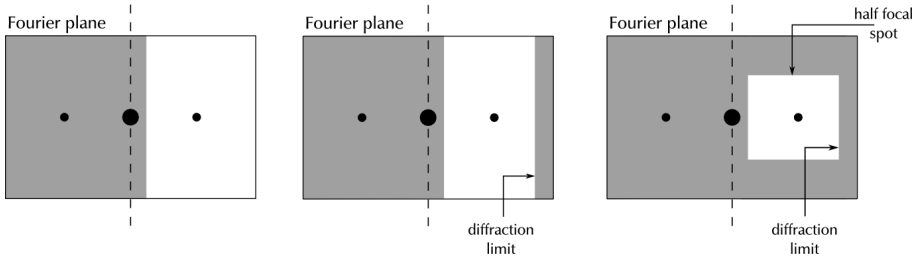


Figure B.3: Filtering of the experimental images in the Fourier plane. The big spot in the center represents the zero frequency component, while the two smaller spots are the heterodyne frequency peak.

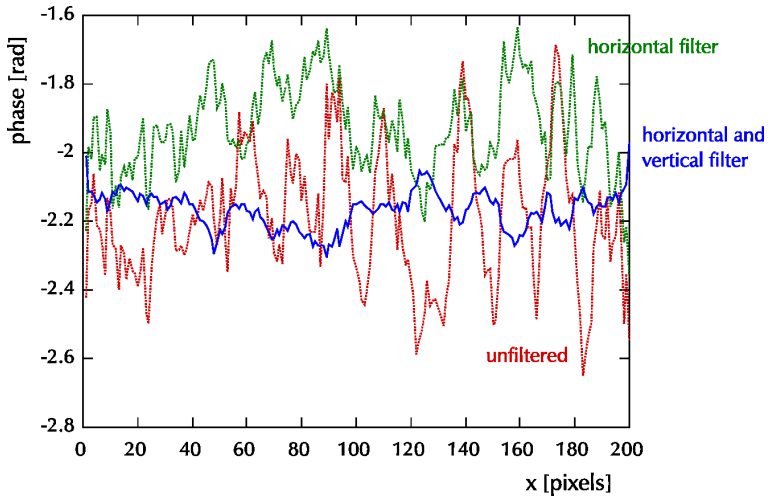


Figure B.4: Comparison between the retrieved phase profile with the three filtering techniques (Fig.B.3)

needed to isolate the components around the heterodyne peak and to build the phase plane (Fig.B.3-I) impose to eliminate the zero order and to keep one of the two half-planes in the Fourier domain (Fig.B.3-I). A stricter condition on the horizontal direction consists in setting a higher threshold on spacial frequencies that hold detail with a size lower than the diffraction limit of the imaging system (Fig.B.3-II). This limit comes from the assumption that any meaningful physical detail on the image should not be smaller than the limits of the optical system. On the vertical direction (Fig.B.3-III) the limit is set on half of the size of the laser focal spot. This choice comes from the consideration that the imaged plasma hardly has spatial features smaller than the transverse profile

of the laser used for creating it. This limits are calculated considering that, set D_ν the resolution in the frequency domain and D_x the spatial resolution of the acquired image, it holds

$$D_x = \frac{1}{N\, D_\nu}, \tag{B.36}$$

where N is the number of points on the image in the considered axis.
In Fig.B.4 it is shown the comparison between the same horizontal cut in the retrieved phase plane, calculated with the three different filters that are proposed in Fig.B.3.

Bibliography

Bibliography

[1] P. Agostini and al. Multiphoton ionization of hydrogen and rare gases. *IEEE J. Quant. Elec.*, QE-4:667, 1968.

[2] P. Agostini and al. Free transitions following 6-photon ionization of xenon atoms. *Phys. Rev. Lett.*, 42:1127, 1979.

[3] Albritton and al. Cold plasma wavebreaking: Production of energetic electrons. *Phys. Fluids*, 9:1136, 1975.

[4] A. Andreev and al. Effect of a laser prepulse on fast ion generation in the interaction of ultra-short intense laser pulses with a limited mass foil target. *Plasma Phys. and Contr. Fus.*, 48:1605, 2006.

[5] L. Antonucci and al. Sub-15 fs, high temporal contrast front-end for pw class laser system. 2006.

[6] D. T. Attwood. Interferometric confirmation of radiation-pressure effects in laser-plasma interactions. *Phys. Rev. Lett.*, 40(3):184, 1978.

[7] S. Backus. Prepulse suppression for high energy ultrashort pulsesusing self-induced plasma shuttering from a fluid target. *Opt. Lett.*, 18:134, 1993.

[8] Bone and al. Fringe pattern analysis using a 2-d fourier transform. *Appl.Opt.*, 10:1653, 1986.

[9] L. Bonnet, A. Decoster, and S. Jacquemot. Electromagnetic solver for short-pulse laser-matter interaction. *Laser Interaction with matter institute of physics conference series*, 140:193–196, 1995.

[10] R. W. Boyd. *Nonlinear Optics.* Academic Press, 1992.

[11] F. Brunel. Not-so-resonant, resonant absorption. *Phys. Rev. Lett.*, 59:52, 1987.

[12] T. Ceccotti and al. Proton acceleration with high-intensity ultrahigh-contrast laser pulses. *Phys. Rev. Lett.*, 99:185002, 2007.

[13] F. F. Chen. *Plasma Physics and Controlled Fusion*. Plenum Press, 1984.

[14] R. Cohen, L. Spitzer, and P. M. Routly. The electrical conductivity of a ionized gas. *Phys.Rev.*, 80:230, 1950.

[15] T. E. e. a. Cowan. Ultra-low emittance, multi-mev proton beam from a laser virtual cathode plasma accelerator. *Phys. Rev. Lett.*, 92:204801, 2004.

[16] J. Crow. *J. Plasma Physics*, 14:65, 1975.

[17] G. Doumy and al. Complete characterization of a plasma mirror for the production of high-contrast ultraintense laser pulses. *Phys. Rev. E*, 69(2):026402, 2004.

[18] W. Ehler and al. Origin of energetic ions from laser-produced plasmas. *J. Appl. Phys.*, 44:4229, 1973.

[19] W. Ehler and al. Effect of target purity on laser produced plasma expansion. *J. Phys. D*, 13:29, 1980.

[20] J. K. Eidmann, T. Meyer-ter Vehn, T. Schlegel, and S. Huller. Hydrodynamic simulation of subpicosecond laser interaction with solid-density matter. *Phys. Rev. E*, 62:1202, 2000.

[21] A. Einstein. Zur quantentheorie der strahlung. *Physikalische Zeitschrift*, 18:121, 1917.

[22] R. Fabbro. *Etude de l'influence de la longeur d'onde laser sur les processus de conduction termique et d'ablation dans les plasmas créés par laser*. PhD thesis, Univ. Paris VI, 2000.

[23] J. Faure, Y. Glinec, A. Pukhov, S. Kiselev, S. Gordienko, E. Lefebvre, J. P. Rousseau, F. Burgy, and V. Malka. A laser-plasma accelerator producing monoenergetic electron beams. *Nature*, 431:541–544, sep 2004.

[24] J. Faure, C. Rechatin, A. Norlin, A. Lifschitz, Y. Glinec, and V. Malka. Controlled injection and acceleration of electrons in plasma wakefields by colliding laser pulses. *Nature*, 444:737–739, 2006.

[25] R. Fedosejevs. Self-steepening of the density profile of a co2-laser-produced plasma. *Phys. Rev. Lett.*, 39(15):932, 1977.

[26] E. Fourkal and al. Coulomb explosion effect and the maximum energy of protons accelerated by high power lasers. *Phys. Rev. E*, 71:036412, 2005.

[27] Freidberg and al. Resonant absorption of laser light by plasma targets. *Phys. Rev. Lett.*, 13:795, 1972.

[28] S. Friztler and al. Ion heating and thermonuclear neutron production fromhigh intensity subpicosecond laser pulses interacting withunderdense plasmas. *Phys. Rev. Lett.*, 89:165004, 2002.

[29] J. Fuchs and al. Comparison of laser ion acceleration from the front and rear surfaces of thin foils. *Phys.Rev.Lett*, 94:45004, 2005.

[30] Gamaly and al. Ablation of solids by femtosecond lasers: ablation mechanism and ablation threshols for metal and dielectrics. *Phys. Plasmas*, 9:949, 2002.

[31] Geant4 collaboration. Geant4 - a simulation toolkit. *Nucl. Instr. and Meth. Phys. Res. A*, 506:250, 2003.

[32] Geant4 collaboration. Geant4 developements and applications. *IEEE Trans. on Nucl. Sci.*, 53:270, 2006.

[33] C. G. R. Geddes, C. Toth, J. van Tilborg, E. Esarey, C. B. Schroeder, D. Bruhwiler, C. Nieter, J. Cary, and W. P. Leemans. High-quality electron beams from a laser wakefield accelerator using plasma-channel guiding. *Nature*, 431:538–541, sep 2004.

[34] P. Gibbon. *Short Pulse Laser Interactions with Matter*. Imperial College Press, 2005.

[35] Ginsburg and al. *Propagation of electromagnetic waves in plasmas*. Gordon and Breach, New York, 1960.

[36] S. J. Gitomer. Fast ions and hot electrons in the laser-plasma interaction. *Phys. Fluids*, 29:2679, 1986.

[37] D. Gold. Prepulse suppression using a self-induced ultra-shortpulse plasma mirror. *SPIE Proc.*, 1413:41, 1991.

[38] A. Gurevich and al. Ion acceleration in an expanding rarefied plasma with non-maxwellian electrons. *Phys. Rev. Lett.*, 42:769, 1979.

[39] H. Habara. Momentum distribution of accelerated ions in ultra-intense laser-plasma interactions via neutron spectroscopy. *Phys. Plasma*, page 3712.

[40] H. Habara. Fast ion acceleration in ultraintense laser interaction with an overdense plasma. *Phys. Rev. E*, 69:36407, 2004.

[41] S. P. Hatchett. Electron, photon, and ion beams from the relativistic interaction of petawatt laser pulses with solid targets. *Physics of Plasmas*, 7(5):2076, 2000.

[42] M. Hegelich and al. Mev ion jets from short-pulse-laser interaction with thin foils. *Phys. Rev. Lett.*, 89:085002, 2002.

[43] J. D. Jackson. *Classical Electrodynamics*. Wiley, 1975.

[44] S. Jacquemot. *SPIE Proceedings*, 2012:180, 2003.

[45] A. Jullien and al. 10-10 temporal contrast for femtosecond ultraintense lasers by cross-polarized wave generation. *Opt. Lett.*, 30:920, 2004.

[46] A. Jullien and al. Nonlinear polarization rotation of elliptical light in cubic crystals, with application to cross-polarized wave generation. *J. Opt. Soc. Am. B*, 22:2635, 2005.

[47] A. Jullien and al. Two crystal arrangement to fight efficiency saturation in cross-polarized wave generation. *Opt. Expr.*, 14:2760, 2006.

[48] A. Jullien and al. Spectral broadening and pulse duration reduction during cross-polarized wave generation: influence of the quadratic spectral phase. *Appl. Phys. B*, 87:595, 2007.

[49] M. Kaluza and al. Influence of the laser prepulse on proton acceleration in thin foil experiments. *Phys. Rev. Lett.*, 93:45003, 2004.

[50] H. C. Kapteyn. Prepulse energy suppression for high energyultrashort pulses using self-induced plasma shuttering. *Opt. Lett.*, 16:490, 1991.

[51] Keldysh and al. Ionization in the field of a strong electromagnetic wave. *Sov. J. Exp. Theor. Phys.*, 20:1307, 1965.

[52] M. V. Klein and T. E. Furtak. *Optics*. Wiley, 1986.

[53] F. Kruer and J. Estabrook. Jxb heating by very intense laser light. *Phys. Fluids*, 28:430, 1985.

[54] W. L. Kruer. Ponderomotive and thermal filamentation of laser light. *Comm. Plasma Phys. and Contr. Fusion*, 9:63, 1985.

[55] A. Levy and al. Double plasma mirror for ultrahigh temporal contrast ultraintense laser pulses. *Opt. Lett.*, 32:310, 2007.

[56] Y. T. Li and al. High-energy electrons produced in subpicosecond laser-plasma interactions from subrelativistic laser intensities to relativistic intensities. *Phys. Rev. E*, 69(3):036405, 2004.

[57] F. Lindau and al. Laser-accelerated protons with energy-dependent beam direction. *Phys. Rev. Lett.*, 95:175002, 2005.

[58] T. V. Liseikina and al. Features of ion acceleration by circularly polarized laser pulses. *Appl. Phys. Lett.*, 91:171502, 2007.

[59] A. Macchi and al. Laser acceleration of ion bunches at the front surface of overdense plasmas. *Phys. Rev. Lett.*, 94:165003, 2005.

[60] A. J. Mackinnon and al. Effect of plasma scale length on multi-mev proton production by intense laser pulses. *Phys. Rev. Lett.*, 86:1769, 2001.

[61] A. J. MacKinnon and al. Enhancement of proton acceleration by hot electron-recirculation in thin foils irradiated by ultraintense laserpulses. *Phys. Rev. Lett.*, 88:215006, 2002.

[62] W. W. Macy. Two dimensional fringe-pattern analysis. *Appl. Opt.*, 22:3898, 1983.

[63] T. H. Maiman. Stimulated optical radiation in ruby. *Nature*, 183:493, 1960.

[64] Mainfray and al. Multiphoton ionization of atoms. *Rep. Prog. Phys.*, 54:1333, 1991.

[65] S. P. D. Mangles, C. D. Murphy, Z. Najmudin, A. G. R. Thomas, J. L. Collier, A. E. Dangor, E. J. Divall, P. S. Foster, J. G. Gallacher, C. J. Hooker, D. A. Jaroszynski, A. J. Langley, W. B. Mori, P. A. Norreys, F. S. Tsung, R. Viskup,

B. R. Walton, and K. Krushelnick. Monoenergetic beams of relativistic electrons from intense laser-plasma interactions. *Nature*, 431:535–538, sep 2004.

[66] P. McKenna and al. Effect of target heating on ion induced reactions in high intensity laser-plasma interactions. *Appl.Phys.Lett.*, 83:2763, 2003.

[67] P. McKenna and al. Characterization of proton and heavier ion acceleration in ultrahigh intensity laser interaction with heated target foils. *Phys. Rev. E*, 70:36405, 2004.

[68] P. McKenna and al. High intensity laser-driven proton acceleration:influence of the pulse contrast. *Philos. Trans. A*, 15:364, 2006.

[69] N. Minkovski and al. Polarization rotation induced by cascaded third-order processes. *Opt. Lett.*, 27:2025, 2002.

[70] N. Minkovski and al. Nonlinear polarization rotation and orthogonal polarization generation experienced in a single-beam configuration. *J. Opt. Soc. Am. B*, 21:1659, 2004.

[71] P. Mora. Plasma expansion into a vacuum. *Phys. Rev. Lett.*, 90:185002, 2003.

[72] P. Mora. Thin-foil expansion into a vacuum. *Phys. Rev. E*, 72:56401, 2005.

[73] P. Mora and T. Grismayer. Influence of a finite initial ion intensity gradient on plasma expansion into a vacuum. *Phys. Plasmas*, 13:32103, 2006.

[74] P. Mora and R. Pellat. Self-similar expansion of a plasma into a vacuum. *Phys. Fluids*, 22:2300, 1979.

[75] P. Mulser. Basic laser-plasma interaction and essential relativity, 2006. Lectures.

[76] P. Mulser and D. Bauer. *High Power Laser Matter Interaction*. Springer, 2004.

[77] Y. Murakami. Observation of proton rear emission and possible gigagauss scale magnetic field from ultra-intense laser-illuminated plasma target. *Phys. Plasma*, 8:4138, 2001.

[78] D. Neely and al. Enhanced proton beams from ultrathin targets driven byhigh contrast laser pulses. *Appl. Phys. Lett.*, 89:1502, 2006.

[79] K. Nemoto. Laser-triggered ion acceleration and table top isotope production. *Applied Physics Letters*, 78(5):595, 2001.

[80] R. Nuter and al. Influence of a preplasma on electron heating and proton acceleration in ultraintense laser-foil interaction. *J. Appl. Phys*, 104(10):103307, 2008.

[81] Popov. Tunnel and multiphoton ionization of atoms and ions in a strong laser field (keldysh theory). *Physics Uspekhi*, 47:855, 2004.

[82] Popov and al. On the relativistic generalization of keldysh ionization theory. *Phys. Lett. A*, 358:21, 2006.

[83] A. Pukhov. Three-dimensional simulations of ion acceleration from a foil irradiated by a short-pulse laser. *Physical Review Letters*, 86(16):3562, 2001.

[84] A. Pukhov and al. Laser hole boring into overdense plasma and relativistic electron currentsfor fast ignition. *Phys. Rev. Lett.*, 79:2686, 1997.

[85] M. Rana. Studies of cr-39 etch rates. *Nuclear Instruments and Methods in Physics Research Section B Beam Interactions with Materials and Atoms*, 198(3-4):129, 2002.

[86] Rozmus and al. A model for ultrashort laser pulse absorption in solid targets. *Phys. Plasma*, 3:360, 1996.

[87] M. I. K. Santala. Effect of the plasma density scale length on the direction of fast electrons in relativistic laser-solid interactions. *Phys. Rev. Lett.*, 84:1459, 2000.

[88] M. I. K. Santala. Effect of the plasma density scale length on the direction of fast electrons in relativistic laser-solid interactions. *Phys. Rev. Lett.*, 84(7):1459, 2000.

[89] J. J. Santos. Fast electron transport in ultraintense laser pulse interaction with solid targets by rear-side self-radiation diagnostics. *Phys. Rev. Lett.*, 89:025001, 2002.

[90] J. J. Santos. Fast-electron transport and induced heating in aluminum foils. *submitted to PoP*, 2007.

[91] Y. Sentoku and al. High proton acceleration in interaction of short laser pulse with dense plasma target. *Phys. Plasmas*, 10:2009, 2003.

[92] J. T. Seo. Effects of underdense preplasma on the energetic proton generation inultraintense short laser pulse interaction with an overdense plasma slab. *J. Phys. Soc. of Japan*, 11:114501, 2007.

[93] R. A. Snavely. Intense high-energy proton beams from petawatt-laser irradiation of solids. *Phys. Rev. Lett.*, 85(14):2945, 2000.

[94] L. Spitzer and R. Harm. Transport phenomena in a completely ionized gas. *Phys.Rev*, 89:977, 1953.

[95] D. Strickland and G. Mourou. Compression of amplified chirped optical pulses. *Opt. Commun.*, 56:219, 1985.

[96] A. Tafo. *Faisceaux de protons générés par l'interaction d'un laser ultra-court avec une cible solide*. PhD thesis, École Polytechnique, 2007.

[97] T. Tajima and J. M. Dawson. Laser electron accelerator. *Phys. Rev. Lett*, 43:267, 1979.

[98] M. A. True. Fast ion production by suprathermal electrons in laser fusion plasmas. *Phys. Fluids*, 24:1885, 1981.

[99] (various). Abel inversion of emission and backlighting images. *University of Rochester, LLE Review*, page 66, 1996.

[100] G. S. Voronov and N. B. Delone. Ionization of xenon atom by electric field of ruby laser emission. *Sov. Phys. JETP Lett.*, 1:66, 1965.

[101] S. C. Wilks and al. Absorption of ultrashort, ultra-intense laser light by solids and overdense plasmas. *IEEE J. Quantum El.*, 33:1954, 1997.

[102] S. C. Wilks and al. Energetic proton generation in ultra intense laser solid interactions. *Phys. Plasmas*, 8:542, 2001.

[103] M. Zepf and al. Proton acceleration from high intensity laser interactions with thin foil targets. *Phys. Rev. Lett.*, 90:064801, 2003.